Section of Hydraulic Engineering

THE USE OF PILE GROYNES

TO REDUCE SEDIMENT EXCHANGE

BETWEEN RIVER AND HARBOUR

MSc Thesis
REPORT

Jessica Tamara Castillo Rodríguez
Juny 2008

UNIVERSIDAD POLITECNICA DE VALENCIA

TU Delft
Technische Universiteit Delft

Delft University of Technology
Faculty of Civil Engineering and Geosciences
Hydraulic Engineering Section

THE USE OF PILE GROYNES TO REDUCE SEDIMENT EXCHANGE BETWEEN RIVER AND HARBOUR

MSc Thesis

Jessica Tamara Castillo Rodríguez
1381857
J.T.CastilloRodríguez@student.tudelft.nl

Juny 2008

Thesis committee:
Prof. dr. ir H.J. de Vriend
Section of River Engineering

Dr. ir. W.S.J. Uijttewaal
Section of Environmental and Fluid Mechanics

Dr. ir. B.C. van Prooijen
Section of Hydraulic Engineering

Ir. H. Havinga
Section of River Engineering

UNIVERSIDAD POLITECNICA DE VALENCIA

TU Delft
Technische Universiteit Delft

SUMMARY

"The use of pile groynes to reduce sediment exchange between river and harbour"

Introduction

To reduce siltation in harbours located in rivers or waterways in order to decrease the high costs of dredging and maintenance of its basins, a need of searching measures to decrease the sediment exchange between river and harbour arises.

Research

One of the measures to reduce the sediment exchange is the use of pile groynes structures located in the river stream, upstream the entrance of the harbour basin.

Due to the blocking of the groynes, the velocities of the river will increase. Because of this, the navigability along the river stream can be altered.

The objective of this research is to determine the effect of the groyne at the interface harbour-river and the mixing layer which develops along the entrance.

Experiments

To analyze the effect of the groyne on the mixing layer dynamics, a schematized physical model of a harbour basin was built in a laboratory flume.

Different configurations of the pile groyne were performed to devise the effect of different geometries of the groyne.

In order to relate the exchange process to velocity distributions, Particle Tracking Velocimetry measurements were performed to obtain the velocity field at the water surface.

The analysis of data was approached on the exchange which takes place via the mixing layer and the primary gyre, that are formed at the river-harbour interface and the harbour basin, respectively.

On the basis of the experimental results can be concluded that the best configurations to reduce the entrainment of water and the velocity gradient along the entrance are the groynes located close to the upstream corner and with spacing between piles lower than its width.

Numerical modelling

Several configurations of the groyne were simulated using state of the art of a 2D numerical model, FinLab, in order to perform a comparison between experiments and simulations, providing an indication as to what extent the exchange processes are properly incorporated into this model.

A good estimation can be obtained for the case without groyne in relation with the basic structures and turbulence properties of the mixing layer at the interface river-harbour. However, it was not possible to simulate the effect of the groyne by increasing the roughness coefficient at the groyne location.

For this reason, some recommendations for further studies about that topic are given.

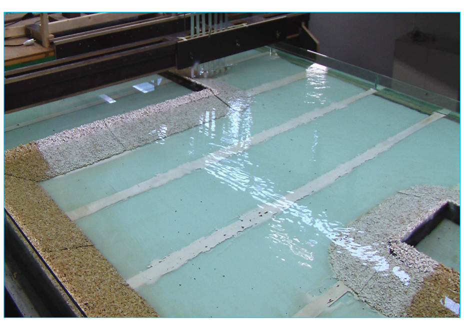

Scale physical model.

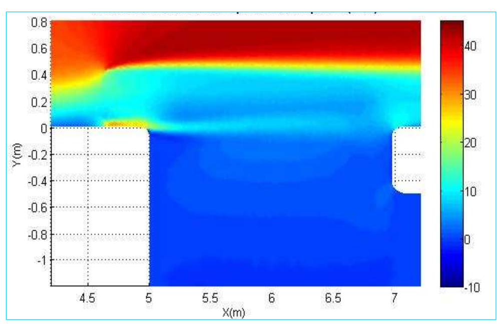

Numerical results.

PREFACE.

The thesis on hand was written during an exchange programme of ten months between Delft University of Technology, The Netherlands, and Universidad Politécnica de Valencia, Spain.

In this Master Thesis an experimental study on the effect of pile groyne structures on sediment exchange has been described. The work has been carried out at the Fluid Mechanics Laboratory at the Faculty of Civil Engineering, Delft University of Technology.

The Thesis is supported by the Rijkswaterstaat and based on a WINN project (Water Innovation Programme).

I would like to thank the members of the graduation committee for their comments and suggestions. The work has been supervised by Prof. dr. ir. H.J. de Vriend, dr. ir. W.S.J. Uijttewaal, dr. ir. B.C. van Prooijen and ir. H. Havinga.

For their daily support, I would like to express my gratitude to Wim Uijttewaal for his continual help and advice with the experimental model and the data analysis, and Bram van Prooijen for giving frequent assistance with the numerical model *FinLab*. Prof. dr. ir. H. de Vriend and ir. H. Havinga are gratefully acknowledged for their comments on my project.

I would like to thank the members of the laboratory of Fluid Mechanics and, specially, the students Victor Roels and Thomas Snoel for their help during the experiments.

Moreover, I wish to thank Prof. dr. ir. Juan F. Fernández Bono, for being my supervisor in Valencia, not only during the practise period last summer, but during this year as well.

Finally, special thanks to my family and friends, for their understanding and endless support during this year abroad and during the last six years.

Jessica T. Castillo Rodríguez

Delft,
Juny 2008

ABSTRACT.

To reduce siltation in harbours located in rivers or waterways in order to decrease the high costs of dredging and maintenance of its basins, a need of searching measures to decrease the sediment exchange between river and harbour arises.

One of the measures to reduce the sediment exchange is the use of pile groynes structures located in the river stream, upstream the entrance of the harbour basin.

Due to the blocking of the groynes, the velocities of the river will increase. Because of this, the navigability along the river stream can be altered.

The objective of this research is to determine the effect of the groyne at the interface harbour-river and the mixing layer which develops along the entrance.

To analyze the effect of the groyne on the mixing layer dynamics, a schematized physical model of a harbour basin was built in a laboratory flume.

Different configurations of the pile groyne were performed to devise the effect of different geometries of the groyne.

In order to relate the exchange process to velocity distributions, Particle Tracking Velocimetry measurements were performed to obtain the velocity field at the water surface.

The analysis of data was approached on the exchange which takes place via the mixing layer and the primary gyre, that are formed at the river-harbour interface and the harbour basin, respectively.

On the basis of the experimental results can be concluded that the best configurations to reduce the entrainment of water and the velocity gradient along the entrance are the groynes located close to the upstream corner and with spacing between piles lower than its width.

Several configurations of the groyne were simulated using state of the art of a 2D numerical model, FinLab, in order to perform a comparison between experiments and simulations, providing an indication as to what extent the exchange processes are properly incorporated into this model.

A good estimation can be obtained for the case without groyne in relation with the basic structures and turbulence properties of the mixing layer at the interface river-harbour. However, it was not possible to simulate the effect of the groyne by increasing the roughness coefficient at the groyne location.

For this reason, some recommendations for further studies are given in this thesis.

INDEX OF CONTENTS.

LIST OF FIGURES.

LIST OF TABLES.

LIST OF SYMBOLS.

Greek

α Angle of the harbour entrance with respect the x direction.
Entrainment coefficient.
δ Mixing layer width.
ε Dissipation.
λ Relative velocity difference between river-water and harbour-water.
Γ Eddy diffusivity.
γ Normalized parameter.
μ Dynamic viscosity.
μ_t Dynamic turbulent viscosity.
υ Kinematic viscosity.
ν_t Kinematic turbulent viscosity.
σ_t Turbulent Schmidt number.
ρ Density of water.

Latin

$\hat{a}$ Tide amplitude.
A Harbour entrance area.
B Width of the harbour entrance
$c_{\varepsilon 1}$, $c_{\varepsilon 2}$ Constants in modelled ε equation.
c_μ Constant in turbulence model.
c_a Ambient suspended sediment concentration.
c_f Bed friction coefficient.
c_h Suspended sediment concentration.
D Water depth.
f_e Exchange coefficient / Entrainment factor.
h Water depth.
k Von Karman constant. /Turbulent kinetic energy.
L Length of the harbour basin.
M_i 1D equation of motion.
p Basin trapping efficiency.
Q Exchange flow rate.
Q_{in} Inflow rate through harbour entrance.
Q_{out} Outflow rate through harbour entrance.
Q_e Exchange flow from horizontal entrainment.
Q_t Tidal filling exchange flow rate.
S Surface area of harbour basin.
T Tidal period.
T_h Horizontal residence time.
u Velocity component in streamwise direction.
u_c Critical velocity for sedimentation.
u_r River flow velocity.
u_h Average harbour basin velocity.
u'_i Fluctuating velocity in x_i direction.

$\bar{u}_i$	Mean velocity in x_i direction.
v	Velocity component in transverse direction.
U,V	Depth-averaged streamwise and transverse velocity
V	Harbour basin volume.
w	Velocity component in vertical direction.
W_s	Sediment settling velocity.
x	Longitudinal coordinate.
y	Transverse coordinate.
y_c	Transverse position of the centre of the mixing layer.
z	Vertical coordinate.

Symbols

´	Deviation of the mean value.

Subscripts

c	Mixing layer centre.
r	River.
h	Harbour basin.
i,j	Indices.
in	Inflow rate.
out	Outflow rate.
std	Standard Deviation.

Notation

1D	One Dimensional.
2D	Two Dimensional.
3D	Three Dimensional.
ADV	Acoustic Doppler Velocimeter.
CDW	Current Deflecting Wall.
EMS	Electromagnetic Sensor.
FEM	Finite Elements Method.
KSM	Methods to keep the sediment moving.
KSN	Methods to keep sediment navigable.
KSO	Methods to keep sediment out.
MHS	Minimizing Harbour Siltation.
PTV	Particle Tracking Velocimetry.
SWE	Shallow Water Equations.

CHAPTER 1.

INTRODUCTION.

1.1. General.

Siltation of harbour basins is one of the most serious problems in commercial and recreational harbours. High rates of siltation may bring high costs of maintenance dredging to sustain the accessibility of the harbour. In most cases, it is required to remove the sediment regularly. This task is not only high-priced; sediment can be contaminated making it more difficult to find disposal areas.

Many millions of cubic metres of mud are dredged annually from harbour approaches, fairways and basins in order to safeguard navigation.

Due to high dredging costs and environmental concerns, there are compelling reasons to seek to reduce dredging volumes by minimising harbour siltation.

Therefore, a need exists of methods by which the sediment transport into harbours can be reduced. Different methods have been carried out during the last decades, but nowadays there are new and promising methods for reducing harbour siltation.

This thesis project lays emphasis on the use of pile groyne structures that modify the flow pattern at harbour entrances to minimize the sediment flux to the harbour area.

1.1.1. Dredging costs and other problems.

Dredging volumes at many harbours from all over the world are expected to increase due to continued economic growth and the increase in vessel draught.

Apart from dredging for shipping, which is the main reason for dredging, this procedure is expected to be increasingly pressed by public interests, such as environmental protection, water supply, drainage and flood defence.

As a consequence, authorities pay a large part of dredging costs, in combination with port authorities. Total cost is composed of cost for dredging activities, for transport and, depending on the quality and quantity of sediments, for treatment and disposal.

Generally, a large part of the dredged material can be relocated within the system in suitable locations. For larger waters, relocation in water is often possible and for smaller waters, placement can occur on floodplain soils nearby. However, if relocation is unfavourable or impossible due to environmental or spatial reasons, alternative options have to be employed such as beneficial use, treatment and confined disposal.

Although only a relatively small part of the dredged sediments is contaminated, special provisions have to be prepared for this material and they are only a temporal solution for the problem. Occasionally, the amount of contaminated sediments can become significant.

In addition, the presence of pollutants in the harbour water contributes to the deterioration of the water quality in the harbour. Some recreational marinas have had to close down permanently as a result.

For this reason, dredging is necessary at both large commercial and small craft harbours and its cost can threaten the financial viability of both.

Four obvious themes are presented *(PIANC, 2007)* which lead to the need for a development of different measures to reduce the sediment exchange to achieve a solution to the problem.

- Firstly, industry is experiencing continued growth in vessel size, first tankers, bulk carries and container ships. As a consequence, deeper basin depths are required.
- Secondly, the consequences of gross over-deepening and offshore disposal with respect to sediment starvation of coastal systems must be considered.
- Next, ineffective dredging and disposal may be one of the greatest fixed operating costs of a port authority. It has priority to find better and sustainable methods or solutions to reduce siltation processes of their basins.
- Finally, environmental legislation, coupled with revised definitions of "bio-availability" of contaminants, further motivates a drive towards alternative approaches.

1.1.1.1. Examples.

The Ports of Haaften and IJzendoorn, in the River Waal, see *Figure 1.1* and *Figure 1.2*, are two of the several harbours in The Netherlands which present siltation problems.

River Waal is the main distributary branch of river Rhine flowing to the central Netherlands for about 80 km before joining the river Meuse near Woudrichem. It connects the Rotterdam harbour with Germany. The river carries 65% of the total flow of the Rhine. The river Meuse rises in France and flows through Belgium and the Netherlands before draining into the North Sea with a total length of 925 km.

Table 1.1 shows annual dredging rates in some harbours along rivers Waal and Meuse (taken from *Barneveld et al, 2007*). The dredging costs of all marinas was estimated at about 500 M€ in The Netherlands in 2001.

However, not only The Netherlands presents serious problems of harbour siltation, other harbours from all over the world show high dredging costs and siltation problems as well. In the Port of Hamburg, the largest tidal port in Germany, about 2.6 Mm^3 of sediments are dredged annually, where mud represents 1 million cubic meters of this amount.

Port	**River**	**Km**	**Type**	**Area (ha)**	**Annual Dredging Rate (m^3/year)**
Lobith	Bovenrijn	863	Recreative	12	3,000
*IJzendoorn**	Waal	908	“”	51,5	29,000
*Haaften**	Waal	936	“”	26	3,000
Pieterplas	Maas	10	“”	15	4,500
Belfeld	Maas	100	Outer harbour	14 +11	18,000
Sambeek	Maas	147	Outer harbour	14 +11	8,000
Heusden	Maas	229	Industrial Harbour	13,4	2,000
Amercentrale	Bergsche Maas	251	Industrial Harbour	45	13,000

Table 1.1. Examples of dredging rates in The Netherlands.

Figure 1.1. Port of Haaften, River Waal. The Netherlands.

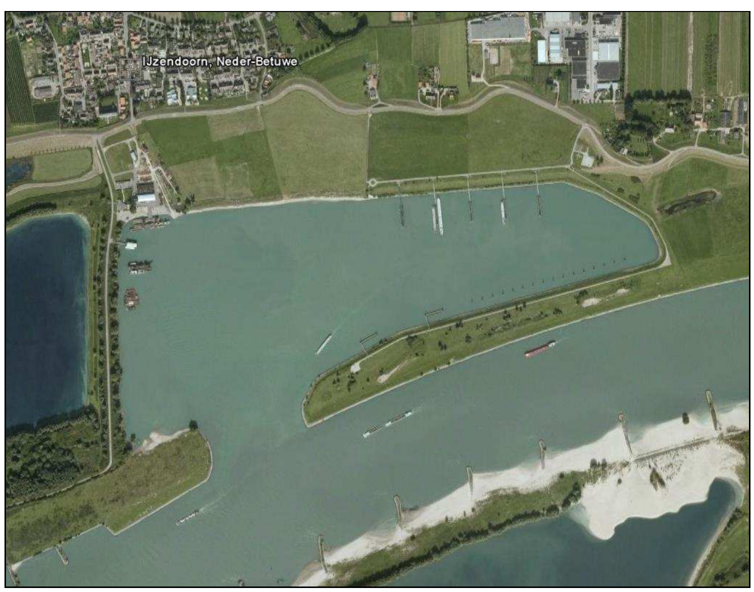

Figure 1.2. Port of IJzendoorn, River Waal. The Netherlands.

1.2. Aim of the present project.

Despite the relevance for such practical applications, little is known of the flow in the harbour entrance to use tools to predict siltation of harbour basins.

In the present project the influence of the location of a sheet of piles on the velocity field at the entrance of a harbour is examined by means of laboratory experiments in a scaled model.

These experiments have provided a data set through which a numerical model for the flow and transport in harbour entrances has been tested.

The study objectives of this graduation project are:

- To devise modifications of the characteristics of the system of piles, as a measure to reduce the exchange between harbour and river.
- To find out the effect of the application of pile groyne structures in different locations on the flow and siltation exchange.
- To establish what the accuracy of the numerical model is in this situation.

1.3. Approach in the present research-project.

Laboratory measurements were performed to study the influence of the geometry and location of a system of piles on the exchange between harbour and river. These experiments were performed by means of a schematized physical model of a river with a harbour basin which was built in a laboratory flume.

The scaled model was developed at the Fluid Mechanics Laboratory of the Department of Civil Engineering at Delft University of Technology.

The data gathered from the experiments were used to test the results of a numerical model called *FinLab*, which has been developed by R. J. Labeur (Faculty of Civil Engineering and Geosciences, Delft University of Technology).

1.4. Report organisation.

The basic physical processes that govern siltation in harbour basins are shown in Chapter 2. An overview of mechanisms of exchange of matter and the development of systems to reduce siltation exchange, their applications and other aspects of the use of pile groynes are given in this chapter.

Basic concepts of turbulence and mixing layers are described in Chapter 3, together with other theoretical questions related with shallow water flows.

Chapter 4 summarizes the main characteristics of the laboratory experiments. The flow conditions, the equipment and the performance of the different series are shown.

The data analysis and experimental results are discussed in Chapter 5.

The numerical simulations and the comparison between the results of the data analysis and the numerical model are included in Chapter 6.

Finally, Chapter 7 presents the conclusions and recommendations of this project.

CHAPTER 2.

THEORY. EXCHANGE AND HARBOUR SILTATION.

This chapter is subdivided in two sections. First, general considerations are made in relation with exchange processes in harbour basins and the flow along the harbour entrance. Second, the different approaches to reduce siltation exchange are presented and the current measures to reduce exchange by horizontal entrainment are described, including the use of pile groynes.

2.1. Introduction.

The exchange due to a steady flow in the river has been studied extensively, but the reduction of the exchange between harbour and river and the change induced in the flow pattern at the entrance by the location of piles upstream the harbour entrance has not been studied widely.

In order to determine the siltation rate in a harbour or develop a measure to reduce harbour siltation, it is important to identify the processes that bring the sediment into the harbour.

In general, suspended sediment is transported through the harbour entrance and into the harbour by exchange, where relatively low flow velocities ensure its deposit.

The dominant exchange process depends on the water system. In lakes and upstream stretches of rivers, horizontal entrainment is almost always the most important exchange mechanism. Tidal effects and density currents generally do not occur in these situations, but the latter can play an important role for marinas located further downstream.

To study the flow characteristics at the entrance of a harbour located in a stream it is necessary to consider the main aspects of shallow flows and their relevant features.

2.2. Exchange processes in harbour basins.

In this section, the most significant aspects related with exchange between harbour and river are described.

There are three main processes that determine this exchange of matter, according to *Langendoen (1992)*:

1) the velocity difference between the flow in the river and the resulting gyre at the harbour entrance,
2) a net flow through the entrance, and,

3) a density-driven exchange flow.

Other mechanisms that produce exchange, like wind and shipping, are of minor importance, according to *Langendoen (1992).*

The basic flow mechanisms are discussed in section 2.2.1 and some concepts related with siltation theory are presented in section 2.2.2. Section 2.2.3 presents an introduction of the flow behaviour at the entrance of a harbour basin adjacent to a river stream.

2.2.1. Basic exchange mechanisms.

Basins are relatively quiescent, due to this characteristic, they are susceptible to siltation. Sediment-rich water enters the basin and these sediments tend to settle due to low basin flow velocities.

Consequently, basin water is exchanged with sediment laden waters outside the basin through the harbour entrance.

Flow exchange mechanisms include horizontal entrainment, tides and density currents. Horizontal entrainment will be described more extensively. The other two processes will be briefly discussed below.

Accordingly with these different processes, the rate of exchange, Q, between a basin and surrounding waters is governed by a number of potential exchange flow mechanisms and it can be divided in the following terms: horizontal entrainment Q_e, tidal filling Qt, salinity density currents Q_d, temperature density currents Q_T, and sediment–induced density currents Q_s.

a) Horizontal entrainment (mixing layer) Q_e.

Any harbour basin located along flowing water presents exchange by horizontal entrainment, denoted by Q_e. Many harbours consist of semi-enclosed basins and model geometries are shown in *Figure 2.1.*

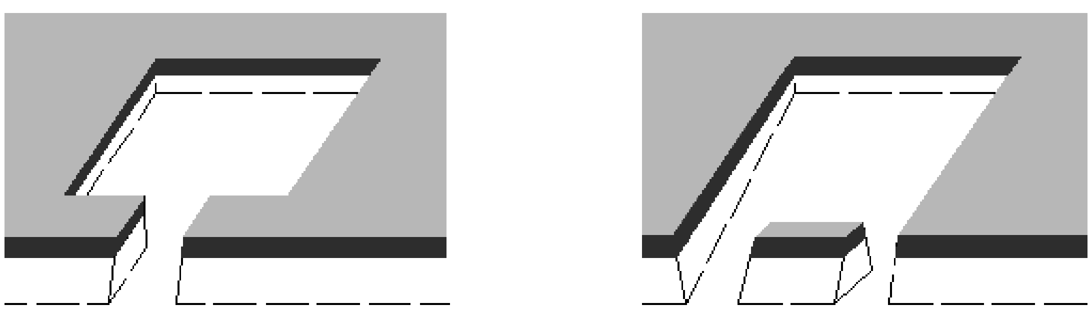

Figure 2.1 Single (a) and multiple-entrance (b) semi-enclosed harbour basins. Adapted from Headland et al, 2007.

The geometry of the harbour entrance can present different configurations. The mouth of the basin may be aligned with the river embankment, as in *Figure 2.1*, or may have protruding breakwaters, protecting the harbour from waves.

Examples of the first configuration are the Ports of Ijzendoorn and Haaften (The Netherlands) as it is given in Chapter 1.

The advantage of single-entrance basins is that they do not have net flow, on the contrary they are subject to three dimensional circulation patterns for this configuration (for instance, horizontal and vertical eddies and layered density currents) are present.

During the experiments in the laboratory, the geometry of the scale model corresponds to the form sketched in *Figure 2.1.a.*

The exchange flow by horizontal entrainment Q_e occurs as in *Figure.2.2.* The strength of the mixing layer (level of turbulence) is governed by the upstream corner geometry and downstream corner stagnation point, and governs the entrainment rate:

$$Q_e = f_e \, A \, u_r \tag{2.1}$$

where A is the cross sectional area of the harbour mouth and u_r is the river velocity along the streamwise direction. The exchange coefficient f_e depends on the harbour mouth configuration and local flow patterns. Typical values for f_e range from 0.01 to 0.03, depending on the angle of the downstream corner of the harbour basin *(Booij, 1986)*. Nevertheless, for unfavourable configurations, f_e may be up to an order of magnitude larger.

As it is shown in *Figure.2.2* the river flow separates at the upstream corner of the basin and forms a wake or turbulent mixing layer, which reaches the opposite corner of the basin. A gyre is formed within the harbour mouth by entrainment and stagnation processes; the dividing stream line is deflected into the basin because of energy losses in the wake.

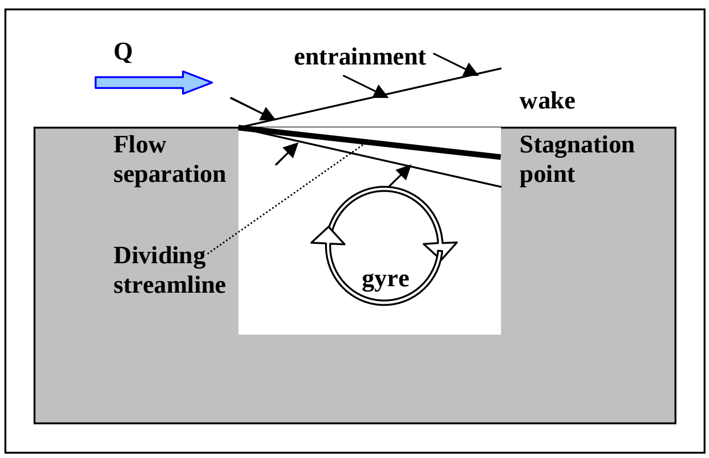

Figure 2.2 Sketch of exchange flow.

This mechanism will be described widely in section 2.2 and Chapter 3.

b) Tidal filling Q_t.

The tidal filling exchange flow rate Q_t can be computed from the tide amplitude â, the basin area, S, and the tidal period T. It is assumed that the tidal filling exchange flow rate follows the next expression:

$$Q_t = 2 \, \hat{a} \times S \times T \tag{2.2}$$

Tidal filling and entrainment flows cannot simply be added to obtain the overall exchange rate as the mixing layer will be advected into the harbour mouth during tidal filling.

c) Salinity Q_d, temperature Q_T, and sediment–induced density currents Q_s.

Density current exchange can be very significant in some harbours and results from gradients in salinity, water temperature or sediment concentration.

Density currents can be generated by fresh (or warm) water releases in the basin or as a result of density variations in the ambient water. The discharge of cooling water within a harbour basin will have a dramatic effect on the exchange flow rate. As a rule of thumb, the exchange flow rate amounts from three to five times the cooling water discharge.

Density currents are generated by horizontal pressure gradients induced by salinity, temperature or sediment concentration gradients. It should be noted that vertical stratification of the ambient water increases gravitational circulation, but does not generate this circulation.

Gravitational circulation is important for sediment transport because of the net near-bed up-estuary net transport, where suspended sediment concentrations are relatively high.

The previous mechanisms will influence the exchange depending on the characteristics of the surrounding ambient. During this thesis, exchange flow by horizontal entrainment will be considered, disregarding the other exchange processes.

2.2.2. Siltation equations.

2.2.2.1. Exchange of matter.

As a result of the roll-up of the wave-like disturbances, fluid from the harbour and the river is entrained into the mixing layer.

When the water in the shear layer flows against the downstream sidewall of the harbour, part of it flows into the river and a part of it into the harbour.

Since water from the harbour is being transported into the river and river-water is being transported into the harbour, exchange of matter will occur if the entrained fluid contains solutes or constituents.

2.2.2.2. Siltation rate through a harbour entrance.

As it has been mentioned in the previous sections, the exchange of matter between a harbour and a river takes place through the mixing layer.

The rate of exchange, Q, between a basin and surrounding waters is governed by a number of potential exchange flow processes. These processes can be divided in: horizontal entrainment Q_e, tidal filling Q_t, salinity density currents Q_d, temperature density currents Q_T, and sediment–induced density currents Q_s.

As it has been explained in Section 2.2, exchange by horizontal entrainment will be discussed in particular.

Harbour basin siltation rates can be computed by means of a zero-order method. This method has a disadvantage, since the accuracy of this approach decreases with increasing basin size. It is based to a large extent on the work by *Eysink (1989)*.

The zero-order approach is based on the mass balance equation for the schematized harbour basin sketched in *Figure 2.3.*

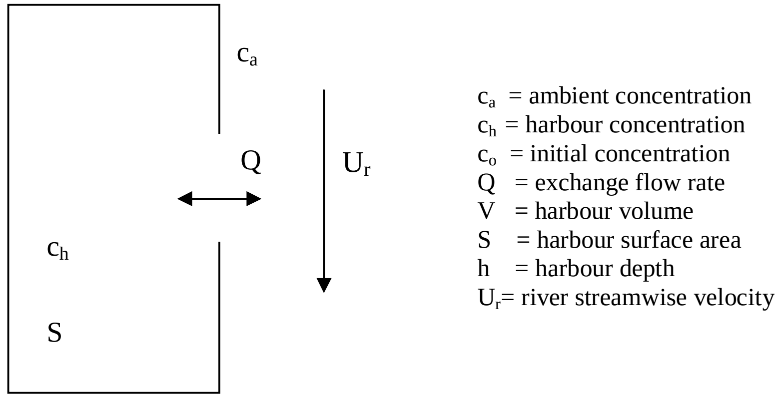

Figure 2.3 Schematic harbour basin.

This basin has a surface area S and depth *h*; the harbour volume amounts to:

$$V = S \times h \tag{2.3}$$

The suspended sediment concentration averaged over the harbour volume is denoted by c_h. The suspended sediment concentration in the ambient water system is denoted by c_a, which may vary with time but at another time scale than, c_h; therefore, it is treated as a constant.

The exchange flow rate between the river and the harbour basin is given by Q. The harbour basin is assumed to be perfectly mixed with small tidal variations.

If now horizontal entrainment is considered, the horizontal exchange rate between a harbour basin and an adjacent river can be approximated as follows:

$$Q_e = f_e \cdot A \cdot U_r \tag{2.4}$$

where:

Q_e = exchange flow from horizontal entrainment.
f_e = exchange coefficient.
A = harbour entrance area.
U_r = river velocity.

According with this formulae, for a harbour as a whole an exchange coefficient, f_e, can be established. This coefficient, f_e, depends on the geometry of the harbour entrance.

For a downstream angle of 90 degrees, the exchange coefficient is 0.03.

Once the exchange flow from horizontal entrainment is known, the following simplified equation gives the siltation rate in the harbour basin:

$$\textit{Siltation rate} = p \times Q_e \times c_a \tag{2.5}$$

where *p* is the basin trapping efficiency, Q_e is the previous exchange rate of water between the harbour basin and surrounding water and c_a is the ambient suspended sediment concentration outside the harbour.

2.2.3. Flow along the harbour entrance.

A flow along the entrance of a harbour generates an exchange of water between harbour and river. The velocity difference between the flow in the river and the gyre in the harbour entrance produces the generation of a mixing layer which is present at the transition from harbour to river.

The velocity difference along the entrance results from the separation of the flow in the river at the upstream corner of the harbour entrance. Transport of matter occurs from harbour to river and vice versa through the mixing layer.

It can be assumed that the water velocity in the river is constant outside the mixing layer and the water velocity in the mixing layer is smaller than that of the river, as a result, conservation of mass implies that the separating streamline at the upstream corner of the harbour entrance is directed into the harbour and reaches the downstream sidewall of the harbour at the stagnation point, inside the harbour basin, as it is shown in Figure 2.2.

The streamline separates the part of the water of the mixing layer which flows into the river and the other part which flows into the harbour at the stagnation point, near the downstream corner of the harbour entrance.

These amounts of river-water and harbour-water determine the location of the stagnation point. A wider mixing layer, as a consequence of a higher entrainment of river-water and harbour-water, results in a location of the stagnation point further into the harbour.

In addition to the existence of a mixing layer along the harbour entrance, a circulation flow takes place in the harbour basin as an effect of the entrainment of harbour water into the mixing layer and the supply of water from the mixing layer to the harbour at its downstream sidewall.

These two aspects (the mixing layer at the transition from harbour to river and the gyre in the harbour basin) are important for the transport of matter from the river to the harbour and in the harbour itself. The next subsections describe these aspects.

2.2.3.1. The mixing layer.

As it was described previously, the flow in the river separates from the bank at the upstream corner of the harbour entrance. A clear transition then is present from the flow in the river to the flow in the harbour near the separation point.

Because a system of two parallel streams with different flow velocities is subject to Kelvin-Helmholtz instability, wave-like disturbances arise that grow in the downstream direction and roll-up to become vortices that form a mixing layer.

The width of the mixing layer increases as a result of vortex pairing and the growth of large coherent eddies.

It is found from experiments, see *Langendoen (1992)*, that a plane mixing layer between two uniform parallel streams spreads linearly. This corresponds to the theory that the flow in the mixing layer approaches self-similarity after some distance downstream of the separation point.

The mixing layer is the most relevant aspect related with exchange processes for the present study. Hence, a more detailed theoretical description of the mixing layer is given in chapter 3, together with basic concepts of turbulence theory.

2.2.3.2. Gyres within the harbour basin.

Several gyres and dead zones can be present in a harbour. The number of gyres and their pattern depend greatly on the geometry of the harbour basin and the entrance.

The first gyre present inside the harbour basin is labelled Primary. Secondary and more gyres occur in harbours with a length to width ratio L/B>2. A sketch is shown in *Figure 2.4* (adapted from *Langendoen(1992)*).

On the contrary, for a length to width ratio from 0.5 to 2 only one gyre is created in the harbour.

The scale model used during the laboratory experiments will show a length to width ratio lower than 2, as a consequence, only one gyre will be developed at the harbour entrance, but other gyres will be present at the harbour owing to the lay-out of the basin (the geometry of the scale model will be described in Chapter 4).

In relation with the length of the gyre, it does not become much larger than 1.5B for harbours with a length to width ratio higher than 2, L/B>2, and their entrances perpendicular to the river axis.

The length of the primary gyre will be larger for entrances oriented at an angle α less than 90 degrees with respect to the river axis, and smaller for entrances oriented at an angle larger than 90 degrees.

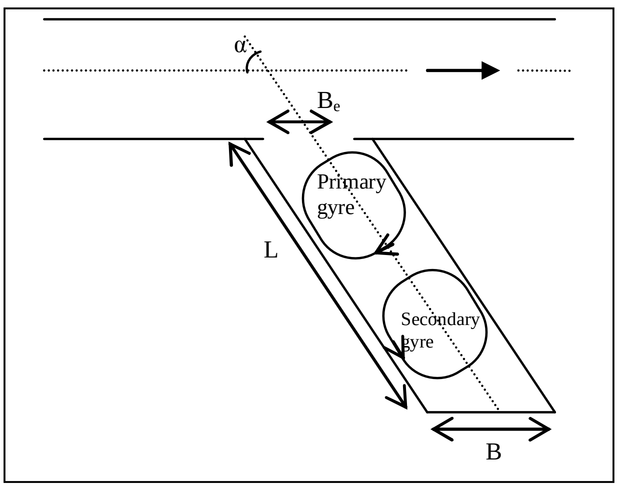

Figure 2.4 Definition sketch of gyres inside the harbour basin. Langendoen (1992).

According to *Langendoen (1992),* the width of the flow from the mixing layer into the harbour is about 20 percent of the width of the harbour. The flow increases in width in the flow direction of the gyre. The water velocity in the gyre is largest near the downstream sidewall, and decreases in the flow direction of the gyre.

A secondary flow exists at the gyre, as a consequence of the curved flow; the strength of this secondary flow will depend on the water depth. The secondary current consists of a flow towards the centre of the gyre near the bottom, and a flow in the opposite direction near the free surface.

The secondary current is crucial for the sediment transport in the harbour. Small sediment particles will rotate towards the centre of the gyre and deposit because the low water velocities near the centre.

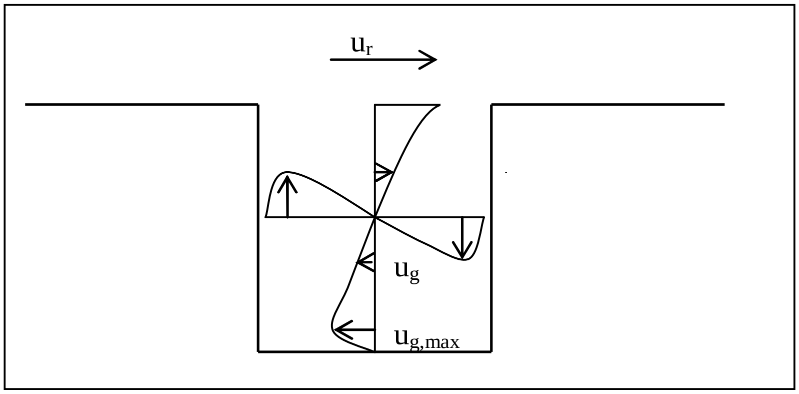

Figure 2.5 Velocity profiles along the central axes of a square harbour. Langendoen (1992).

The secondary current also transfers momentum and therefore it may be important for the development of secondary gyres in the harbour.

This aspect may possibly account for the fact that most depth-averaged numerical models are not capable of predicting secondary gyres.

2.3. Methods to reduce exchange.

In this section, different methods to reduce harbour siltation will be described in the first section. Second, two measures to reduce sediment exchange by horizontal entrainment will be considered, together with an example of a case of study carried out by *Van Schijndel and Kranenburg (1998)*. The advantages and drawbacks of the use of pile groyne systems to reduce siltation exchange will be discussed in the last section.

2.3.1. General.

Exchange processes have been studied during decades and this has led to the development of a number of measures to reduce siltation, ranging from simple methods based on research to complex measures involving scale modelling.

There are different methods to reduce the exchange between a harbour and a river. For instance, maintenance can be avoided or minimized by locating harbours in naturally deep waters or by implementing measures for minimising harbour siltation. These measures are called MHS measures.

The simplest method to reduce harbour siltation would be the construction of a narrow entrance.

The use of only one of the entrances of the port is other measure to take into account for minimizing siltation. Other possibility would be a change in the orientation of the harbour entrance, because it has been demonstrated the exchange rate is lower when the entrance is situated with a certain angle with respect the direction of the river. The last and the most recent option is the use of structures to modify the behaviour of the mixing layer.

When it is not possible to modify the features of the harbour entrance, the application of structures is the most appropriate solution.

The aim of this project is the study of this reduction by means of the use of a pile array on the upstream side of the harbour entrance.

More complex measures are a current deflecting wall (CDW) or a curved sill at the harbour entrance.

2.3.2. Minimizing Harbour Siltation (MHS) approaches.

The subsequent sections describe the different measures to reduce siltation exchange. The different approaches to reduce or minimize harbour siltation are called MHS. There are three basic categories to siltation minimization in relation with MHS approaches *(Headland et al, 2007)*:

1. KSO: These methods keep sediment out.
2. KSM: Methods that keep sediment moving.
3. KSN: Methods to keep sediment navigable.

The first type of measures, KSO strategies, focuses on minimizing penetration by sediment laden waters that enter harbour basins.

In contrast, KSM strategies are centred on maximizing flow velocities in quiescent areas to prevent sediment from settling.

KSN strategies take advantage of the ability of ships to sail close to the low density fluid mud often located at the bottom of a basin.

A distinction can be made between passive and active measures from the first two categories. Some examples of passive measures are submerged sills, flow training structures, etc. which do not require energy or moving parts. Movable gates, locks and flow augmentation are cases of active measures.

The first approach, KSO, can involve barriers, like dikes or sills, as well as entrance modifications and traps. Some examples of these measures are narrow entrances, training structures, shallow entrances, horizontal eddy reduction, gates and curtains, pneumatic barriers or air curtains. These strategies are generally best suited to relatively calm basins where KSM are not possible.

The KSM approach can incorporate flow training structures (i.e., conventional dikes, submerged dikes, sills) or flow augmentation. In the field of flow augmentation measures, there is a wide range of possibilities, like channel realignment to take advantage of higher velocity areas, channel diversion to redirect flow towards a low velocity area, or application of scour and propeller jets that increase flow velocities mechanically.

2.3.2.1. KSO & KSM semi-enclosed basins.

As it was given in (2.6), the basin sedimentation is governed by the following simplified equation:

$$\textit{Siltation rate} = p \times Q_e \times c_a$$

Basin sedimentation can be diminished by reducing one of the previous three parameters: the basin trapping efficiency, p, the exchange rate Q_e or the ambient suspended sediment concentration outside the harbour, c_a.

KSM measures can be used to reduce p and KSO measures for reducing Q or c_a.

2.3.2.2. KSO by reducing through flow.

One example of KSO measures is the port of Bremen in German. The second entrance of this harbour was closed to eliminate the through-flow and sedimentation was reduced.

2.3.2.3. KSM by reducing trapping efficiency, p.

Trapping efficiency is generally difficult to decrease, but it can be achieved with an increase in basin circulation.

It is possible to diminish p by means of reduction in residence time (i.e., $T_h = \frac{V}{Q_e}$), but normally only slightly, as computed by *Eysink (1989):*

$$p = 1 - \exp\left\{-\frac{W_s}{h}\left(\frac{1-\frac{u^2}{u_c^2}}{u_c^2}\right)\cdot T_h\right\}$$

(2.6)

where:

W_s = sediment settling velocity.

h = basin water depth.

u = average basin velocity.

u_c= critical velocity for sedimentation.

T_h = horizontal residence time V/Q_e.

V = basin volume.

Q_e = discharge through harbour entrance.

The ratio of $\frac{u}{u_c}$ is generally <<1, therefore the trapping efficiency is determined by the ratio of T_h to vertical residence time, ($T_v = \frac{h}{W_s}$).

When $T_h > 4\cdot T_v$, all of the sediment entering the harbour will be trapped.

A reduction in p attends a reduction in the residence time T_h, however it can only be reduced with an increase in Q or with a reduction in harbour volume, V. Significant reductions in T_h are necessary to diminish trapping.

Unfortunately, an increase in Q will bring more sediment to the basin, with the exception of the case when other source fills the basin with clear water.

2.3.2.4. KSM by reducing suspended sediment concentration, c_a.

It is generally difficult to reduce c_a due to this value is normally dictated by regional scale processes and the suspended sediment concentrations in the surrounding area.

It is possible to reduce c_a by preventing near bottom waters from entering a harbour because high sediment concentrations are found near the bed. Sills and walls are used as flow blocking structures.

One of the simplest and most cost-effective methods of reducing c_a at semi-enclosed basins is by the sill which is a component of entrance flow optimization (EFOS).

2.3.2.5. KSM by reducing horizontal entrainment flow.

As it was shown in Section 2.2, the horizontal exchange rate between a harbour basin and an adjacent river can be approximated as follows:

$$Q_e = f_e \cdot A \cdot U_r$$

where:

Q_e = exchange flow from horizontal entrainment.
f_e = exchange coefficient.
A = harbour entrance area.
U_r = river velocity.

From these expression, Q_e can be decreased by reducing either A or f_e. The harbour entrance area, A, must be large enough for safe navigation, so this aspect limits its reduction. Reducing f_e requires entrance geometry modifications designed at lowering entrainment rate.

In order to satisfy this reduction, the upstream corner of the harbour entrance can be modified by means of structures such as a pile array groyne or a current deflecting wall. These methods are described in the following section.

2.3.3. Measures to reduce horizontal entrainment flow.

As it was discussed previously, the horizontal exchange rate between a harbour basin and an adjacent river can be approximated as it has been stated in equation (2.4). To reduce f_e, geometry modifications of the entrance can reach a lower entrainment rate.

Sections 2.3.3.1 and 2.3.3.2 will explain two different measures: the current deflecting wall (CDW) and the pile array groyne. The last measure will be studied during the laboratory experiments.

2.3.3.1. Current Deflecting Wall (CDW).

A successful method to reduce horizontal entrainment flow has been patented by Dr. H. Christiansen and it is known as the current deflecting wall (CDW) or, on grounds that more than only walls are involved, entrance flow optimization structures (EFOS). With this measure, f_e is significantly reduced.

An up-estuary corner modification is shown in *Figure 2.6.*

The objective of the CDW is to form river-directed currents rather than stagnation or basin-directed currents, so diverting the entrainment mixing layer away from the entrances as shown in *Figure 2.6.*

The CDW consists of three parts: a curved training wall, a channel between the training wall and the shoreline, and a sill sited at the down-estuary end of the wall.

The wall curvature acts to reduce the strength of the mixing layer and flow entrainment. Depending on the CDW design, the mixing layer can be pushed into the channel, in that way the stagnation point at the up-estuary corner of the entrance is eliminated.

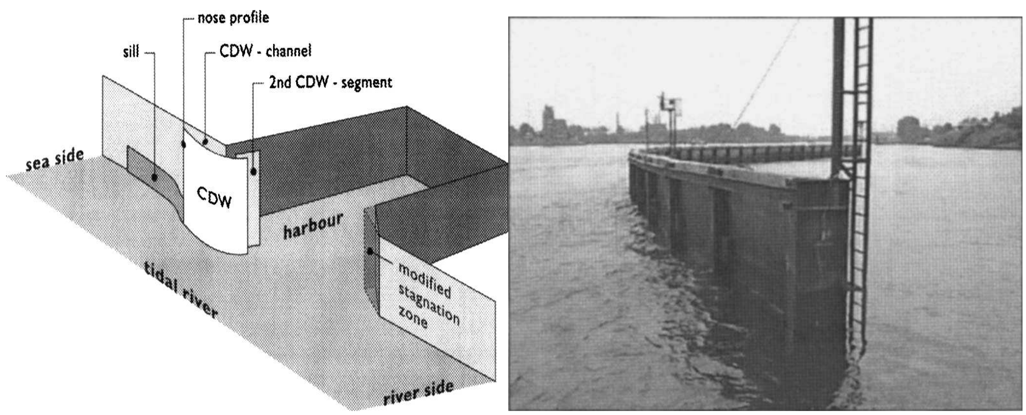

Figure 2.6 Sketch of a current deflecting wall and CDW of Köhlfleet harbour. (Winterwerp 2005).

The sill between the CDW and the shoreline, located at the so-called "CDW inlet", acts to intercept the high concentrations of suspended sediment near the bed. Consequently, the sediment concentration, c_a, entering the harbour is reduced.

In addition, the CDW facilitates all tidal filling of the basin through the channel that exists between the CDW and the shoreline, rather than through the harbour entrance. Due to the presence of the sill, the basin is only filled with relatively clear surface water.

CDW systems have near-and far-field effects. Some of these properties are:

1. Reduction in silt input and retention by 40-50%.
2. Operate whenever there is a flow.
3. There is no transfer of deflected sediment into adjacent basins where these are present.
4. CDW does not present moving parts and it does not need more maintenance than other harbour walls.
5. Reduced input rate may permit bed sediments to be colonized by invertebrates not able to cope with high rates of bed elevation change.

Far-field:

1. Reduction on the impact and prolonged lifespan of disposal sites and disposal areas.

As an example of this measure, a CDW with a length of 150 m was constructed near the entrance of the Köhlfleet harbour basin, located seawards of the Parkhafen, Hamburg, in 1991, with the purpose to minimize sediment input to the basin. This CDW is given in Figure 2.7.

Extensive hydraulic scale model tests were performed at the Franzius Institut in Germany to establish the design of the CDW for this harbour. The CDW confirmed its value over the years reducing the dredged quantities in the Köhlfleet by approximately 40% (for more details see *Christiansen and Winterwerp, 2005*).

2.3.3.2. Pile groyne structures.

The mixing layer strength can be reduced by lowering the velocity gradient between the river and the harbour basin. For this purpose, a pile groyne can be installed upstream a harbour entrance as it is drawn in *Figure 2.7.*

A pile groyne consists of an array of piles from the riverbank into the river perpendicular to the flow, a little upstream of the harbour mouth, as it is sketched in Figure 2.7.

The sheet acts to smooth the transition in velocity between the river and the primary gyre at the harbour basin. It reduces the cross-flow velocity gradient; as a result it reduces the strength of the mixing layer and entrainment rates.

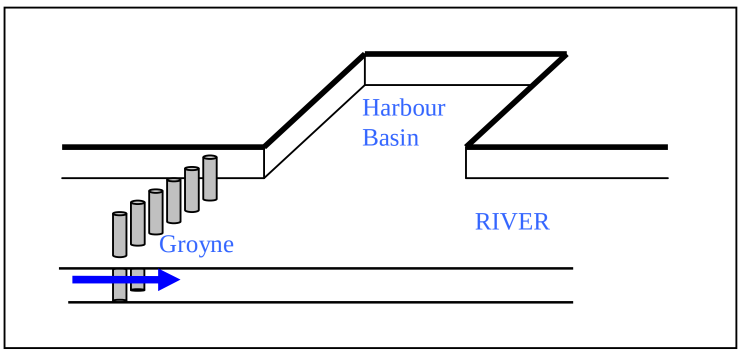

Figure 2.7 Pile groyne located at the upstream corner of a harbour basin.

A further description of the characteristics of pile groyne systems and their features is given in Section 2.3.4.

2.3.3.3. Example of reducing siltation measures."'t Steel/la Bonne Aventure marina"

In this subsection, a real case of the development of siltation-reducing measures for harbours situated along rivers is shown. A study of different methodologies was performed for the marina *'t Steel/la Bonne Aventure* by *Van Schijndel and Kranenburg (1998).* A sketch is given in *Figure 2.8.*

This marina is located on the right bank of the River Meuse, near the city of Roermond, The Netherlands. It has a length of about 700 m and a width of about 1,500 m, and its mouth is around 70 m wide and 7 m deep.

The river flow rate is controlled by rainfall in its catchment area and a large number of sluices along its course, and it differs between 10 and 3,000 m^3/s, with a long-term average of 250 m^3/s. The local mean water depth is about 5 m. The mean load of fine sediments is estimated at about 500 kton/year.

The marina was separated from the river by a recreation field upstream of its mouth and a training dam downstream; the field and dam are both flooded during high river flows.

The flow field in the marina is characterized by a primary eddy in its mouth and a secondary, low-energy eddy in the remaining part of the marina.

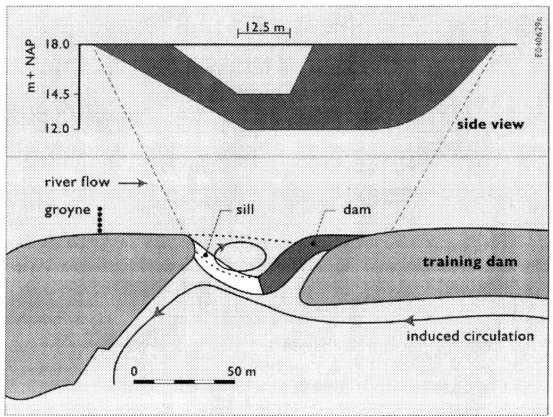

Figure 2.8 Plan of the ‘t Steel/la Bonne Aventure marina along Meuse River.
(Van Schijndel and Kranenburg, 1998).

The study was carried out in the Laboratory of Fluid Mechanics of the Delft University of Technology, The Netherlands, in a physical scale model with an undistorted length scale of 1:50. An undistorted model was chosen because it properly reproduces the vertical flow structures in the harbour mouth.

The exchange flow rate between river and basin was measured with the use of hot water as tracer.

A large number of siltation-reducing measures were studied. Two aims were establish to be verified from the experimental results, i.e.:

- Reduction of entrainment by a current deflecting wall and by a permeable pile groyne, and
- Reduction of the cross section of the harbour entrance by a sill.

The reduction of the cross section of the entrance was an option in this case, because the cross section was oversized for its purpose, i.e. access of yachts.

It was found by trial end error that the sill could reduce the induced entrainment considerably, but its efficiency appeared strongly dependent on its specific layout.

The efficiency of the various measures was quantified through the exchange coefficient f_e measured in the model and a reduction factor R, defined as $R = \dfrac{Q_e}{Q_{e,0}}$, where index 0 refers to the original configuration. The results are set in *Table 2.1.*

Despite of the high percentage of reduction for a permeable pile groyne together with a curved sill (R=0.1), the final solution did not include the construction of a pile groyne structure as it was difficult to get permission of the managing authorities to build a pile groyne in the river, as the authorities were afraid that this would affect the capacity of the river.

For this reason, from the results obtained by the study, the construction of only a curved sill and reduction of the harbour entrance was recommended.

Parameter	f_e	*R*
Original configuration	$1.8{\cdot}10^{-3}$	1
Current deflecting wall	$1.4{\cdot}10^{-3}$	0.8
Permeable pile groyne	$8.5{\cdot}10^{-4}$	0.5
Straight sill	$1.7{\cdot}10^{-3}$	0.7
Sill curved to shape of primary eddy	$1.2{\cdot}10^{-4}$	0.3
Permeable pile groyne + curved sill	$3.5{\cdot}10^{-4}$	0.1

Table 2.1 Efficiency of siltation reducing measures for't Steel/La Bonne Aventure Marina.

2.3.4. The use of pile groynes as a measure of reduction.

2.3.4.1. Current applications.

Permeable pile groynes have been used widely in coastal engineering. They have been built on the southern shores of the Baltic Sea in large numbers for years. Pile groynes act as a hydraulic roughness on the longshore current. They reduce the littoral current and the velocity differential between the velocity seaward and in the pile groyne fields is smaller than with impermeable groynes.

Moreover, pile groynes are one of the most frequently used permeable groynes for controlling the erosion of river banks. Pile groynes have been used in river engineering to reduce the flow velocity near the river banks and cause deposition of sediment and bank stability. Sediment trap efficiency of pile groynes depends on their opening and flow and sediment conditions.

The idea of using pile groyne systems for reducing harbour siltation starts from the last concept. In this case, the aim of the structure is not blocking the sediment transport along the river as it occurs in bank stabilisation; otherwise, the objective is to modify the flow behaviour along the harbour entrance in order to reduce the velocity gradient between river and harbour.

After several studies (see example in previous section from the study of *Van Schijndel and Kranenburg, 1998*), it was found that a permeable pile groyne placed upstream of the entrance can reduce the exchange substantially.

Some model tests have shown that a permeable pile groyne can reduce f_e on the order to 50%. In addition to this, combining the pile groyne with a sill or a CDW the exchange can be suppressed for the most part.

2.3.4.2. Advantages and drawbacks.

Despite of their great effect on the exchange rate, the use of pile groynes requires more study to determine the most suitable geometry for effectiveness on siltation reduction.

Appropriate choice of shapes, dimensions and location of piles is crucial, but effectiveness of the groyne depends also on their "permeability", that is the distance between piles.

The main hydraulic disadvantage of impermeable groynes is the effect of flow separation at the groyne head, caused by the blockage of the flow, resulting in high local velocities and scour. Therefore, special attention must be given to the toe protection at the head of the groynes, where severe scouring occurs. For this reason, a system of piles as a permeable groyne is considered to avoid this disadvantage.

Permeable groynes may be built of steel piles or reinforced concrete piles, which are driven into the riverbed and the flood plain, and they may consist of a single pile row or of several rows. In addition to current and wave attack, horizontal loads caused by floating debris must be considered in the design.

Steel groynes are constructed of vertical sheet piling, located perpendicularly to the river bank.

The main disadvantage of the use of permeable groyne instead of other measures as CDW or sills is the effect of the pile groyne on the capacity of the river. It should be taken into account to establish their characteristics and layout in order to prevent possible drawbacks for the navigation.

It should be noted that the groyne field have to be constructed with limited extent out from the river bank in order to improve vessel manoeuvrability around the structure and entry into the basin.

2.4. Summary.

The aim of this chapter has been to introduce the main concepts related with harbour siltation and the different measures that can be applied to minimize the exchange between river and harbour.

The second part has described several aspects in relation with methods to reduce harbour siltation. During this section abbreviations for MHS strategies have been used, namely: keep sediment out (KSO), keep sediment moving (KSM) and keep sediment navigable (KSN).

It is necessary to understand the physics that govern siltation in harbours in order to apply appropriate MHS strategies and develop a more extensive study on the use of specific measures as a pile groyne structure.

Semi-enclosed basins are common, especially along rivers, and for this reason the study of different methods to reduce their siltation problems has been developed during decades.

Pile groyne and CDW systems are the culmination of repeated efforts to resolve the conflict of interest between need for a wide entrance to admit vessels and need for a limitation to reduce silt trapping.

However, these methods will be inapplicable where basin exchange is entirely dominated by density.

Therefore, there is insufficient knowledge about these systems, and more research must be carried out to improve their results and find new methods.

The goal of this project is to perform new laboratory experiments to determine the effectiveness of pile groyne structures located upstream harbour basins and to optimize its geometry to reduce the exchange of sediment at the harbour mouth.

CHAPTER 3.

TURBULENCE AND SHALLOW MIXING LAYERS.

This chapter is divided in three sections. The first part is a brief introduction on turbulent flows. The second part deals with basic concepts about turbulence models and coherent structures. Finally, an overview is given of some basic and generally accepted theories and concepts about shallow water flows. The concepts presented in this chapter form the basis for the data analysis. Sources for this chapter are the lecture notes of *Uijttewaal (CT5312)* and theses by *Van Prooijen (2004), Langendoen (1992)* and other articles listed in the literature (see References).

3.1. Introduction.

Most flows in nature are turbulent. Turbulent flows can be found in rivers, channels, seas, at the atmosphere, at the boundary layer of airplanes or cars, etc.

Turbulence can be generated at walls or boundaries of a channel, at mixing layers and at other locations where the flow is disturbed as in wake flows or the surroundings of piles and other structures.

Figure 3.1 gives some examples of turbulent flows as it is mentioned in *Uijttewaal (2007).* The first two plots show typical examples of wall turbulence in the banks and the bottom of a channel. Wake flows and mixing layers are examples of turbulent flows due to free turbulence generated by the presence of structures or obstacles in the stream.

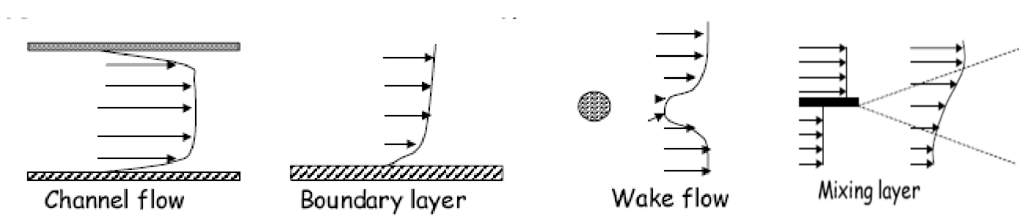

Figure 3.1.Examples of turbulent flows.

A first classification of turbulence can be based on the dimensionless Reynolds number Re, defined as the ratio between inertial and viscous forces of the flow. More specifically the definition is

$$\mathrm{Re} = \frac{UL}{\upsilon} \tag{3.1}$$

in which U (m/s) is a characteristic velocity, L (m) a characteristic length associated with U and ν (m^2/s) the kinematic viscosity of the fluid. The kinematic viscosity of water is ν = 0.01 cm^2/s.

The characteristic length-scale for a channel of width w and depth h is the hydraulic radius, R_h = w·h/P, where P is the wetted perimeter. For an open channel, with a rectangular cross section, the wetted perimeter is given by P = (2h + w).

The flow is considered to be laminar when the viscosity dominates the flow, but if the Reynolds number is large (Re>4,000) then inercial forces will dominate.

Turbulent flows present complicated and chaotic features, however they should not be considered as a random flow. Turbulent flows show organised motions and consequently, it can be described statistically with characteristic length and time scales.

Concerning with statistical properties, a stationary field will have statistical properties independent of time. Otherwise, a homogeneous field will present statistical turbulent properties independent of space. However, it is said that the turbulent flow field is isotropic, it has no preferred direction. For this reason, many theoretical turbulence studies are based on the hypothesis of homogeneous isotropic turbulence.

3.2. Basic concepts and turbulence modelling.

3.2.1. Navier-Stokes Equations.

During the following sections, the coordinate system will be (x, y, z) with x the streamwise coordinate, y the transverse coordinate and z positive upward. The velocity components will be (u, v, w).

For convenience, in this chapter, the coordinate system will be denoted by x_i and the velocity components by u_i, with i=1, 2, 3.

In order to describe the properties of turbulence, a velocity field given by (u, v, w) can be divided in two components: i.e., for the streamwise component, the mean motion will be $\overline{u}$ (the over-bar denotes a time average value) and the fluctuating part will be u' (defined as $u - \overline{u}$).

In the following, the fluctuating parts will be denoted by an apostrophe and the mean values will be denoted by an over-bar or by <>, as it was suggested by Osbourne Reynolds.

According with the previous concept, the instantaneous variables (for example velocity components and pressure) will be decomposed into a mean value and a fluctuating value, i.e.

$$u_i = \overline{u}_i + u_i' \quad \text{and} \quad p = \overline{p} + p' \tag{3.2}$$

The continuity equation and the Navier-Stokes equation for incompressible flow are given by

$$\frac{\partial \rho}{\partial t}+\frac{\partial(\rho u_i)}{\partial x_i}=0 \qquad (3.3)$$

$$\frac{\partial(\rho u_i)}{\partial t}+\frac{\partial(\rho u_i u_j)}{\partial x_j}=-\frac{\partial p}{\partial x_i}+[\mu\left(\frac{\partial u_i}{\partial x_j}+\frac{\partial u_j}{\partial x_i}\right)]_j \qquad (3.4)$$

where $(.)_j$ denotes derivation with respect to x_j.

The Navier-Stokes equations consist of a continuity equation and a momentum equation. The Navier-Stokes equations describe conservation of momentum. To discuss these equations, it can be assumed that the fluid is incompressible. Note that the term incompressible is used in the sense that density is independent of pressure, but it can be dependent on temperature or concentration.

3.2.2. Reynold’s Averaged Equations

Inserting equation (3.2) into the continuity equation (3.3) and the Navier-Stokes equation (3.4) it is obtained the *time averaged* continuity equation and Navier-Stokes equation

$$\frac{\partial \rho}{\partial t}+\frac{\partial(\rho \bar{u}_i)}{\partial x_i}=0 \qquad (3.5)$$

$$\frac{\partial(\rho \bar{u}_i)}{\partial t}+\frac{\partial(\rho \bar{u}_i \bar{u}_j)}{\partial x_j}=-\frac{\partial p}{\partial x_i}+[\mu\left(\frac{\partial \bar{u}_i}{\partial x_j}+\frac{\partial \bar{u}_j}{\partial x_i}\right)-\rho\overline{u'_i u'_j}]_j \qquad (3.6)$$

The term $\rho\overline{u'_i u'_j}$ is called the *Reynolds stress tensor* which is symmetric and contains nine components (normal stresses and shear stresses). It represents correlations between fluctuating velocities. It is an additional term due to turbulence and it is unknown. It is necessary a model for $\overline{u'_i u'_j}$ to close the equation system in equation 3.6.

This is called the *closure problem*: the number of unknowns (ten: three velocity components, pressure, six stresses) is larger than the number of equations (four: the continuity equation and three components of the Navier-Stokes equations).

3.2.3. Closure problem.

The equations can be closed by using the eddy viscosity concept or by solving a transport equation for the Reynolds stresses.

3.2.3.1. Boussinesq assumption.

To approximate a solution Boussinesq introduced in 1877 his turbulent-viscosity hypothesis. In *Davidson (2003)* this hypothesis is described.

The Reynolds stresses are linked to the velocity gradients via the turbulent viscosity: this relation is called the Boussinesq assumption, where the Reynolds stress tensor in the time averaged Navier-Stokes equation (3.6) is replaced by the turbulent viscosity multiplied by the velocity gradients.

An identification is made in the second term of (3.6)

$$[\mu\left(\frac{\partial \bar{u}_i}{\partial x_j}+\frac{\partial \bar{u}_j}{\partial x_i}\right)-\rho\overline{u'_i u'_j}]_j=[(\mu+\mu_t)\left(\frac{\partial \bar{u}_i}{\partial x_j}+\frac{\partial \bar{u}_j}{\partial x_i}\right)]_j \tag{3.7}$$

which gives

$$\rho\overline{u'_i u'_j}=-\mu_t\left(\frac{\partial \bar{u}_i}{\partial x_j}+\frac{\partial \bar{u}_j}{\partial x_i}\right) \tag{3.8}$$

where $\mu_t=\rho\upsilon_t$ and the dimension of υ_t is m^2/s.

3.2.3.2. Turbulent eddy viscosity concept.

As it was introduced previously, the eddy-viscosity concept consists of the assumption that the turbulent stresses are proportional to the mean velocity gradients. It represents the first step towards closure of the Reynolds-averaged Navier-Stokes equations.

A flow with a high turbulence viscosity has the capacity to transfer more momentum than a flow with a lower value. Consequently, more exchange will take place and the width of the mixing layer will be larger.

This is the case of a harbour basin adjacent to a river stream. In the region along the harbour entrance a mixing layer develops in which an exchange of mass, momentum and energy takes place.

3.2.4. Turbulence models.

There are different levels of approximations involved when closing the equation system in equation (3.6).

ALGEBRAIC MODELS: Algebraic model are based on the Boussinesq assumption. An algebraic equation is used to compute the turbulent viscosity, called eddy viscosity. Models which are based on an eddy viscosity are called *eddy viscosity* models.

ONE EQUATION. In these models a transport equation is solved for a turbulent quantity (usually the turbulent kinetic energy) and a second turbulent quantity (usually a turbulent length scale) is obtained from an algebraic expression. The turbulent viscosity is calculated from Boussinesq assumption.

TWO EQUATION MODELS. These models fall into the class of eddy viscosity models. Two transport equations are derived which describe transport of two scalars, for example the turbulent kinetic energy (k) and its dissipation (ε). The Reynolds stress tensor is then computed using an assumption which relates the Reynolds stress tensor to the velocity gradients and an eddy viscosity. The latter is obtained from the two transported scalars.

REYNOLDS STRESS MODELS. Here a transport equation is derived for the Reynolds tensor. One transport equation has to be added for determining the length scale of the turbulence. Usually an equation for the dissipation is used.

Above the different types of turbulence models have been listed in increasing order of complexity, ability to model the turbulence, and cost in terms of computational work.

3.2.5. Turbulence modelling in the present study.

The physical scaled model of the laboratory experiments will be modelled by means of a numerical model called *FinLab*. *FinLab* is a three dimensional, non-hydrostatic finite element model based on a tetrahedral mesh which is unstructured in all three dimensions. *FinLab* was created by Robert Jan Labeur and is being further developed at the TU Delft.

A simple model for channel flows is the Elder formulation, and it will be applied in *FinLab* to carry out the numerical simulations. The Elder formulation is given by:

$$\upsilon_t = \alpha u_* h \tag{3.9}$$

where the typical velocity scale is the friction velocity u_* and the length is the water depth, h. A complementary expression for the depth-averaged eddy viscosity υ_t is given by (*Van Prooijen ,2004)*:

$$\upsilon_t = \beta \cdot u_* \cdot h = \beta \cdot \sqrt{c_f} \cdot U \cdot h \tag{3.10}$$

where *U* is the depth-averaged streamwise velocity (capital letters will denote depth averaged values) and the parameter β could be considered the dimensionless eddy viscosity and it may range from approximately 0.07 to about 0.3. The bed friction coefficient is denoted by c_f .

The eddy viscosity is considered at the numerical model from the expression as follows:

$$\upsilon_t = \upsilon_0 + \beta \cdot u_* \cdot h = \upsilon_0 + \beta \cdot \sqrt{c_f} U \cdot h \tag{3.11}$$

where υ_0 and β will vary depending on the case.

The advantage of this formulation is that relatively coarse grids can be used with mesh sizes depending on the length scales of the mean flow, which are generally larger than the water depth. The disadvantage is that the dynamics of the horizontal structures is not represented, especially in complicated geometries.

3.3. Shallow mixing layers.

This section describes the basic concepts of shallow water flows, the main characteristics of the mixing layer which is developed at the harbour entrance and the coherent structures present in the mixing laxer.

3.3.1. Introduction to shallow water flows.

Mixing layers are found for example downstream of groyne tips in rivers and at confluences of natural streams. They occur at junctions where two flows with different velocities come together and, as it is the aim of this project, at the entrance of a harbour located in a river stream.

According to the characteristics of the physical model used in the laboratory experiments, this project is concerned with mixing layers in shallow flows: so called shallow mixing layers.

The domain of a shallow flow has two dimensions, namely the horizontal dimension in flow-direction and a direction transverse to the flow, both significantly larger than the third dimension (vertical dimension).

Shallow shear flows can be considered as a combination of two types of flow, according to *Van Prooijen (2004).* On one hand, they are *plane free shear flows* and on the other shallow shear flows are in the category of *open-channel flows.*

Within the first category the flows are principally uni-directional and yield a transverse gradient in the streamwise velocity. The streamwise velocity profile for a mixing layer is given in *Figure 3.2.a.*

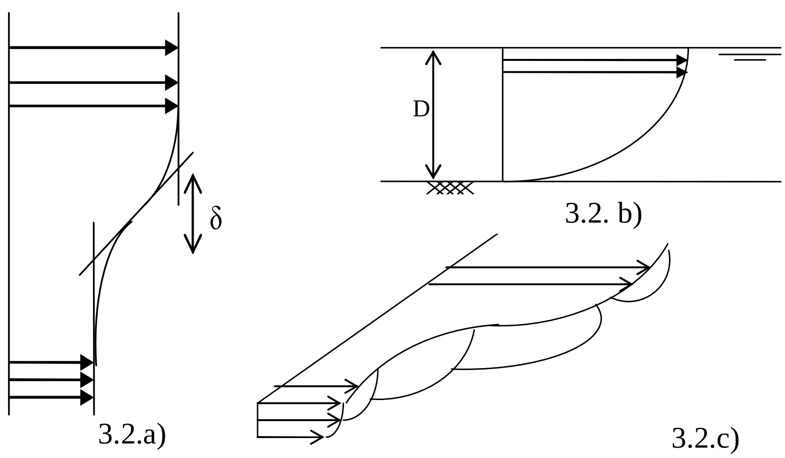

Figure 3.2. a) Mixing layer flow (top view). b) Wall flow (side view).
c) Shallow mixing layer flow. Adapted from van Prooijen (2004).

The mixing region between the high velocity side and the low velocity side becomes wider in downstream direction and the velocity gradient decreases due to the transference of momentum from one side to other. The velocity differences across the mixing layer and its width are the main parameters to define the mean velocity field.

With respect to the second category, a typical vertical profile of the streamwise velocity for an open channel flow is sketched in *Figure 3.2.b.*

A velocity gradient is created over the depth due to the no-slip condition at the bottom, where the flow is slowed down. In these flows, it is assumed that the water depth is not exceeded the dominant horizontal lengths scales.

Depending on the flow parameters, one of the two previous flows will dominate in a shallow water flow. In the category of shallow flows, neither the horizontal shear nor the bottom turbulence can be neglected.

3.3.2. Theoretical description.

As it has been described in a previous section, a mixing layer develops at the harbour entrance between a river and a harbour basin. The mixing layer forms a transition between the stream and the harbour basin and it is considered to be a typical case of shear flows.

This paragraph describes the modelling of the development of two-stream shallow mixing layer over a horizontal bottom and the large coherent vortices in it as presented by *Van Prooijen & Uijttewaal (2002b).*

The modelling is divided in two stages. The first stage describes the evolution of the mean base flow, which is modelled using a quasi 1D model based on self-similarity. This model simulates some characteristic properties of the development of shallow mixing layers. These properties are a downstream decrease of the velocity difference across the mixing layer, a downstream reduction of the growth of the mixing layer width and a transverse displacement of the mixing layer centre towards the slow stream in downstream direction.

The second part gives a linear stability analysis which uses the modelled base flow to predict the development of the large coherent vortices.

The study shows that in shallow-water mixing layers the transverse velocity component is much smaller than the streamwise velocity component. This implies that the transverse free surface slope can be neglected in comparison with the longitudinal free surface slope.

A set of two coupled 1D models can be used to describe the interaction of the contiguous flows over a horizontal bottom if the following three assumptions are taken into account: The transverse mean velocities in both contiguous flows, the transverse variation of the water depth and the transverse variations of the bed friction coefficient are neglected.

These models for both flows are:

$$
\begin{aligned}
M_1 : U_1 + \frac{\partial U_1}{\partial x} + g\frac{\partial H}{\partial x} + c_f\frac{U_1^{\,2}}{H} = 0 \\
M_2 : U_2 + \frac{\partial U_2}{\partial x} + g\frac{\partial H}{\partial x} + c_f\frac{U_2^{\,2}}{H} = 0
\end{aligned}
\qquad (3.12)
$$

where M_i is the 1D equation of motion, U_i is the streamwise velocity component in the fast or slow stream, D the water depth, g the gravitational acceleration and c_f the bed friction coefficient.

Figure 3.3 shows a sketch of the mixing layer and the two streams discussed in this section.

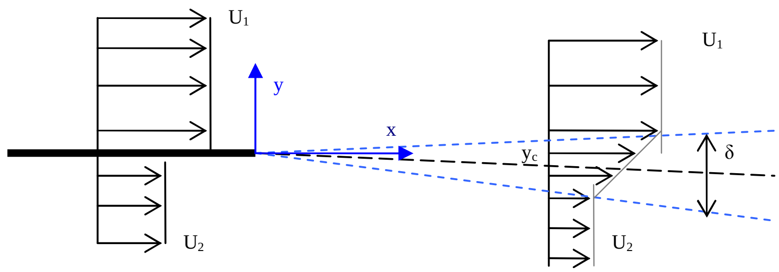

Figure 3.3 Mixing layer developed between two streams.

The subsequent expression is used to obtain the bed friction coefficient for a hydraulically smooth bottom, using the depth integrated Prandtl-Von Karman logarithmic profile:

$$\frac{1}{\sqrt{c_f}} = \frac{1}{k}(\ln(\mathrm{Re}(\sqrt{c_f}) + 1) \qquad (3.13)$$

where k is the Von Karman constant, 0.41; $\mathrm{Re} = \frac{U_c D}{\upsilon}$ is the local Reynolds number, with $U_c = \frac{U_1 + U_2}{2}$, υ is the kinematic viscosity and c_f is the bottom friction coefficient.

In shallow mixing layers the streamwise velocity component varies in the transverse direction. Previous experimental results have shown that for shallow mixing layers self-similarity of the transverse profile is found. Self-similarity implies that the transverse profiles of the streamwise velocity can be described with a self-similarity model. A profile function, of the form of a hyperbolic tangent, can be used to model the mean streamwise velocity field:

$$U(x,y) = U_c + \frac{\Delta U(x)}{2}\tanh\left(\frac{y - y_c(x)}{\frac{1}{2}\delta(x)}\right) \qquad (3.14)$$

where δ is defined as the mixing layer width and y_c is defined as the transverse position of the centre of the mixing layer. The 2D formulation of the streamwise velocity field is reduced to a formulation that depends only on the downstream position x. The mean flow field can be calculated by means of the evolution of δ and y_c in downstream direction.

3.3.3. Mixing Layer Width.

The downstream evolution of the shallow-water mixing layer can be described in terms of the evolution of the width of the shallow-water mixing layer.

The most practical and simple expression for the mixing layer width is the ratio of the velocity difference ΔU across the mixing layer to the maximum transverse gradient of the mean streamwise velocity:

$$\delta = \frac{\Delta U}{\left(\dfrac{\partial U}{\partial y}\right)_{\max}} \tag{3.15}$$

The presence of a single length scale is a characteristic of self-preserving mixing layers. The presence of two length scales, the water depth and the mixing layer width, suggests that shallow mixing layers cannot have the property of self-preservation. Despite the presence of two length scales, experiments have shown *(Uijttewaal and Booij, 2000),* that transverse distributions of the mean flow and turbulence characteristics can be scaled with only a single length scale (the width of the mixing layer).

This result can be ascribed to the presence and dominant role of the large coherent vortices in shallow mixing layers, which justifies the description of the evolution of the mixing layer by a single length scale.

These large coherent vortices generated by the transverse shear and with dimension of the order of the mixing layer width play an important role in the entrainment of mass and momentum and therefore in the growth of the mixing layer in downstream direction.

Consequently, the development of the mixing layer is affected by the presence of the large coherent vortices.

In an unbounded self-preserving mixing layer, the growth of the mixing layer is proportional to the relative velocity difference and a factor, which is called the entrainment coefficient (α):

$$\frac{d\delta}{dx} = \alpha \frac{\Delta U(x)}{U_c} \tag{3.16}$$

Equation (3.16) can be integrated with respect to the longitudinal coordinate, x, and substituting the development of the velocity difference:

$$\delta(x) = \alpha\lambda_0 \frac{H}{c_f}\left(1 - \exp\left(-\frac{2c_f}{H}x\right)\right) + \delta_0 \tag{3.17}$$

The centre of the mixing layer shifts towards the slow stream as a result of the deceleration of the fast stream, acceleration of the slow stream and continuity.

Figure 3.4 represents the mixing layer width according to equation (3.17) for an example of two streams with velocities U_1=0.30m/s, U_2=0.10m/s and a water depth of 0.1 m. The initial width δ_o is imposed by the thickness of the boundary layers and can be approximated to the water depth. The entrainment coefficient has an empirically determined value of α≈0.085.

The value of λ_o is given by $\lambda_0 = \dfrac{\Delta U_o}{2U_c}$, where ΔU_o is the velocity difference between streams and U_c is the velocity at the mixing layer centre.

The flow outside the mixing layer defines the mean difference over the mixing layer, $\Delta U_o = U_1 - U_2$ and the mean velocity in the centre of the mixing layer, $U_c = \dfrac{U_1 + U_2}{2}$.

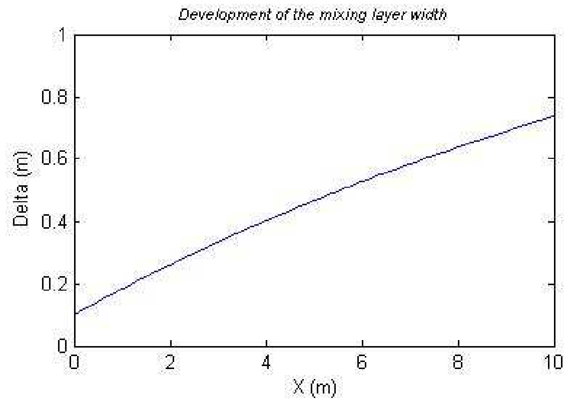

Figure 3.4. Width of a two-stream shallow mixing layer.

3.3.4. Coherent structures.

The development of the shallow mixing layer is predominantly determined by the velocity difference across the mixing layer and the growth of the large horizontal vortices, which are present in this type of flow.

These large horizontal vortices dominate the turbulent transports in the transverse direction.

It can be assumed that velocity fluctuations in different directions are related and this assumption has resulted in the concept of spatially coherent, temporally evolving vortical motions and they are usually called *coherent structures.*

Coherent structures are organised motions that are characteristic for turbulent flow. The correlation between the different components of the velocity in a coherent structure is what distinguishes them from the surrounding flow.

Large coherent vortices generated by the transverse shear and with dimension of the order of the mixing layer width play an important role in the growth of the mixing layer in downstream direction due to the entrainment of mass and momentum.

To study these coherent vortices, their turbulence properties have to be taken into account. Vortices are turbulent structures with a variety of scales and are generally characterised by randomness and 3D fluctuations, which can be characterised in a statistical sense.

Small-scale vortices, which characterise the fine structure of the turbulence, are nearly isotropic and behave to a certain extent as random motions.

In contrast to small-scale vortices, large-scale vortices show coherent behaviour because they retain their character while being advected over a large distance. These vortices extract energy from the mean flow by means of instability processes. These vortices appear to have a life cycle that includes different steps: origin, development, interactions with other structures and breakdown.

Therefore, coherent structures show dynamic motions with a life cycle. These motions appear to be quasi-periodic and give rise to quasi-periodic oscillations of an instantaneous velocity signal.

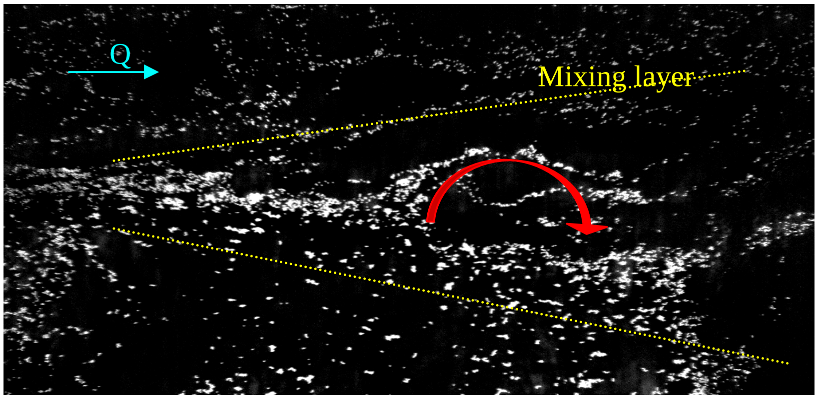

Figure 3.5. Coherent vortices in a mixing layer experiment.

A velocity signal can be interpreted as a superposition of fluctuations caused by small-scale turbulence with time scales t and fluctuations caused by large coherent vortices with time scales T (see *Figure 3.5*).

Nevertheless, large coherent vortices are not perfectly deterministic. On one hand, their characteristics (size, intensity and orientation) vary from one vortex to another. On the other hand, coherent vortices appear to move randomly in space and time in turbulent shear flows.

These properties are the reason that conventional long-term averaging cannot satisfactorily reveal the existence of coherent vortices and may not adequately explain the contributions of the coherent vortices to the velocity fluctuations. Traditional stochastic methods, experimental techniques or theoretical analysis are not capable of completely revealing the characteristics of these coherent vortices.

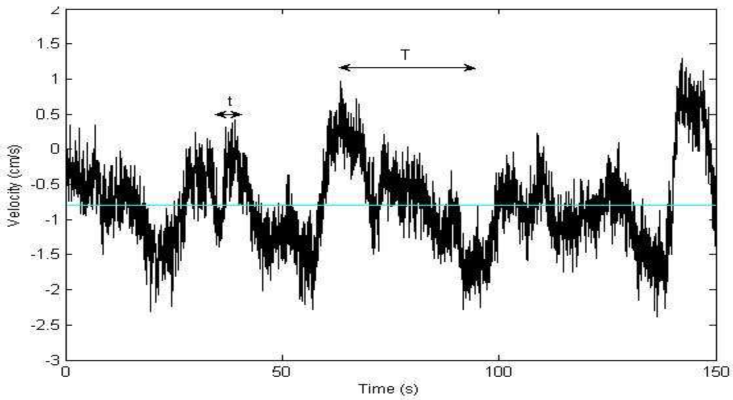

Figure 3.6. Time signal v-component from EMS measurements during the experiments.

3.4. Summary and conclusions.

In this chapter some basic concepts related with shallow waters flows and the processes that govern the flow patterns at the harbour entrance have been described.

The first section has given a brief introduction of turbulent flows, to continue with a description of the basic concepts and main equations that govern turbulence in the second section.

As it has been described in Section 3.2, the Reynolds equations can be closed by using the eddy viscosity concept. With the consideration of the Reynolds stresses the closure problem arises, which can be solved, in analogy with the viscous stresses in laminar flows by using the eddy viscosity concept.

The closure problem shifts to the determination of an effective eddy viscosity. The eddy viscosity is the product of a typical length and velocity scale. Different turbulence models can be used to determine these scales.

The third section has described the modelling of the development of two-stream shallow mixing layer over a horizontal bottom and the basic concepts of large coherent vortices.

The concepts described above will be the basis of the data analysis which will be developed in Chapter 5. The conclusions of this study will be drawn from this theoretical background.

CHAPTER 4.

LABORATORY EXPERIMENTS.

The experiments were carried out between November and December 2007 in the Laboratory for Fluid Mechanics of the Faculty of Civil Engineering and Geosciences of the Delft University of Technology.

This chapter deals with the description of the laboratory experiments which were executed in this study.

In Sections 4.1 and 4.2 the experimental set-up is described, including the flume, the flow conditions and the description of the model. In Section 4.3 the measurement techniques used during the experiments are presented. The main characteristics of the experiments will be discussed in Section 4.4.

4.1. Introduction.

The aim of the laboratory experiments presented in this thesis is to determine the effect of the geometry and the location of a system of piles, upstream the entrance of a harbour, on the exchange of mass between harbour and an adjacent river.

The influence of the characteristics of the system of piles on the velocity and density fields at the entrance of a harbour has been examined by using a physical model.

Two goals were established during the experiments:

- Qualitatively, to increase our insight into the effect of this structure on the exchange.
- Quantitatively, to generate a data set with which numerical models can be tested for the flow in harbour entrances.

4.2. Experimental set-up.

4.2.1. Geometry of the flume.

The experiments were carried out in a facility specially built for shallow-water flow research, the so-called shallow water flume, which is located at the Laboratory for Fluid Mechanics.

A top view and a side view of the flume are drawn in *Figure 4.1.*

The flume has a length of 20 m, a width of 3 m and a height of 0.20 m. The relatively large width of the flume ensures that the flow is shallow without sidewall effects.

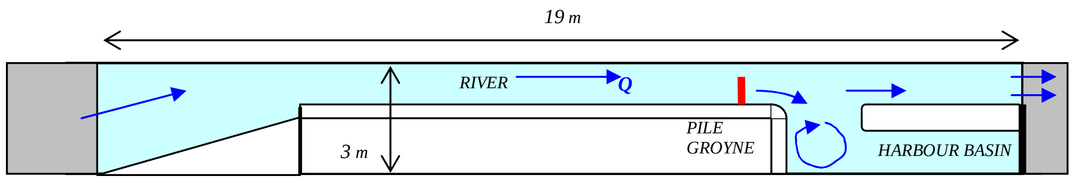

Top view

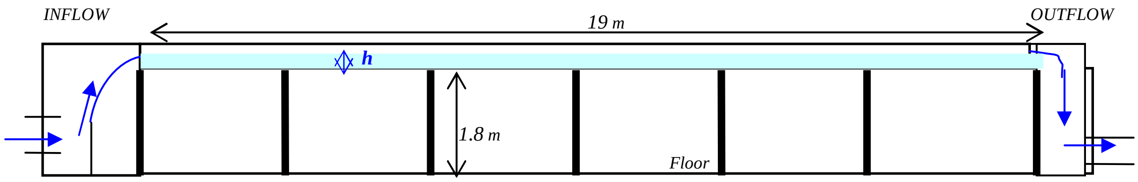

Side view

Figure 4.1 Shallow-water flume. Top and side view.

The facility has smooth glass sidewalls and a smooth horizontal glass bottom which is positioned 1.80m above the floor.

The facility is connected to the circulation system of the laboratory. The flow is generated by a constant water supply controlled by a main valve. The water height can be adapted by an adjustable sharp-crested weir located at the end of the flume. At this point, the water flows into a storage bin of the circulation system.

4.2.2. Flow conditions.

The facility was designed for experiments with a turbulent and sub-critical flow, as is the case in lowland rivers.

The flow has to satisfy two conditions. First, in order to establish a fully turbulent flow, the Reynolds number condition has to be accomplished. The Reynolds number should be sufficiently large to keep the flow turbulent, larger than about 2,300. Secondly, a subcritical flow is required in the facility. Moreover, in order to avoid influences of surface disturbances on the flow, the Froude number should be smaller than 0.5.

After several qualitative experiments, a flow of *40 l/s* was established to obtain a minimum Reynolds number of 4,000 into the harbour basin and a Froude number lower than 0.3 in the main stream.

It should be noted that even under these conditions the conclusions drawn from laboratory experiments cannot straightforwardly be applied to full scale natural river flows where Froude numbers are larger than 0.3, or river flows where Reynolds numbers are orders of magnitude larger.

4.2.3. Description of the model.

A top view of the model is given in *Figure 4.2.* The two main parts of the model are a harbour basin, where the entrance is 1.37 m wide, which is located perpendicularly to the direction of the flow along the river. The main stream is 1.2 m wide.

The perimeter of the harbour basin and the right bank of the river are made of concrete blocks. These blocks have a width of 30 cm and a height of 15 cm. The bottom part is made of multiplex and the upper part is a roughness layer of rocks.

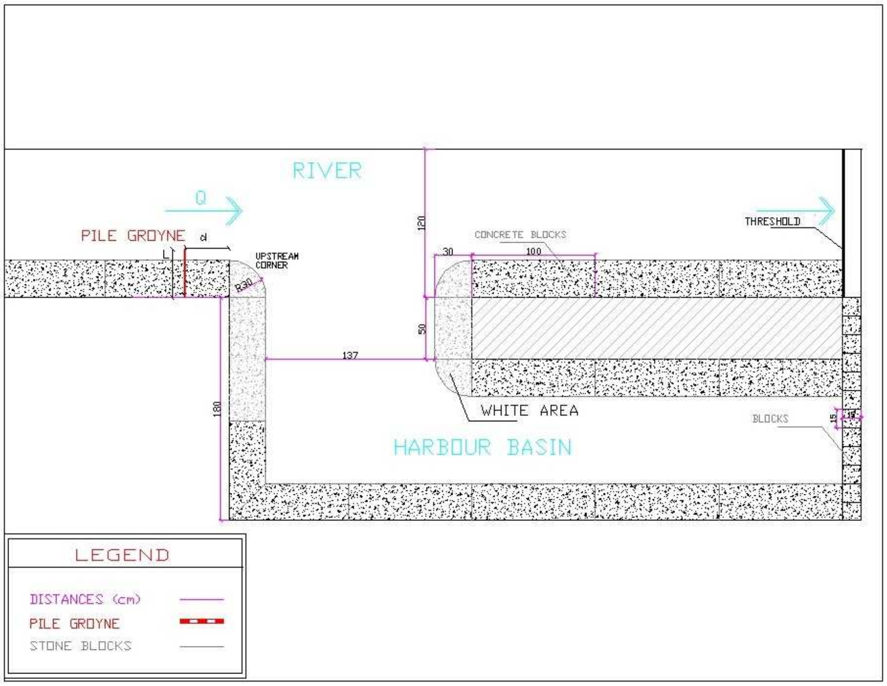

Figure 4.2 Top view of the model.

The groyne is located upstream the harbour entrance (see red line in Figure 4.2). The steel piles are located at the right bank. The total length (L) increases towards the main stream depending on the number of piles (n) and the space between them (s). The distance between the groyne and the edge of the upstream corner, delimited by the beginning of the first block, is labelled d.

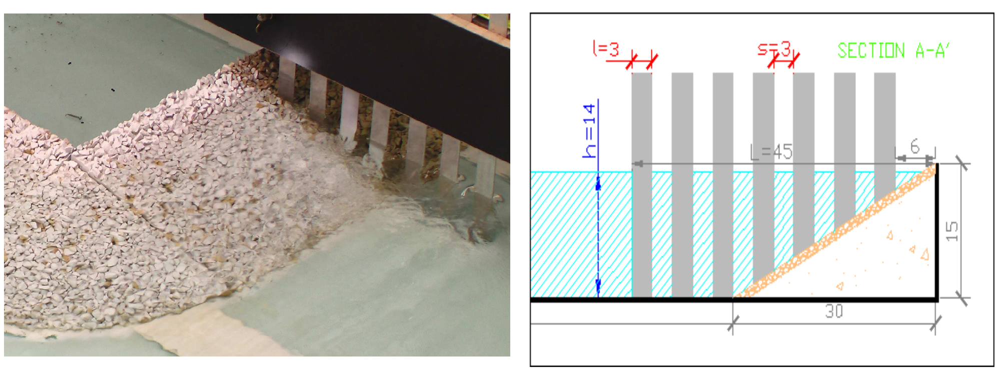

Figure 4.3 Details of embankment and the permeable pile groyne.

4.3. Measurement techniques.

Methods used to measure turbulence in water flows can be classified into two categories:

- Single point measurements.
- Flow visualisation techniques.

Single point measurement techniques are useful for the accurate determination of velocity fluctuations at one or more measurement points in order to acquire detailed temporal information about turbulence properties.

Flow visualising techniques are effective in revealing the presence, dimensions and structure of large 2D vortices.

During the experiments, both techniques were applied. Visualisations of large-scale quasi-2D vortices are carried out by means of Particle Tracking Velocimetry (PTV). Detailed information about turbulence properties is obtained with point measurements from an Acoustic Doppler Velocimeter (ADV) and an Electromagnetic Sensor (EMS). The main advantages of the ADV and EMS systems with respect to the PTV measurements are:

- A higher spectral resolution.
- The ability to measure over the water depth.

4.3.1. ADV and EMS techniques.

Acoustic Doppler Velocimeter (ADV) is point-velocity current meter with a high precision, because they measure velocities within a very small volume.

An ADV consists of a probe head connected by a stem to cylindrical electronics housing. The probe head consists of a transmitting transducer in the centre and two or three probes containing receiving transducers.

Velocities are measured within a sampling volume located at a fixed distance from the transmitting transducer, as illustrated in *Figure 4.4*.

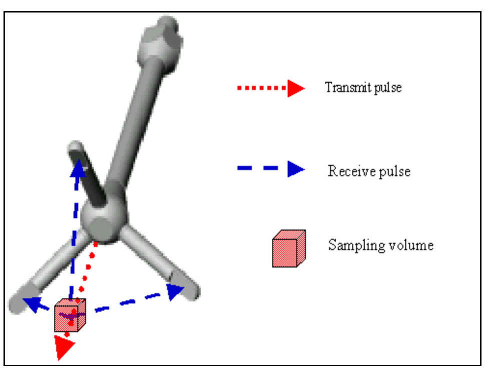

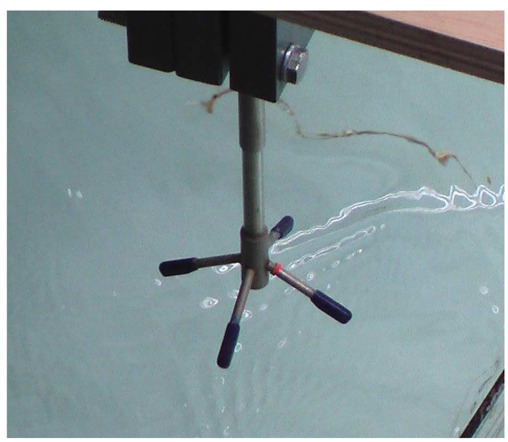

Figure 4.4 Detail of an ADV probe head.

The ADV requires the presence of small particles that scatter the acoustic waves. In this experiment these particles were hydrogen bubble of <100µm generated through electrolysis.

The EMS is generally applied for flow monitoring purposes in open channels and fully or partially filled pipes.

In many situations flow directions is subject to large variations and may even reverse. For this reason, the four quadrant response of the EMS enables direction-independent measurements.

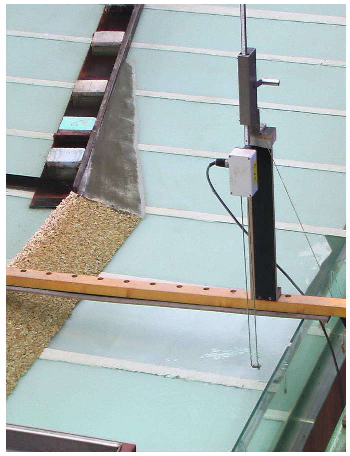

Figure 4.5. EMS located at the river stream upstream the harbour entrance.

4.3.2. Particle Tracking Velocimetry.

Particle Tracking Velocimetry (PTV) is a straightforward and powerful measurement technique. The principle is based on tracking individual particles in the flow. The velocity of a particle is determined by recording its displacement during a certain time interval.

In order to determine the velocity field, floating polypropylene beads with a diameter of 2mm were distributed homogeneously on the water surface.

A distributor was used to spread the beads homogeneously on the water surface, upstream the location of the pile groyne, so that the effect of particles moving out of vortex centres due to secondary circulation is reduced.

As the particles are submerged for more than 90%, they are expected to follow the surface velocity. A digital camera mounted on a bridge over the flume recorded the positions of the particles. The camera, a Kodak ES 1.0, has a resolution of 1008 x 1018 pixels with 256 grey levels and a maximum frame rate of 30 Hz.

The duration of the measurement should be chosen such that all important scales are captured. A time length of 5 minutes is enough to cover all large scale structures in the flow assuming that these are smaller than the length scale of the river width which is 1.2 m.

Sequences of 5 minutes, with a frequency rate of 10 Hz for each test, were recorded to obtain images to be analyzed during the data processing. Measurements are performed over a fixed area covering the harbour entrance. A maximum part of the mixing layer has to be captured: at least the first part needs to be covered.

This area has dimensions of 1.74m x 1.74m, which is considered to be sufficient to record the mixing layer. The centre of the measurement area is located at X=5.99m and Y=-0.15m (the description of the reference system is given in Section 5.1).

In order to present a good contrasting background for the particles white foil was attached to the glass bottom from below. The blocks and the joints between plates were painted. However, it was not possible to obtain a totally white surface for the PTV area. The characteristics of the PTV post-processing are described in more detail in Section 4.5.

4.4. Description of the experiments.

4.4.1. General considerations.

Six different series of experiments were performed.

- Series 1.Experiments with different location of the groyne upstream the entrance,
- Series 2. Experiments with a different number of piles,
- Series 3. Experiments with a different distance between piles,
- Series 4. Experiments with a withdrawal from the harbour, changing the location of the extraction point, and,
- Series 5. Experiment with a narrow harbour entrance, and,
- Series 6. Experiment with a different flow discharge.

The main characteristics of each series will be described in the following sections. The experiment in which the model is carried out without pile groyne located upstream the entrance has been labelled Test 2 or Reference case.

Table 4.1 illustrates the main characteristics of each experiment. Three parameters describe each case: first, **n** is the number of piles; second, **d** is the distance from the edge of the groyne to the edge of the corner, and **s** is the distance or gap between piles. These parameters were drawn in Figure 4.3.

The length of the groyne can be obtained from *n* and *s* as follows:

$$L = n \cdot l + (n-1) \cdot s \tag{4.1}$$

where *l* is the width of each pile (3 cm).

Series	*Test*	*Case*	*Piles (n)*	*Location "d" (cm)*	*Space "s" (cm)*	*L (cm)*
1	**2**	Reference case	-	-	-	
-	**3**	Groyne at d = 35 cm	7	35	3	39
-	**4**	Groyne at d = 0 cm	7	0	3	39
-	**5**	Groyne at d = 70 cm	7	70	3	39
2	**6**	6 piles	6	35	3	33
-	**7**	5 piles	5	35	3	27
3	**8**	s = 4.5 cm.	5	35	4.5	33
-	**9**	s = 2 cm	6	35	2	28
6	**10**	Different flow discharge	7	35	3	39
4	**11**	Ref. case + Withdrawal A	-	-	-	-
-	**12**	Pile groyne + Withdrawal A	7	35	3	39
-	**13**	Ref. case + Withdrawal B	-	-	-	-
-	**14**	Pile groyne + Withdrawal B	7	35	3	39
5	**15**	Narrow entrance	7	35	3	39

Table 4.1 Configuration properties of each experiment.

4.4.2. Parameters and points of measurement.

The table below shows which properties will be analysed from the different measurements with the discussed experimental setup.

The overview in this table merely presents the aim of what flow aspects were to be measured. The analysis and the results will show whether the techniques are in fact capable of measuring these flow properties.

PARAMETER		*EQUIPMENT*
Flow discharge.		Flow meter
Water heights.		EMS
Mean flow	Velocity profiles.	ADV, EMS, PTV
	Lateral displacement mixing layer	PTV, ADV
	Mixing layer width	PTV, ADV
Turbulent flow	Sizes coherent structures	PTV, ADV
	Time scales of coherent structures	PTV, ADV
	Reynolds stresses	ADV, EMS

Table 4.2 Parameters of measurement.

The flow discharge was 39.3 l/s and it was constant in all experiments.

Eight different EMS points were defined over the harbour basin and eleven ADV points were established at the harbour entrance. The PTV pictures are taken in an area of 1.74m x 1.74m. The PTV area includes some EMS and ADV points as it is shown in the sketch of Figure 4.6.

Figure 4.6 shows the measurement points for the ADV and EMS equipment at the harbour area.

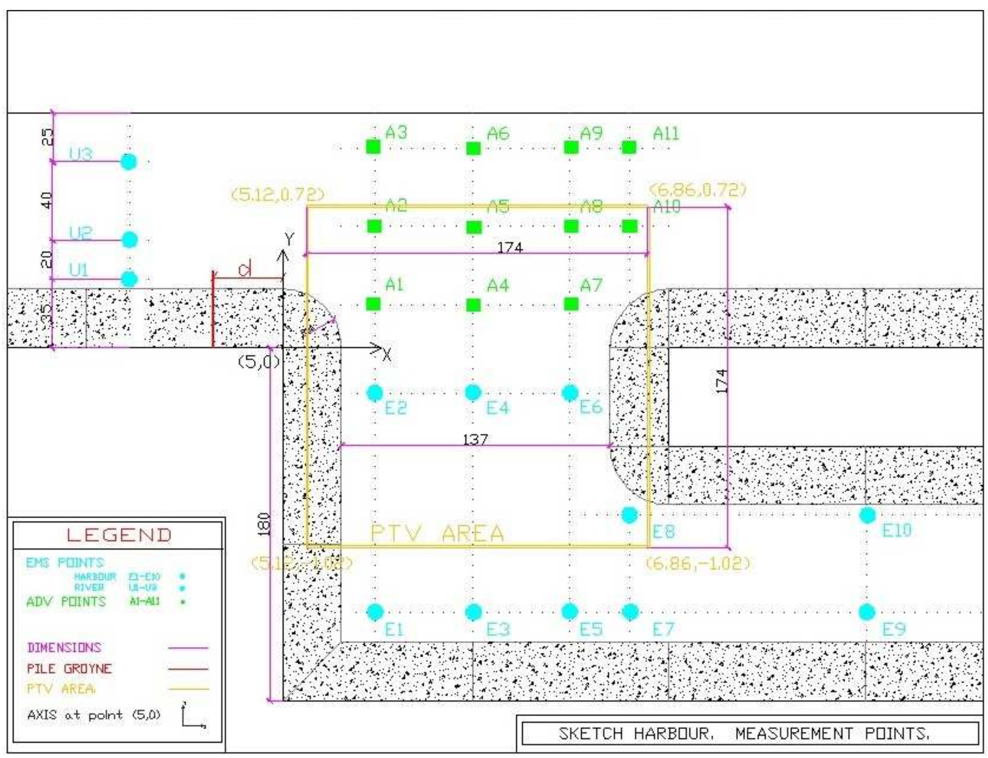

Figure 4.6 Measurement points and PTV area.

During the experiments for series 4, other points were located along the harbour basin in order to obtain more results due to the different behaviour of the gyres when a withdrawal is extracted from the harbour.

A different line of three EMS measurement points was defined upstream the groyne to study the effect of the system at the main stream.

4.4.3. Series 1. Experiments with different location upstream the entrance.

This set of experiments consists of a group of four tests. During these experiments, three different locations for the pile groyne were considered. The first experiment represents the reference case of this series, a configuration without pile groyne located upstream the model.

The distance from the groyne to the upstream corner of the harbour, *d*, is the variable parameter in each test. According to this distance, *d,* from the pile groyne to the corner, there are four different experiments:

- Reference case. Case without groyne and it is labelled Test 2.
- Distance d = 0 cm. The groyne is located at the edge of the corner. This experiment is labelled Test 4.
- Distance d = 35 cm. The groyne is located 35 cm upstream the corner. Test 3.
- Distance d = 70 cm. The groyne is located 70 cm upstream the corner. Test 5.

The number of piles and the space between them were constant in each experiment (7 piles and a gap of 3 cm). *Figure 4.7* shows a sketch of the Series 1.

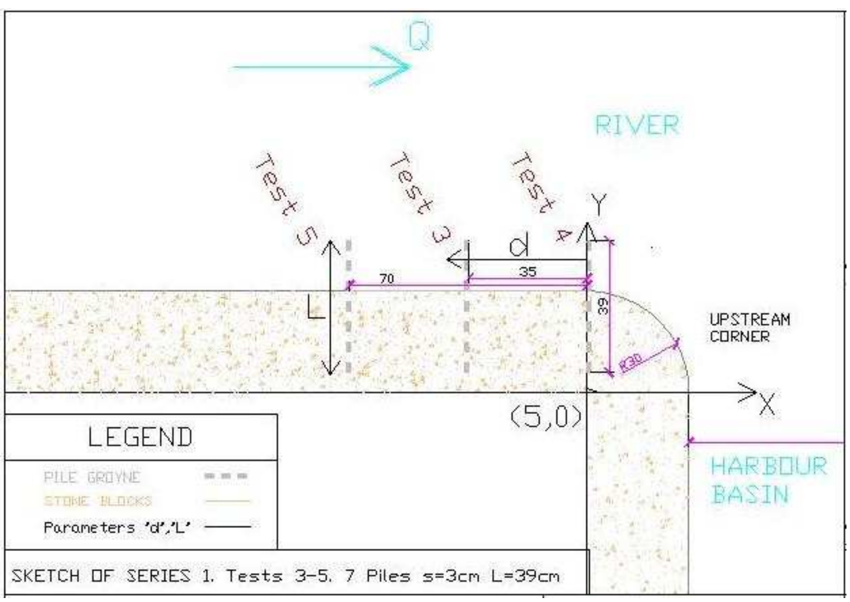

Figure 4.7 Sketch of series 1.

4.4.4. Series 2. Experiments with different number of piles.

Two different geometries of the pile groyne were performed during this second series. These tests were developed with the groyne located at a distance of 35 cm (as in Test 3) from the upstream corner of the harbour entrance.

Consequently, these experiments will be compared with Test 3, together with the reference case without groyne (Test 2).

The characteristics of each experiment are summarised as follows:

-Test 6. Groyne with 6 piles (n=6 piles and s =3 cm)

-Test 7. Groyne with 5 piles (n=5 piles and s =3 cm).

Figure 4.8 presents the sketch for experiments Test 6 and Test 7 from Series 2.

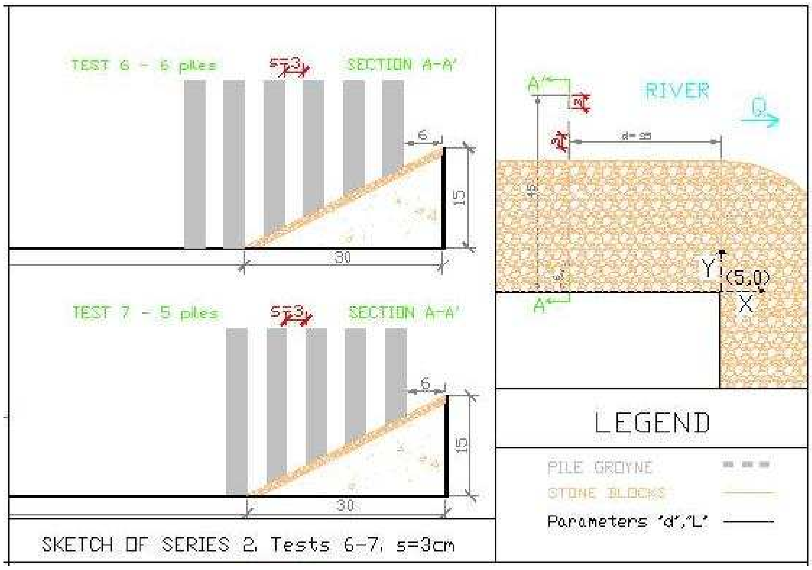

Figure 4.8 Sketch of series 2.

4.4.5. Series 3. Experiments with different distance between piles.

Two different geometries of the pile groyne were performed during this series. The groyne was located at a distance of 35 cm (as in Series 2) from the upstream corner of the harbour entrance. Therefore, these experiments will be compared with Tests 6 and 7.

The characteristics of each experiment are summarised as follows:

-Test 8. Groyne with a distance of 4.5 cm between piles, with a total number of 5 piles (n=5 piles and s =4.5 cm). This test will be compared with Test 7 (n=5 piles).

-Test 9. Groyne with a narrow distance of 2 cm between piles, with a total number of 6 piles (n=6 piles and s =2 cm). This test will be compared with Test 6 (n=6 piles).

Figure 4.9 shows the sketch of Tests 8 and 9.

4.4.6. Series 4. Experiments with withdrawal from the harbour.

The purpose of this set of experiments is to identify the effect of the pile groyne when a flow around 10% of the discharge is extracted from the harbour basin in order to study the model when the harbour basin contains a steady current.

These tests were performed with the same geometry as Tests 2 and 3, but with the exception that a withdrawal is taken from the harbour basin.

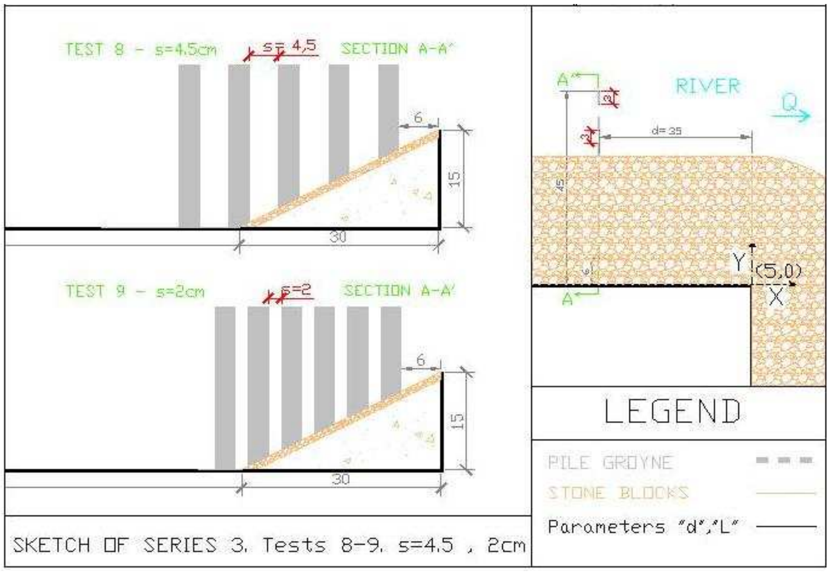

Figure 4.9 Sketch of series 3.

To accomplish this feature, one of the blocks of the basin was removed to allow the extraction of harbour water.

Four different cases were executed:

-Test 11. Reference case and withdrawal from the right part of the basin (the 7th block of the basin was removed).

-Test 12. Pile groyne located at 35 cm from the upstream corner and seven piles.

-Test 13. Reference case and withdrawal from the left part of the basin (the 3rd block was removed).

-Test 14. Pile groyne located at 35 cm from the upstream corner and seven piles.

Figure 4.10 shows a picture of the end of the harbour basin during Tests 11 and 12.

Figure 4.10 Picture of the extraction point for series 4.

4.4.7. Series 5. Experiment with a narrow harbour entrance.

For Test 15, the model was modified to obtain a narrow entrance in order to study the effect of the pile groyne when the geometry of the harbour entrance varies.

Two new concrete blocks were located at the model to reduce the harbour entrance from 1.37 m to 1.12 m. The new configuration is drawn in *Figure 4.11.*

In this case, the configuration of the pile groyne was the same than in Test 3, with d=35 cm and n=7 piles.

4.4.8. Series 6. Experiment with a different flow discharge.

During this experiment, a reduction of a 30 % in the flow discharge was set up to detect the variations on the velocity field for a case with a lower flow in the main stream.

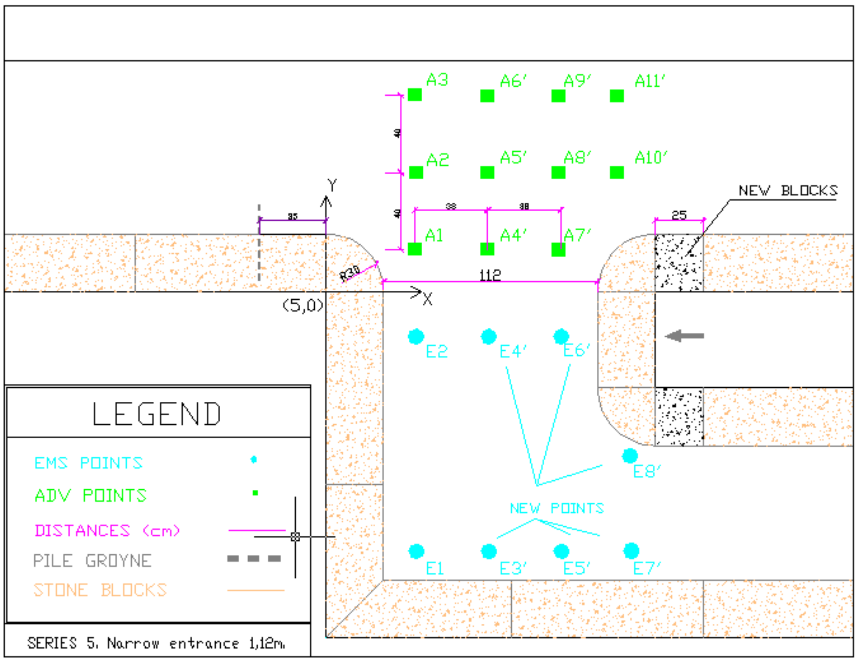

Figure 4.11 Sketch of series 5.

4.5. Data processing.

4.5.1. Reference system and cross sections.

The reference system is defined by (X,Y,Z) where X is positive in downstream direction and represents the streamwise coordinate, Y represents the transverse coordinate and it is positive from harbour to river, and Z represents the wall-normal coordinate and it is zero at the bottom. Consequently, the velocity vector is denoted (u; v; w).

The reference point for all locations is O (0, 0). This point is located 5m upstream the first corner of the harbour entrance. Consequently, the upstream corner is located at (5,0).

The different locations of the groyne for series 1 are defined by means of the parameter *d*. For example, the pile groyne at Test 3 is located 35 cm upstream the harbour entrance. Consequently, *d* = 0.35 m and Y = 5-d = 4.65 m.

All EMS and ADV measurement points are included in a corresponding cross section and longitudinal section. For instance, as it is labelled in *Figure 4.12*, point A4 corresponds with cross section "B" and longitudinal section "G". The PTV area includes five of these sections (A, B, C, F and G).

In this chapter, different cross and longitudinal sections will be taken into account to establish the comparison between PTV and ADV/EMS measurements.

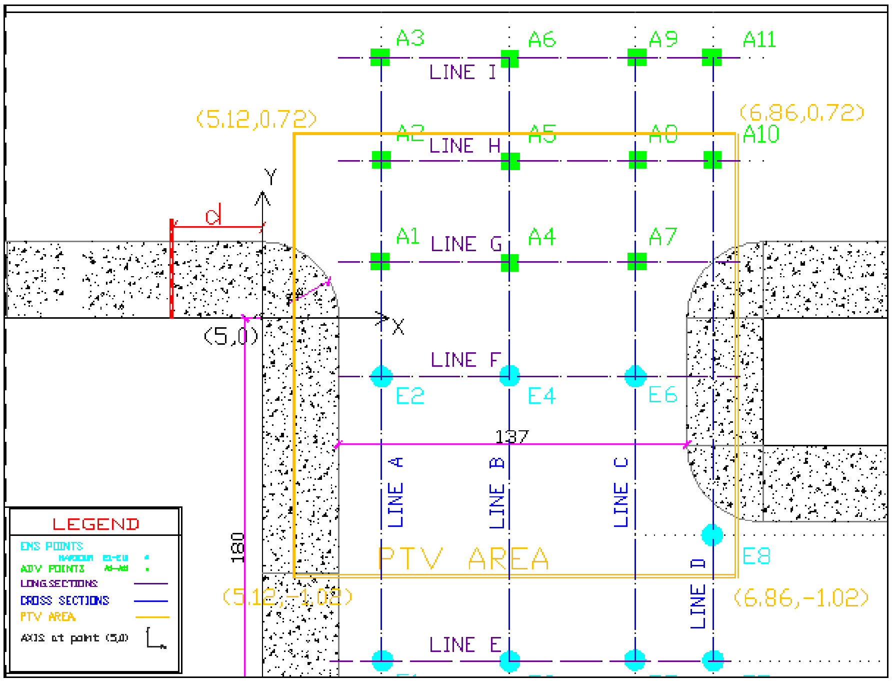

Figure 4.12 Cross and longitudinal sections of measurement points.

Table 4.3 gives the coordinates of the longitudinal and cross sections within the PTV area which will be used during the data analysis. Other sections will be used to describe results from ADV or EMS data.

SECTION	TYPE	COORDINATES (m)	DESCRIPTION
"A"	Cross-section	X_A= 5.47	Near the upstream corner. Corresponds with points A2, A1 and E2.
"B"	Cross-section	X_B= 5.98	Intermediate distance. Points A5, A4 and E4.
"C"	Cross-section	X_C= 6.47	Downstream corner. Points A8, A7 and E6.
"G"	Longitudinal Section.	Y_G= 0.22	Mixing layer. Line of ADV measurements. Points A1, A4 and A7.
"F"	Longitudinal Section.	Y_F= -0.23	Line of EMS measurements. Points E2, E4 and E6.

Table 4.3 Coordinates of the cross sections used during PTV comparison.

Appendix A includes the coordinates of the different points defined for the harbour model. They are related with measurement points from the EMS and ADV equipment.

4.5.2. Description of data processing.

This section deals with the procedure for data processing. The data analysis is split into two parts for each series. One part deals with the velocimetry: finding averaged velocity maps and the characteristics of the mixing layer. Another part focuses on the study of turbulence properties by means of autocorrelation analysis and Reynolds stresses.

In order to carry out these two parts of the analysis, data from ADV, EMS and PTV measurements has to be processed.

a) ADV and EMS data

Time signals, mean values and standard deviations are obtained from ADV and EMS measurements to provide information of the velocity field. These measurements will be used to establish the parts of the analysis which cannot be performed by PTV data, due to the limitation of the PTV area or the inaccuracy of this method to extract results related with turbulence properties.

b) PTV data processing

The PTV scheme developed by *Kadota* at the TU Delft has been used for the data processing. Kadota made three Matlab scripts to implement the data processing. These scripts are used by some researchers in Hydraulic Laboratory of TU Delft.

These Matlab scripts combined with the Matlab Image toolbox were employed to process the data.

The PTV algorithm tracks individual particles in successive images. A velocity vector at each particle position is determined on the basis of finding the most likely relations between the particle images of successive frames.

The paths of thousands of particles can be determined simultaneously, such that spatial information about the flow can be obtained with a high resolution.

This technique tracks the paths of individual particles and calculates the velocity, resulting in an unstructured velocity vector map. This map is interpolated to a regular grid of 41x41 mesh points using linear interpolation. Interpolation of the velocity vectors yields a sequence of velocity vectors mapped on a structured grid.

In this study, an amount of 1,000 – 2,000 particles are detected at each time step.

Velocity fields from time series have been averaged in order to get a proper view of the properties of the primary gyre present in the harbour entrance and the behaviour of the mixing layer at the harbour-river-interface.

Using this procedure, only information regarding the motion of the free surface is obtained. Mean and standard deviation values will be used to describe the mean flow pattern.

The most important modules of the PTV algorithm are:

- Background filtering.

Each experiment has 3,000 frames from the camera recording. The frame rate of recording was ten frames per second.

The resulting single images serve as input for the first Matlab programme that detects the particles on each frame. The first step consists of converting each frame to a black and white image.

- Particle image localisation.

The detection of the particles is based on the idea that the particles are shown in the image and they are significantly darker than the surrounding pixels.

This binarisation of the image should be done with such a level that a maximum number of particles is captured in the image.

A complicating factor in this was that in all experiments the bottom of the model was not completely white. By means of trial and error, an appropriate average threshold level was chosen to make sure a maximum number of particles were detected.

- Matching and prediction.

The estimated position of a particle is established from frame to frame. Store all possible pairings within the defined maximum matching distance are stored and the position of a particle in a next frame is estimated. By means of spatial interpolation with a weighting function based on the displacement of neighbouring matched particles.

- Mapping.

Determining the mean flow field consists in principle of two steps. First a spatial grid has to be constructed in the rectified image. For every instantaneous velocity map, a spatial interpolation of vectors has to be performed. The result is a set of velocity maps for all time steps in which all vectors are placed on the nodes of the grid.

The second step is to make a time average of all these interpolated instantaneous velocity maps to get one time-averaged velocity map. This is done by calculating the average flow vector for every grid point of all vectors that appear on that grid point in the instantaneous velocity maps.

- Post-processing.

Several Matlab programs, or scripts, were made that enable the data analysis and all necessary processing steps.

The following figures represent some of the steps carried out by the PTV algorithm to extract velocity vector fields from the original pictures which were taken during the experiments.

Figure 4.13.a. shows a frame of Test 2 (Reference Case) and its transformation after the background filtering. During the mapping process, the particles are detected in consecutive frame to determine the velocity vectors which are plotted in figures 4.13.c and 4.13.d.

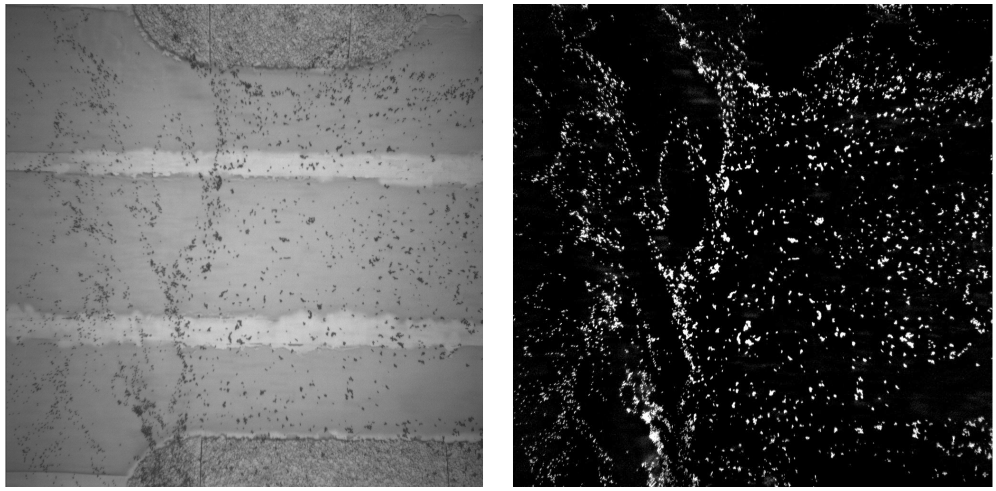

a) Original picture and particles. *b) Background filtered.*

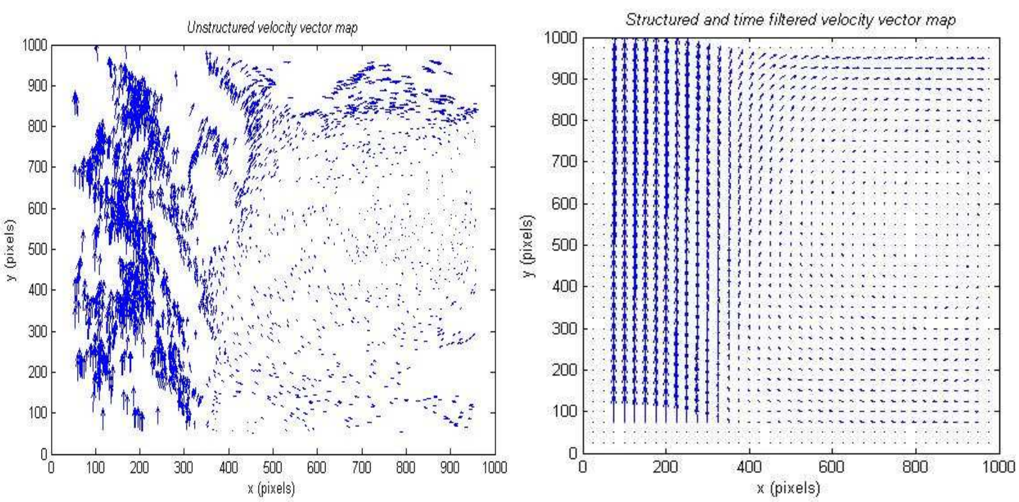

c) Unstructured velocity vector field. *d) Structured velocity vector field.*

Figure 4.13.a.PTV processing.

c) Autocorrelation analysis.

The current paragraph describes the theory and plot representation of the autocorrelation analysis which will be carried out in the following sections of this chapter.

The basic equation for autocorrelation function in terms of discrete time reads:

$$R_m = \frac{1}{N\text{-}m}\sum_{t=1}^{N\text{-}m}(x_t)(x_{t+m}) \approx \frac{1}{N}\sum_{t=1}^{N\text{-}m}(x_t)(x_{t+m}) \qquad (4.2)$$

where R_m represents the value of the autocorrelation function at the time delay τ, x_t represents the value of the signal x at time t, and $x_{t+\tau}$ is the value of the signal x at delayed time t+ m, N (sample size) is the approximation of N-m (the difference between N-m and N is negligible in most cases), and m is the delay value called lag.

Introducing x (mean of the entire time series x) into Eq 4.1-, the expression for the Autocovariance is obtained:

$$\text{Autocovariance}=\frac{1}{\text{N}}\sum_{\text{t=1}}^{\text{N-m}}(x_t-\bar{x})(x_{t+m}-\bar{x}) \tag{4.3}$$

Autocovariance is one of the two major components in the formulation of the autocorrelation coefficient function for a given lag value.

For an autocovariance analysis, a time series gets compared to itself and the main tool in the system is the lag. It is a quick method of evaluating deviations between the one unaltered time series and one that is lagged.

In order to generate the autocovariance values there are two rules. The first rule is that the data set should contain more than 50 data points. The second rule is that the largest lag for the autocovariance calculation must be equal to one quarter of the total number of points in the data set.

In this thesis, an autocorrelation analysis is studied from ADV and EMS data. In both cases, the previous rules are fulfilled. Data set contains more than 50 data points (1000 and 12000 points, respectively) and the largest lag is exactly one quarter of the number of data points for EMS results and it is lower for ADV.

The second factor for the autocorrelation coefficient for a given lag is called variance and it is obtained by standardising Eq.4.3. Therefore, it can be compared directly to other standardised autocovariances. The equation for variance is the sum of the square terms of (x_t-x) for each observation in the original time series, divided by N:

$$\text{Variance}=\frac{1}{\text{N}}\sum_{\text{t=1}}^{\text{N-m}}(x_t-\bar{x})^2 \tag{4.4}$$

Following the previous concepts, the description for the autocorrelation coefficient for a given lag is basically the autocovariance divided by the variance as presented in:

$$\text{Autocorrelation } (\text{R}_\text{m})=\frac{\text{autovariance}}{\text{variance}}=\frac{\sum_{\text{t=1}}^{\text{N-m}}(x_t-\bar{x})(x_{t+m}-\bar{x})}{\sum_{\text{t=1}}^{\text{N-m}}(x_t-\bar{x})^2} \tag{4.5}$$

The autocorrelation coefficient values range between +1 to –1, with +1 meaning the time series compared are exact duplicates of each other, which also means the lag value is equal to zero, and –1 meaning the time series compared are mirror images of each other.

Time series which have no relation to each other gives a null coefficient, therefore likely to be random.

In order to analyse the autocorrelation coefficients and their respective lag values it is possible to plot the autocorrelation coefficient against the lags. The plot is called correlogram or autocorrelation function.

With this method, it is viable to identify the relationship between different time series of data.

In the case where two time series are compared, if they do not have relationship to each other, the autocorrelation function will show an irregular pattern with amplitude close to zero, except when the lag value is equal to zero. In contrast, when the time series have a strong relationship, the function will present high coefficient values and a regular pattern.

Visual examination of different autocorrelation functions will be applied for different EMS and ADV locations for each series.

However, this method is very subjective to individual interpretation. A person with many years of experience will be able to make a more precise comparison than a person who has less knowledge on this field of expertise.

d) Reynolds stress components

As it has been explained in Chapter 3, a velocity field (u, v, w) can be decomposed into mean and fluctuating components: $u=\bar{u}+u'$; $v=\bar{v}+v'$; $w=\bar{w}+w'$.

The averaged velocities have been subtracted from the instantaneous velocities to give the fluctuating components of velocity: u', v' and w'. Then, the Reynolds stress can be defined as

$$-\rho\langle u'w'\rangle$$

The magnitude of the Reynolds stress more often approaches zero. The Reynolds stress term $u'v'$ represents the effect of the fluctuating horizontal velocity components on the mean motion.

It also shows the turbulence of the mean flow movement (multiplied by density, $u'v'$ is the momentum exchange). The Reynolds stress is in fact the covariance between the two horizontal velocities. This is defined in such a way that $u'v'$ is likely to be negative where $\partial u/\partial y$ is positive and vice versa.

It is expected that the component $\langle u'w'\rangle$ will approach zero for points located at the mixing layer and $\langle u'v'\rangle$ will approach zero in points of the river stream.

The average value of each component should be of the order of 0.4 times the product of u_{sd} and v_{sd} at the points of measurement near the mixing layer.

The Reynolds stresses can be considered as an identifier of a different downstream evolution of the large horizontal vortices for different upstream conditions, as the different configurations of the groyne.

CHAPTER 5.

EXPERIMENTAL RESULTS. DATA ANALYSIS.

In this chapter it is considered whether a difference in geometry and configuration of the pile groyne imposed upstream a harbour entrance results in different mixing layer dynamics.

Several experiments were executed that differs in location of the array, number of piles and other aspects like the gap between piles and the presence of a withdrawal from the harbour basin.

Three series of experiments will be discussed:

-Section 5.1 develops the analysis of Series 1, with different locations of the groyne upstream the entrance.

-Section 5.2 will describe Series 2, which consists of two experiments with different number of piles.

-Section 5.3 presents the data analysis of Series 3, with two experiments with different distance (gap) between piles.

Each section will be divided in two parts. The first part discusses the properties of the mean flow. These properties are the velocity differences along the mixing layer, across the harbour entrance and the variations in the mixing layer width and its centre.

The second part considers turbulence properties of the flow. An autocorrelation analysis is carried out from EMS and ADV results and some aspects will be considered in relation with Reynolds stresses.

5.1. Data analysis for Series 1.

In this section emphasis is put on differences, between the four experiments of Series 1, in relation with downstream development of the flow properties obtained from PTV measurements and ADV-EMS measurements.

5.1.1. Mean flow.

5.1.1.1. Velocity field.

The velocity field will be characterised by two components: u, is the streamwise velocity component and it is defined positive from upstream to downstream along the river; *v*, is the transverse velocity component and it is defined positive from harbour to river (as it was considered for *x* and *y* coordinates in Chapter 4).

In order to obtain an overall view of the flow pattern at the harbour entrance, a modified vector map of the mean velocity is plotted for each case in *Figure 5.1.1.*

It shows the velocity vectors which represent the flow pattern along the harbour entrance, obtained from PTV results for each experiment of Series 1.

These vectors are plotted along cross sections "A" (X=5.47m), "B" (X=5.98m). and "C" (X=6.47m). Different points along the harbour entrance at Y=0m are drawn (green vectors). Each velocity vector results from the combination of the average values of the streamwise and the transverse component. Each vector is obtained from $(u^2+v^2)^{1/2}$.

A simplified sketch of the harbour model is drawn to give an view of the location of the groyne in each case (thick red line)

At Y=0.22m, these figures show a decrease of the velocity in all cases with the groyne located upstream the entrance. Larger water velocities are observed in these points for Test 5 (groyne at d=70 cm).

It is found that velocities near the entrance show different magnitude in each case. In Test 4 (groyne at d=0 cm), as in Test 5 (groyne at 70 cm), the mean transverse velocity component is larger than in the reference case near the upstream corner of the entrance. However, Test 3 (groyne at d=35 cm) presents much larger mean transverse velocities along this line near the downstream side of the harbour basin.

A velocimetry comparison between ADV and PTV data will be discussed in the next paragraph and after that, mean values of the streamwise and transverse velocity components will be analysed by means of lateral profiles and other diagrams in following subsections.

5.1.1.2. Velocimetry comparison ADV versus PTV.

Before ADV and PTV results can be discussed, it is necessary to compare the ADV average velocities with the averaged values from PTV measurements.

For all cases of Series 1, a direct comparison is made between the average velocities of the ADV and the gridded average velocities of the PTV.

Measurement points from longitudinal sections "G"(Y=0.22m) and "H" (Y=0.62m) can be compared with the PTV data. The results are listed in *Table 5.1.1.*

Note that even though some ADV points are within the area captured by the PTV camera, it can be possible that there is no sufficient amount of particle data at those points to calculate an average PTV velocity. As well, ADV points at Y=0.62m are not within the area, then they will be compared with PTV results at the last coordinate with data (Y=0.57m).

For the reference case, at points along section "H" (Y=0.62m) the difference between ADV and PTV results is close to 10%-15%(i.e. point A2 varies from 31.47 to 36.20 cm/s), on average the relative differences along section "G" (Y=0.22m) are larger. The highest deviation is found at point A1, the first measurement point near the upstream corner. It is clear that the deviations are greater for locations towards the harbour entrance line and the upstream side.

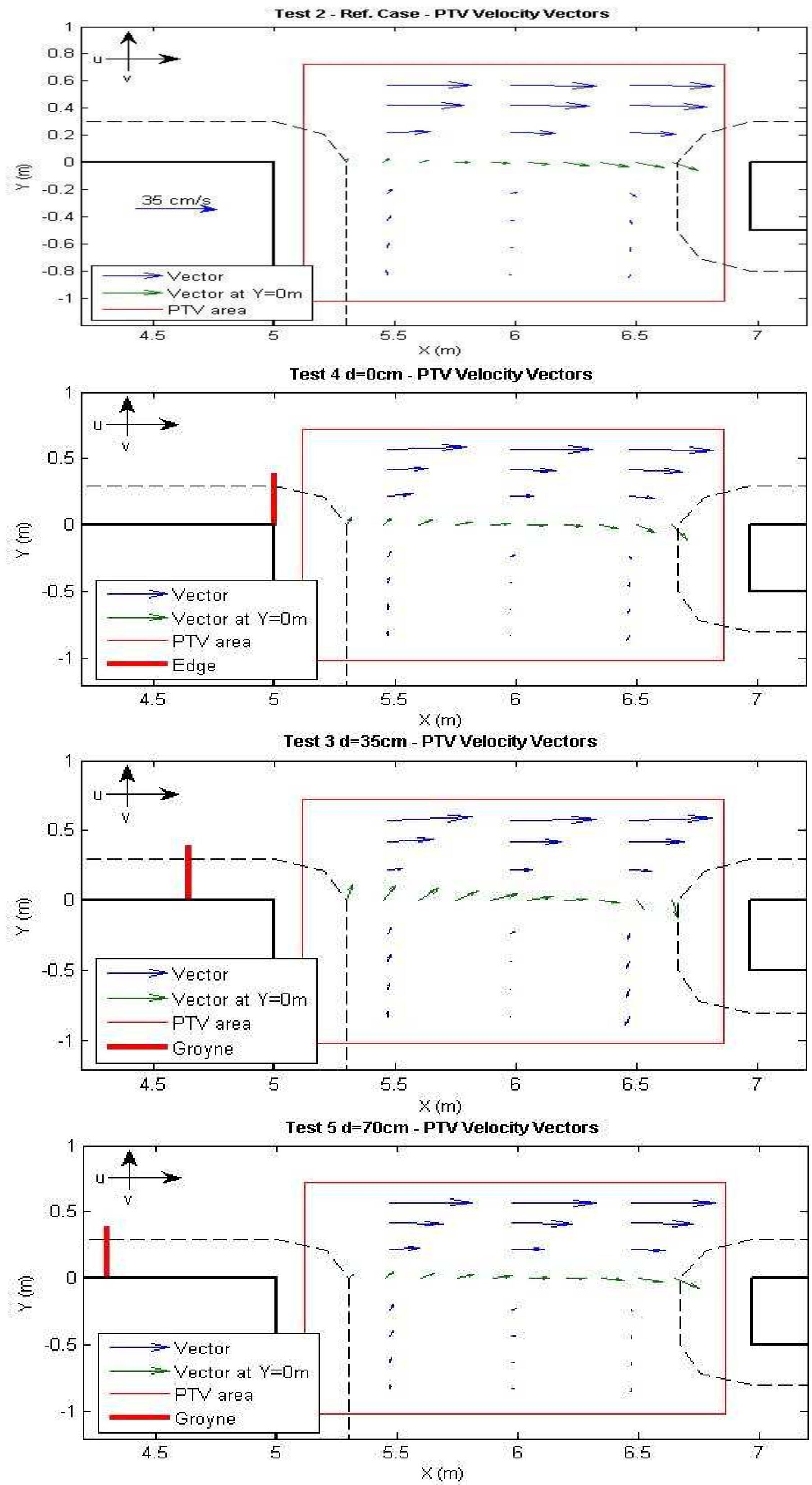

Figure 5.1.1. Series 1.Velocity vectors from PTV data.

For all cases with the groyne located at the model a different relation is found. All points along section "H" (Y=0.62m) show higher streamwise velocities from ADV results. Consequently, PTV values along the stream are lower than ADV values with regard to the streamwise component.

All cases show a positive absolute difference (Δ) along section "G" (Y=0.22m), due to the presence of higher transverse velocity components from PTV data. It is important to mention that Test 3 shows low Δ values along the coordinate Y=0.22 m.

It is not strange that there are such clear differences between the two velocimetry methods, since deviations in both lateral and downstream direction are to be expected as a result of the particle paths.

A large difference between both techniques is an indicator of 3D effects like upwellings or secondary circulation along the interface river-harbour.

In conclusion, the difficulty in this comparison is that different techniques detect different parts of the flow. It is generally not easy to compare data from two different experimental methods. PTV requires a more even spreading to obtain a higher accuracy.

Test 2 – Ref. Case.

POINT	Coordinates		ADV	PTV	
	X(m)	Y(m)	$\sqrt{(u^2+v^2)}$(cm/s)		Δ (cm/s)
A1	5.47	0.22	5.33	18.28	12.95
A2	5.47	0.62	31.47	36.20	4.73
A4	5.98	0.22	10.01	18.98	8.96
A5	5.98	0.62	31.06	36.60	5.54
A7	6.47	0.22	11.96	20.24	8.28
A8	6.47	0.62	29.20	36.35	7.15

Test 4 – Groyne d=0 cm.

POINT	Coordinates		ADV	PTV	
	X(m)	Y(m)	$\sqrt{(u^2+v^2)}$(cm/s)		Δ (cm/s)
A1	5.47	0.22	4.06	9.46	5.39
A2	5.47	0.62	35.72	28.92	-6.81
A4	5.98	0.22	4.76	8.72	3.96
A5	5.98	0.62	35.27	30.37	-4.90
A7	6.47	0.22	5.13	9.52	4.40
A8	6.47	0.62	34.39	31.34	-3.05

Test 3 – Groyne d=35 cm.

POINT	Coordinates		ADV	PTV	
	X(m)	Y(m)	$\sqrt{(u^2+v^2)}$(cm/s)		Δ (cm/s)
A1	5.47	0.22	3.75	5.60	1.85
A2	5.47	0.62	35.48	29.41	-6.07
A4	5.98	0.22	6.85	7.56	0.71
A5	5.98	0.62	34.78	29.49	-5.30
A7	6.47	0.22	7.57	8.01	0.45
A8	6.47	0.62	34.18	28.89	-5.30

Test 5 – Groyne d=70 cm.

POINT	Coordinates		ADV	PTV	
	X(m)	Y(m)	$\sqrt{(u^2+v^2)}$(cm/s)		Δ (cm/s)
A1	5.47	0.22	2.92	11.18	8.27
A2	5.47	0.62	34.36	30.91	-3.45
A4	5.98	0.22	6.83	11.63	4.80
A5	5.98	0.62	33.43	31.10	-2.33
A7	6.47	0.22	7.80	12.72	4.92
A8	6.47	0.62	32.73	31.55	-1.17

Table 5.1.1. Series 1. Comparison of flow velocities from ADV and PTV.

5.1.1.3. Streamwise velocity.

- Lateral profiles. Sections "A"and "B".

In this paragraph, different lateral profiles along two cross sections "A" (X=5.47m) and "B"(X=5.98m) are considered. Section "A" corresponds with points E1, E2, A1, A2 and A3; and Section "B" corresponds with points E3, E4, A4, A5 and A6. These different measurement locations were drawn in section 4.5 (Data processing).

For each case, ADV values are plotted with a single mark and PTV results with a solid line. From *Figure 5.1.2*, it can be concluded that for Test 2 (Reference Case) there is a difference between ADV and PTV results around 6 cm/s along the river stream that it can be attributed to the velocity distribution over the depth. The ADV is located 5 cm above the bottom; hence, it is located 9 cm below the surface, and this distance can be considered the origin of this discrepancy.

These differences increase within the region of the mixing layer. At Y=0.22m, ADV values remain from 12.95 cm/s (A1) to 8.28 cm/s (A7), lower than the PTV results as it was described in table 5.1.1.

PTV results show a stable mean streamwise velocity along the mixing layer (from 18.28 cm/s to 20.18 cm/s), but these values vary notably for the ADV measurements, increasing from the upstream corner to the downstream sidewall of the harbour (from 5.32 cm/s to 11.86 cm/s).

A clear decrease on the streamwise velocity is seen from Figure 5.1.2 for all experiments with groyne. The lateral profile in these cases shows lower velocity gradients and the profile moves towards the river. A clear shift along the profile is seen in these experiments due to the presence of two mixing layers. Test 5 (groyne at d=70 cm) presents higher PTV values than for the rest of experiments.

The gradient of the streamwise velocity along the cross section is lower for theses cases, and Test 4 (groyne at d=0 cm) gives the lowest value.

As it was discussed in the previous section, all ADV measurements are higher than the PTV results at Y=0.57 m (last y-coordinate with data within the PTV area).

It means that the effect of the pile groyne suggests a decrease in surface velocities near the harbour entrance and at the river stream, but ADV reveals an increase of the mean streamwise velocity at the river stream at middle depth. These results can be attributed to the fact that the groyne reduces the cross section of the river stream, resulting in higher velocities at the middle depth, but exerting a lower effect on the surface motion.

Figure 5.1.3 presents the lateral profile in section "B" (X=5.98 m). From section "B", Test 4 (groyne at d=0 cm) and Test 3 (groyne at d=35 cm) present identity profiles, with lower values than Test 5 (groyne at d=70 cm) and a lower velocity gradient.

In this section, the shift along the profile due to the presence of two mixing layer has disappeared in all cases. It can be slightly appreciated in Test 4 (groyne at d=0 cm).

From these lateral profiles, it can be conclude that the closer the groyne is located to the entrance the more it has an effect on the reduction of the surface velocities along the entrance.

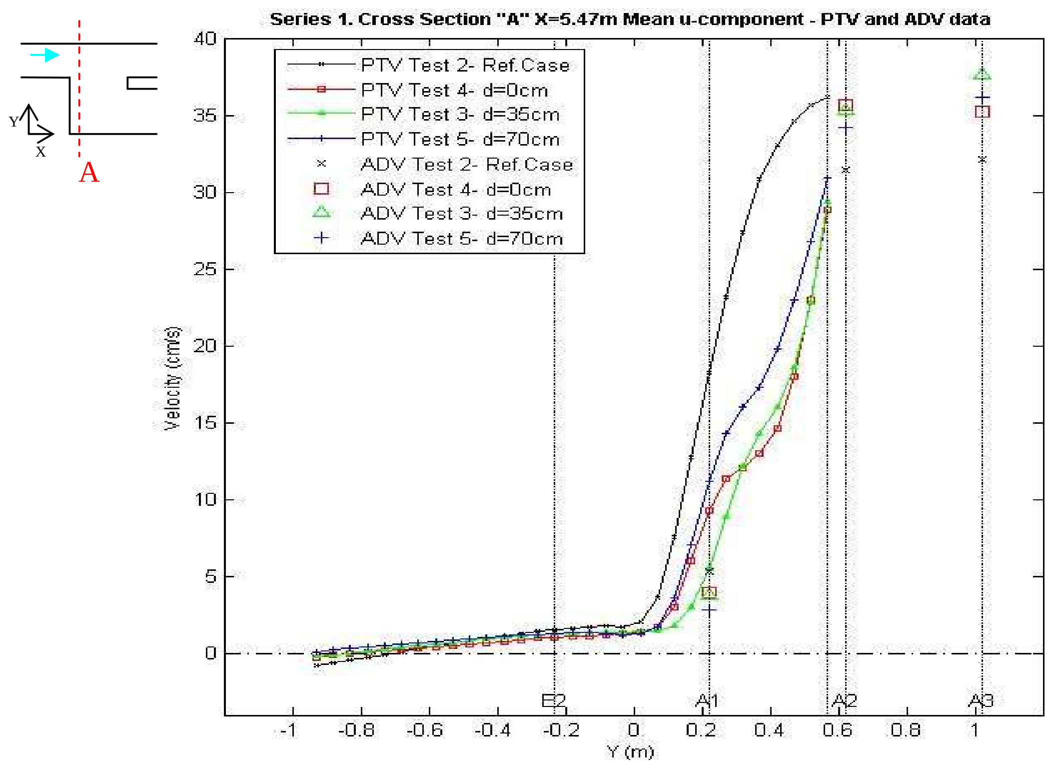

Figure 5.1.2 Series 1. Lateral profile mean u-component (cm/s). Section A. (X=5.47m).

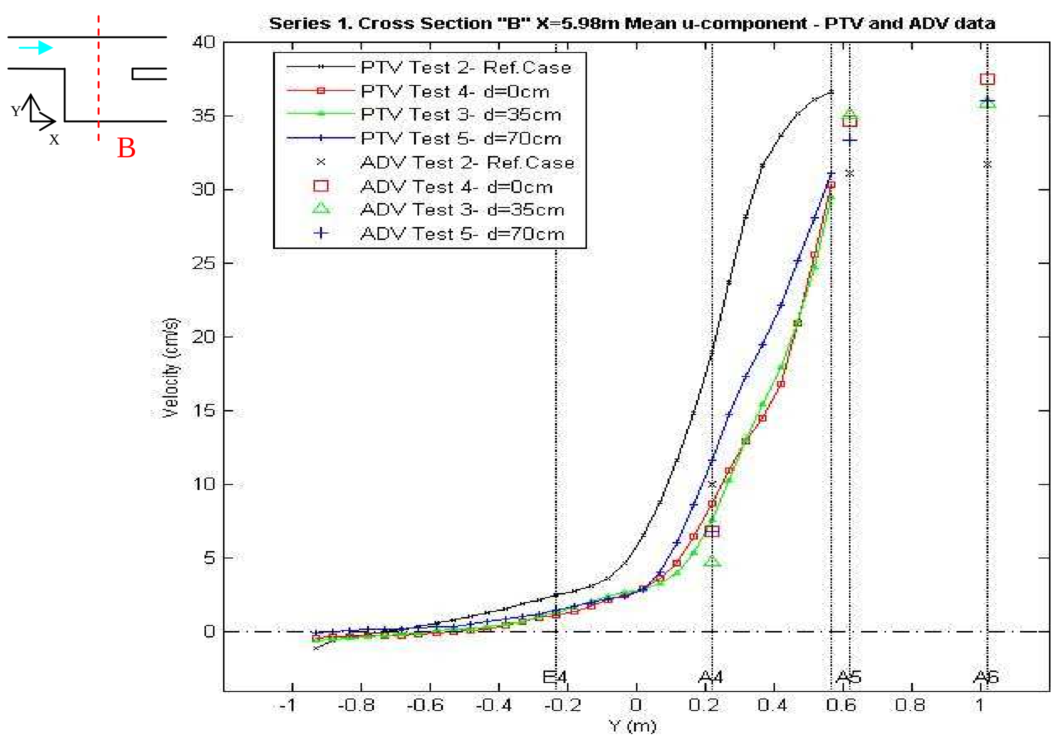

Figure 5.1.3. Series 1. Lateral profile mean u-component (cm/s). Section B. (X=5.98m).

- Standard deviation. Streamwise velocity.

Figure 5.1.4. shows the distribution of the standard deviation for the streamwise velocity from PTV results (this parameter will be denoted u_{std}).

The location of the groyne is sketched in each figure to provide an idea of the position of the array and the PTV area at the harbour entrance. From these figures the location of the highest values of the standard deviation for the u-component can be discussed.

It is feasible to associate the location of the mixing layer with the points where the standard deviation gives higher values. In accordance with this assumption, the reference case reveals a clear area from the upstream corner towards the downstream side where u_{std} presents values around 3-4 cm/s.

With regard to the other experiments, Test 4 (groyne at d=0 cm) shows high u_{std} values near the upstream corner, opposite to the location of the array, and the green area (points with u_{std} values from 3 to 4 cm/s) moves towards the river and it does not reach the downstream side of the harbour entrance. High u_{std} values around 5 cm/s are revealed near the edge of the groyne.

However, comparing Test 3 (groyne at d=35 cm with the previous results, the highest u_{std} values are located between the x-coordinates 5.5 m and 6.5 m at the river stream, and it shows values around 7-8 cm/s.

Nevertheless, for Test 5 (groyne at d=70 cm) the high standard deviation points are located at the river stream as in Test 4, but further from the harbour entrance, with lower u_{std} values and it shows a regular behaviour along all the area, except for a small area with high u_{std} values at the river stream.

From this stage, a clear change on the location of the mixing layer is recognized, which shifts towards the river stream due to the presence of the groyne.

High u_{std} values are shown near the upstream corner for the configuration with the closest groyne, but this turbulent pattern is diminished when the groyne is located 70 cm from the entrance.

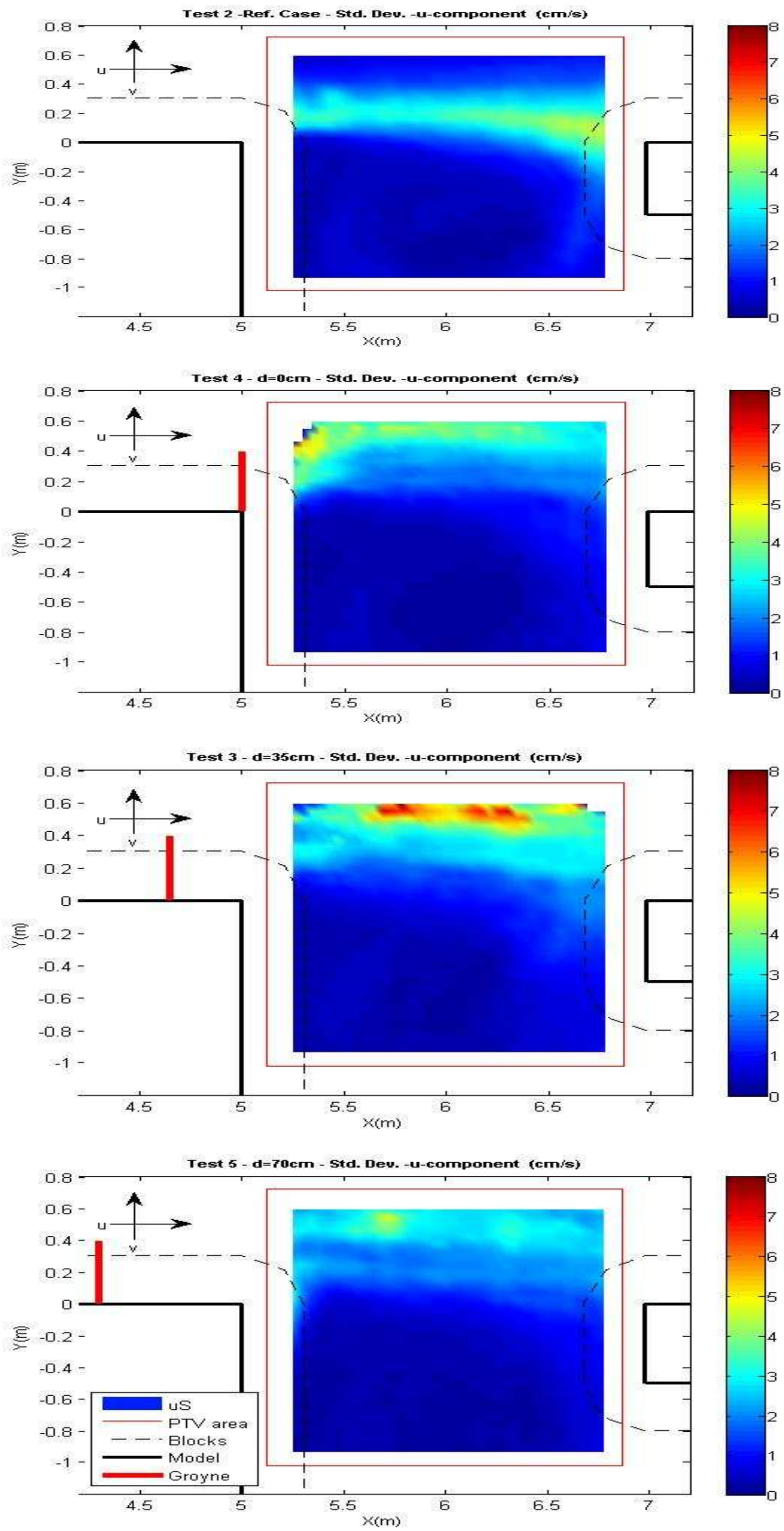

Figure 5.1.4. Series 1. Std. Deviation u-component (u_{std}) from PTV data (cm/s).

5.1.1.4.Transverse velocity.

- Lateral profiles.

This section shows the results of the mean transverse velocity from PTV and ADV results along three different cross sections: "A"(X=5.47m), "B"(X=5.98m) and "C"(X=6.47m).

As it was drawn in Figure 5.1.2., the ADV values are plotted with single marks and the PTV results by means of a solid line.

From *Figure 5.1.5* it is shown that in section "A"(X=5.47m) the mean transverse velocity is positive at all points inside the harbour basin (Y<0m) and the differences between experiments appear at the harbour entrance.

For Tests 2 and 5, the values remain close to 0 cm/s, but Test 3 shows the highest values. It denotes that the effect of the groyne is higher for Test 3 between points A1 and A2.

In section "B", Test 3 shows differences with respect to the reference case with regard to PTV data, but they are more evident in section "C"(X=6.47m).

For section "C", Test 3 gives a steep profile that shifts from positive values at the stream to -5 cm/s inside the harbour basin. It indicates that this configuration produces a higher gradient for the transverse velocity near the downstream sidewall of the harbour entrance than the other cases.

With respect to the ADV data, in the river stream ADV values show negative results for Test 3, however these values are positive for Tests 4 and 5. This characteristic is present in all the cross sections and it can be attributed to the fact that when the groyne is located at d=35 cm a shift over the depth is produced and then the mean transverse velocity is negative.

- Standard deviation. Transverse velocity.

Figure 5.1.6 represents the distribution of the standard deviation for the transverse velocity (v_{std}) from PTV results. The location of the mixing layer and its extension can be analysed from the location of the highest values of the standard deviation as it was discussed for the streamwise velocity.

Test 2 shows an area with values of v_{std} around 3 cm/s along the harbour entrance. This area shifts towards the harbour basin at the downstream side of the entrance. However, Test 4 (groyne at d=0 cm) presents higher values of v_{std} near the upstream corner as it was shown for the streamwise component. In this case, these values reach 3 cm/s and cover a larger area.

Comparing Test 3 (groyne at d=35 cm) with the previous cases, high v_{std} values are obtained at the river stream, with values higher than 4 cm/s. On the other hand, Test 5 (groyne at d=70 cm) provides the same distribution of v_{std} than Test 4, but in this case, there are no high v_{std} values near the upstream corner.

It can be concluded that the area with high v_{std} values moves to the river stream, as it was drawn for u_{std}, and covers a wider area in front of the harbour entrance than for the reference case.

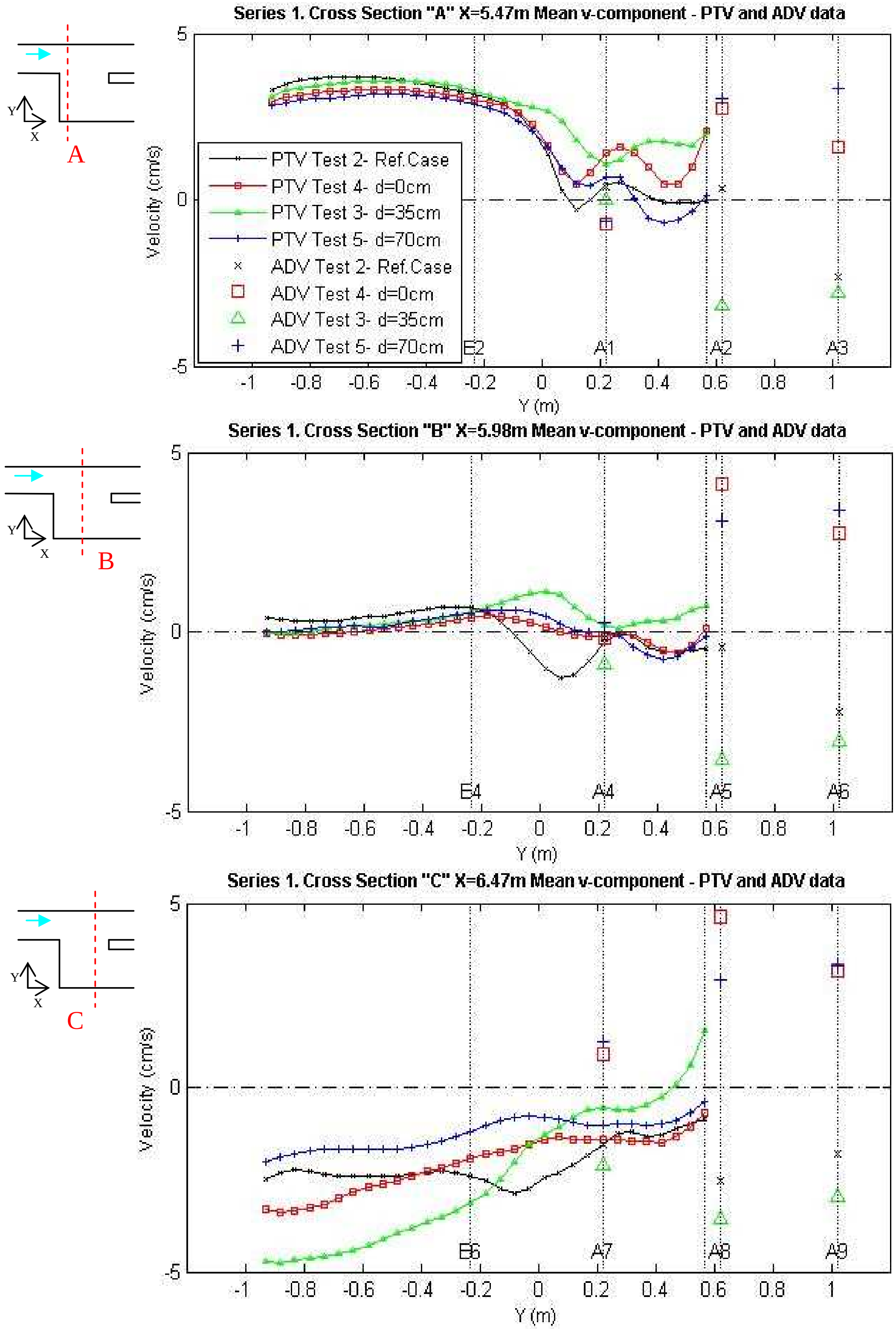

Figure 5.1.5. Series 1. Lateral profile mean v-component (cm/s).
Sections A(X=5.47m), B(X=5.98m) and C(X=6.47m).

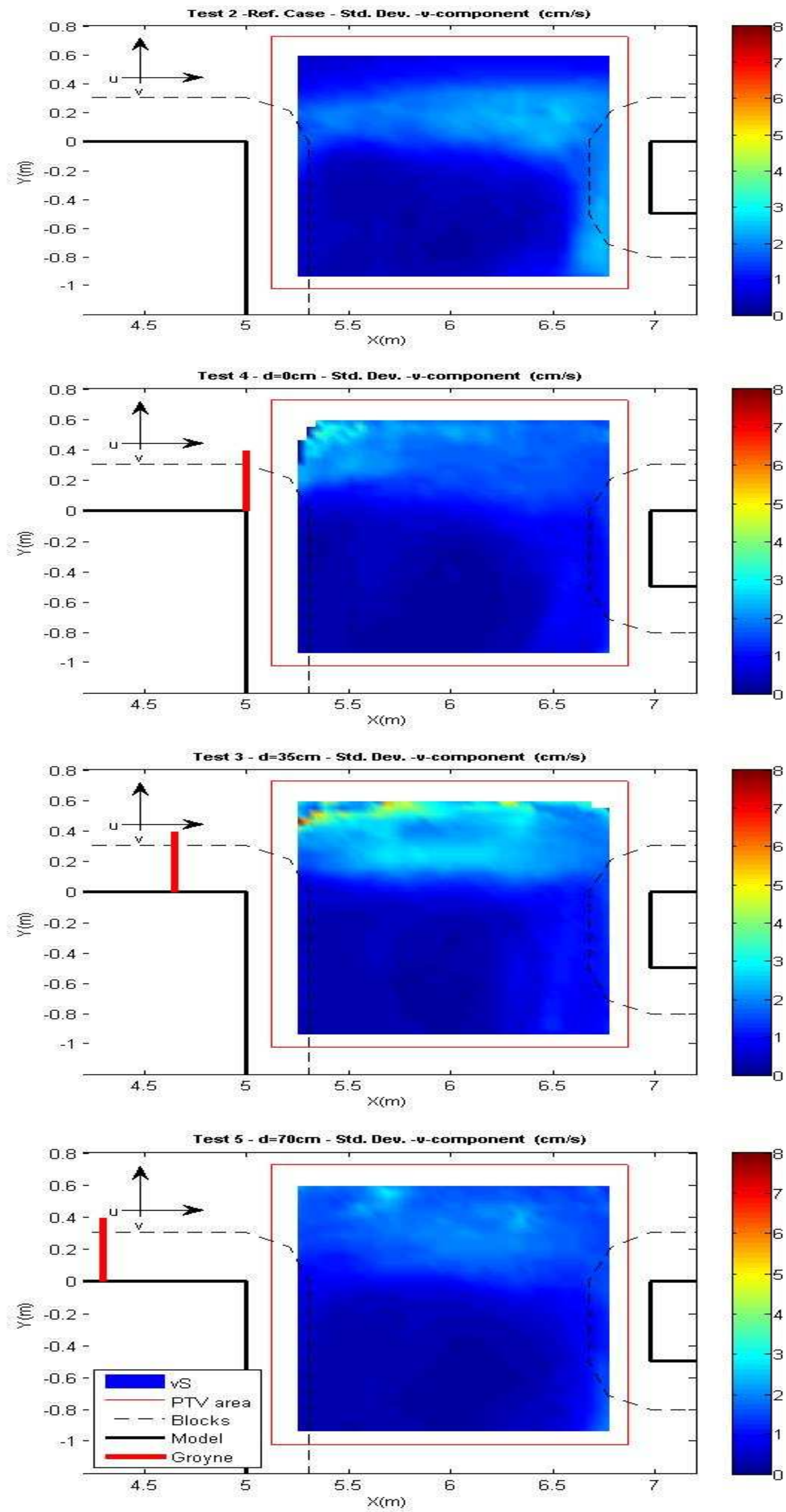

Figure 5.1.6. Series 1. Std. Deviation v-component from PTV data (cm/s).

5.1.1.5. Estimation of flow exchange through the harbour entrance.

Two different longitudinal sections will be considered in this part: one is located inside the harbour basin, "F"(Y=-0.23m), and the second section corresponds with the harbour entrance line, "HE" (Y=0m).

In this part the lateral profile of the transverse velocity, *v*, along both sections will be studied for the different experiments of Series 1. PTV results in these sections are averaged and a polynomial function is adjusted to these mean values of the transverse velocity. Mean values of the transverse velocity from PTV data are defined from X= 5.12m to X=6.86m (width of the PTV area).

The polynomial function will have degree five to match the profile of the mean transverse velocity and the shape of the function. The polynomial satisfies the following expression:

$$f(x) = \sum_{i=0}^{n=5} C_i x^i$$

An estimation of inflow and outflow discharge across both sections is established from the integration of this function.

The polynomial function is integrated along the x-coordinate and over the depth, taking into account the geometry of the harbour basin, which changes due to the presence of the stone blocks (the left bank achieves the x-coordinate X=5.3 m and the right bank begins at X=6.67 m).

A straightforward algorithm divides the interval X (5.12, 6.86) in steps of 0.01 cm and calculates the average value of *f(x)* in each step. The flow rate is the sum of all these values times the length of each interval (0.01 cm).

A new x-axis is employed to determine the integral. The polynomial achieves v=0 cm/s at $X=X_o$, and this point is defined as x_Q=0 m. This value will be different for each experiment.

According with these new axis, Q_{out} is defined as the outflow rate from harbour to river (result of the integration from the left side of the PTV area), and, Q_{in}, the inflow rate from river to harbour (from x_Q =0 cm to the right side of the PTV area). The flow rate is considered negative when it enters into the harbour basin (Q_{in}<0 l/s).

The same methodology is applied to section "HE" (Y=0m).

Figure 5.1.7 shows the lateral profile of the mean transverse velocity for Series 1 along section "F", together with the mean EMS values at locations E2, E4 and E6.

The results of Q_{in} and Q_{out} for all experiments are indicated in *Table 5.1.2.a..* and *Figure 5.1.8.*

	Section F		***Section HE***	
	Q_{in} (l/s)	***Q_{out} (l/s)***	***Q_{in} (l/s)***	***Q_{out} (l/s)***
Test 2 – Reference Case.	-2.36	2.44	-2.93	0.86
Test 4 – Groyne at 0 cm.	-2.06	2.16	-1.58	1.34
Test 3 – Groyne at 35 cm.	-2.58	2.49	-1.30	2.44
Test 5 – Groyne at 70 cm.	-1.39	2.04	-0.94	1.34

Table 5.1.2.a. Series 1. Inflow and outflow rates for Sections "F" and "HE".

The results of Q_{in} and Q_{out} for all experiments shown in the previous table are transformed into percentages of reduction/increase with respect the reference case in *Table 5.1.2*.b. Positive values denote an increase in the inflow or outflow rates.

	Section F		**Section HE**	
	% Q_{in}	**% Q_{out}**	**% Q_{in}**	**% Q_{out}**
Test 4 – Groyne at 0 cm.	-12.80	-11.44	-45.96	56.45
Test 3 – Groyne at 35 cm.	9.55	2.54	-55.67	184.59
Test 5 – Groyne at 70 cm.	-41.11	-16.25	-68.02	56.07

Table 5.1.2.b. Series 1. Reduction rates of inflow and outflow results. Sections "F" and "HE".

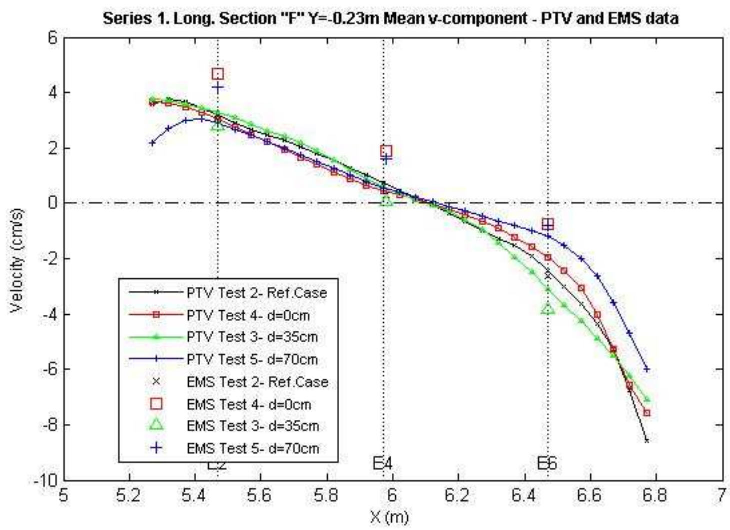

Figure 5.1.7. Series 1. Lateral profile of mean v-component at Section "F"(Y=-0.23m).

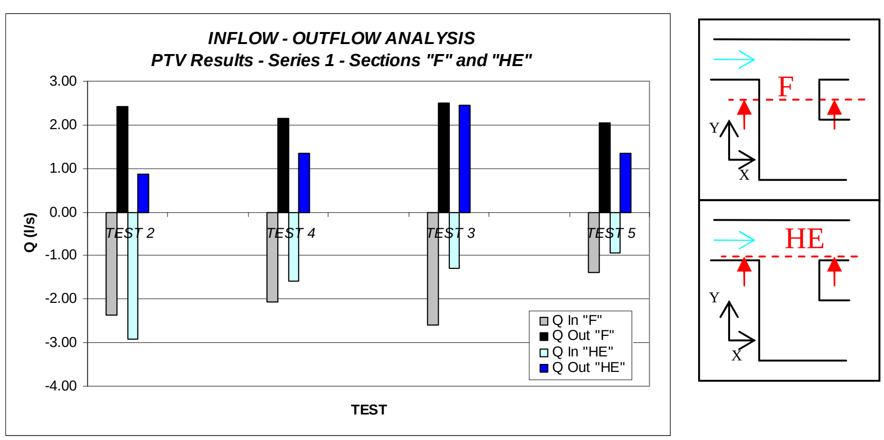

Figure 5.1.8. Series 1. Inflow and outflow rates for Sections "F" and "HE".

From Figure 5.1.7 it is obtained that Test 5 (groyne at 70 cm) shows the lower values of the mean transverse velocity at Section F. Consequently, the inflow and outflow rates for Test 5 are lower than for the other cases as it can be seen in Figure 5.1.8.

From Figure 5.1.8, it can be seen that the reference case presents similar inflow and outflow rates at Section "F" (black and grey bars) and it indicates that the behaviour of the primary gyre in this case creates an exchange across section "F" that is almost symmetric at the surface.

The highest inflow rate is given in Test 3 (groyne at 35 cm) and it is due to the fact that the mean transverse velocities near the downstream sidewall are higher for this configuration as it is observed in Figure 5.1.7 (green line).

However, Test 5 shows asymmetry between these two rates. The effect of the groyne in Section "F" is larger for Test 5 (groyne at 70 cm). For this case, the inflow rate decreases significantly and consequently, there is a higher unbalance between Q_{in} and Q_{out}. The amount of water which is moving from harbour to river is higher than the amount of water which is entering the basin, according with results at the surface.

It reveals that the groyne at d=70 cm causes an asymmetric gyre which has higher differences for the transverse velocity along Section "F".

This asymmetry in the results reveals asymmetry over the depth to balance the amount of water which is entering and leaving the harbour.

With respect to Section "HE", the asymmetry is principally present in Tests 2 and 3. For the reference case, the inflow rate Q_{in} is much larger than Q_{out}. However, Test 3 (groyne at 35 cm) presents the same value for the outflow rate, but a lower inflow towards the harbour basin.

It can be concluded that the configuration with the groyne at 70 cm presents higher effects on the mean transverse velocities and the related exchange across the harbour entrance than the other cases. Larger reduction rates are obtained for this configuration.

It is assumed that the accuracy of this method to obtain the flow exchange is not valid when the objective is to find the exact value of the exchange.

It is known that the velocity profile over the depth is not constant, and it is not possible to establish a precise vertical profile because of lack of data over the depth. EMS results (located at 2/3 of the water depth) are close to PTV mean values, and hence, the value at the surface has been used.

It should be noted that the flow exchange across the harbour entrance is more complex due to the 3D eddies and the presence of the mixing layer. However, the aim of this paragraph is to provide an estimation of this rate to compare differences between experiments.

5.1.1.6. Location and streamwise velocity at the centre of the mixing layer.

To establish the main characteristics of the mixing layer the estimation of the centre location has been developed. The two main parameters to define the centre of the mixing layer will be the y-coordinate, y_c, and the streamwise velocity, u_c.

The value of the streamwise velocity at the centre of the mixing layer will be obtained as follows:

$$u_c = \frac{u_h + u_r}{2} \tag{5.1}$$

where u_r is the streamwise velocity in the river and u_h is the streamwise velocity in the gyre.

During this section, PTV data will be used to obtain the previous parameters. *Figure 5.1.9* shows the four lateral profiles of the streamwise velocity at X=5.47m (Section "A") from the PTV analysis, together with the ADV values at locations Y=0.22, 0.62 and 1.02 m. The ADV values are plotted by single marks.

The values of the harbour velocity, u_h, are defined by the PTV results at the lower part of the profile. The river velocity, u_r, is estimated from the difference between the PTV and ADV data at Y=0.22 m. The velocity difference is applied to obtain an estimated value of u_r at the river stream (PTV area does not reach the river stream further than Y=0.57m). From these results, u_c is calculated as it was defined before.

The red dash lines define the values of u_r and u_h. The width of the mixing layer is obtained from the intersection of both horizontal lines with the tangent line of the lateral profile. The double arrow represents the mixing layer width, δ. The y-coordinate of the centre, y_c, is obtained from the intersection of u_c and the velocity profile.

Table 5.1.3 summarizes the results of all experiments in three different cross sections (X=5.47m, 5.98m and 6.47m).

		Mixing layer centre		
CASE	X(m)	u_c (cm/s)	δ (cm)	y_c (cm)
Test 2 - Ref. Case	5.47	19.32	0.35	0.22
	5.98	19.26	0.43	0.21
	6.47	19.53	0.5	0.2
Test 4- Groyne at d=0 cm	5.47	21.00	0.70	0.5
	5.98	20.34	0.65	0.45
	6.47	20.16	0.55	0.4
Test 3- Groyne at d=35 cm	5.47	20.02	0.50	0.47
	5.98	19.36	0.6	0.45
	6.47	18.75	0.6	0.38
Test 5- Groyne at d=70 cm	5.47	23.15	0.65	0.45
	5.98	21.00	0.7	0.41
	6.47	20.80	0.75	0.37

Table 5.1.3. Series 1. Characteristics of the mixing layer.

From the previous table several conclusions can be drawn. The most relevant aspect is the presence of two mixing layers in all experiments with a groyne upstream the harbour entrance. A small mixing layer is created from the edge of the groyne and it overlaps with the mixing layer due to the transition between river and harbour. In Figure 5.1.12, the clear variation along the lateral profile which distinguishes the two mixing layers for Tests 3, 4 and 5 is shown. This change along the lateral profile is more obvious in Test 4 (groyne at d=0).

The width of the mixing layer in each case depends on diverse characteristics. First, the slope or gradient of the velocity profile establish widely the width of the mixing layer. The width is lower for the cases in which the profile is steeper. Second, the ADV values for all the experiments, except for the reference case, are higher in the river stream, and consequently, the estimated streamwise velocity to determine u_r is higher in these cases.

A clear increase of the mixing layer width is observed in downstream direction, except for the case with the groyne at d=0 cm. This difference can be attributed to the fact that the groyne is located too close to the harbour entrance and consequently, at X=5.47m the high turbulence created by the groyne develops a larger area where the mixing layer follows a larger initial width.

The velocity gradient is relevant because it is related with turbulence production and Reynolds stresses as it was defined in Chapter 3. Consequently, the experiment with lower velocity gradient along the streamwise velocity profile will reveal less turbulence production, and as a result lower levels of mixing and exchange.

From this assumption, Test 4 presents the lowest gradient due to the effect of the second mixing layer in the lateral profile which originates a larger shift on the slope than other cases.

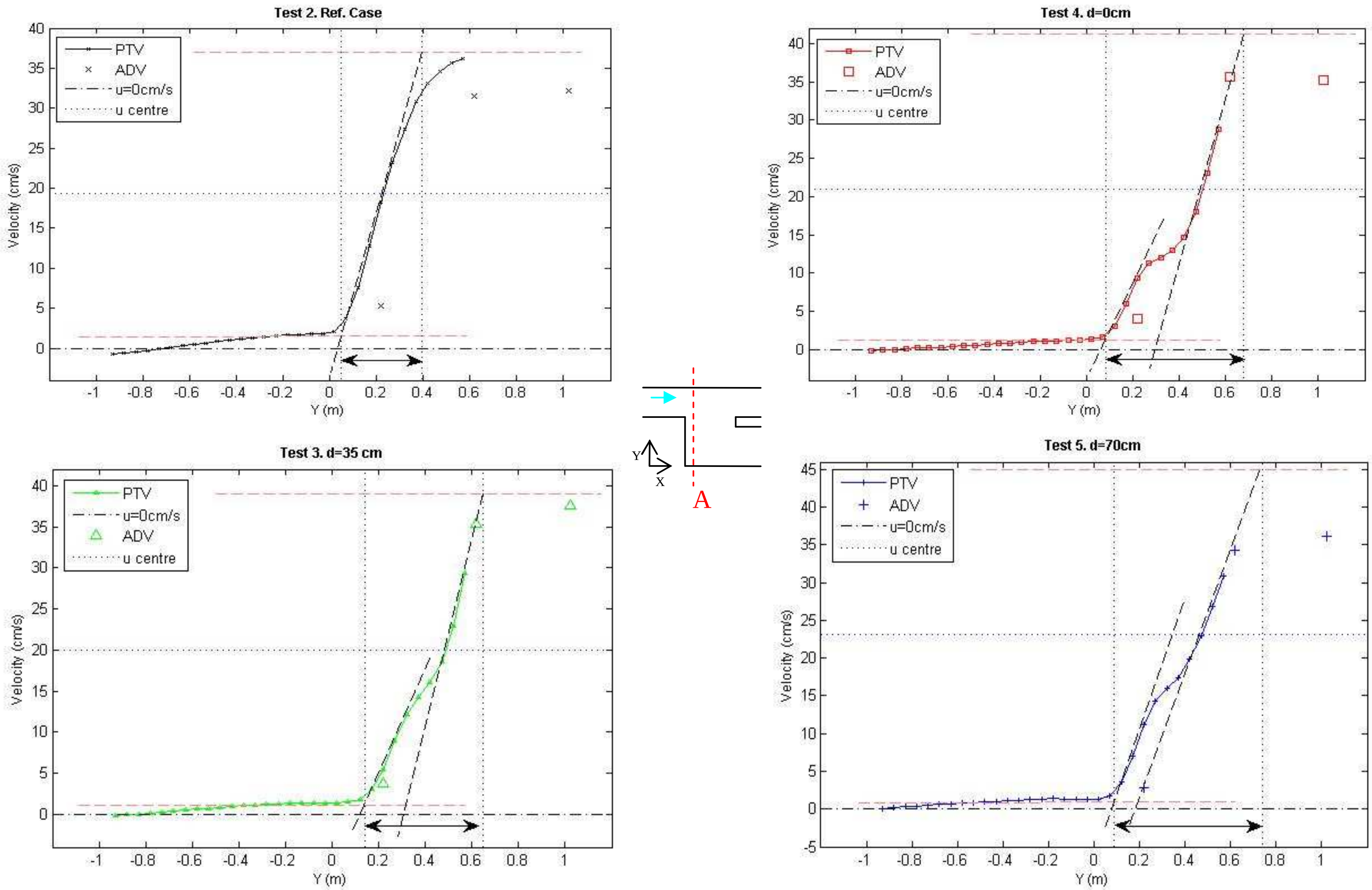

Figure 5.1.9. Series 1. Profile of mean u-component and mixing layer width. Section A (X=5.47m).

5.1.2. Turbulence properties.

5.1.2.1. Autocorrelation analysis.

The following section describes the autocorrelation analysis, as it was explained in Chapter 4, for the different groyne configurations of Series 1.

The transverse velocity component will be discussed in three different cases. From EMS data, point E6 (X=6.47m, Y=-0.23m) is studied for each experiment. From ADV data, cross section “B” at X=5.98m (points A4 and A5) and the longitudinal section “G” at Y=0.22m (points A1 and A7) have been considered.

a) EMS 6.

Figure 5.1.10 shows three different plots. The first two figures are the time signals for each experiment from EMS data at point E6. The last figure shows the autocorrelation functions from E6 data for each experiment.

For all experiments, time series in this EMS location were compared to themselves, with a time delay τ, where $\tau = \Delta t * n = 0.01 * n$ (s). The original time series has a data set with 30,000 values (5 minutes of recording), but only 20,000 will be used during the analysis.

Finally, a total of 5,000 different comparisons were made for each point. Consequently, there is a maximum lag of 50 seconds between the unaltered time series and the lagged series n=5,000 (5,000·0.01=50s is the largest lag, ¼ of the total data set).

From the comparison of the four different autocorrelation functions it is clear that the reference case (black line) shows higher periodicity and high amplitude values, i.e. it reaches a minimum of R=-0.5 for a time delay of τ =6s. The time scales are shorter for this case.

For Test 4 (groyne at d=0 cm), the autocorrelation functions shows a totally different pattern which falls suddenly to R=0.6 at the first time delays. Tests 3 and 5 recover the initial slope of the function and Test 5 (groyne at d=70 cm) presents some periodicity as in Test 2.

Time signals for Tests 2 and 5 (black and blue lines, respectively) confirm this periodicity for the transverse component at this point.

These results symbolize that the pile groyne at location E6 loses effect when it is located far from the harbour entrance.

c) Section B.

For this cross section, two ADV locations from the river stream to the harbour entrance are used: A4 (located at Y=0.22m) and A5 (located in the centre of the river, Y=0.62m). Both points are located in X=5.98 m.

Time series in these two ADV locations were compared to themselves, with a time delay of $\tau = n \cdot \Delta t$, where Δt =0.05 s, because for the ADV measurements, the original time series has a data set with 6,000 values (7,500 values for Test 5) for a period of 5 minutes.

A total of 400 different lagged series were compared with the original time series. Consequently, there is a maximum lag of 20 s between the unaltered time series and the lagged series number 400 (400* Δt =20s is the largest lag).

Figure 5.1.11 gives the autocorrelation functions for points A4 (soft line) and A5 (pointed line).

As A5 is located at the river stream (Y=0.62m), the autocorrelation function shows a fast decrease of the R values and they remain around zero for the whole range, which is characteristic of the river stream, where the time scales are smaller than in the mixing layer.

Point A4 presents longer time scales and some periodicity in Test 2 which disappears for configurations with the groyne near the upstream corner, but unexpectedly, for Test 5 (groyne at d=70 cm) a higher periodicity is found with a time interval between relative minimums of 10 s.

b) Section G.

For this longitudinal section, each figure shows two autocorrelation functions which corresponds with ADV results at point A1 (located near the upstream corner, X=5.47m), and A7 (located near the downstream corner, X=6.47m). All these points are located in Y=0.22 m.

In this section, the number of lagged series to be compared with each original time series is the same than in Section "B". *Figure 5.1.12* shows the autocorrelation functions for all experiments.

As the autocorrelation function for point A7 shows, there is a visible change of amplitudes and phase distortions when the pile groyne is located upstream the harbour entrance. For all experiments with groyne, the autocorrelation values oscillate around lower rates and present longer time periods than the reference case.

For point A1, no apparent differences are between Tests 2 and 4, but curves from Tests 3 and 5 have a negative region implying that there are significant time periods for which the lateral velocity has an opposite direction. The presence of a region of negative correlation is related with transverse continuity.

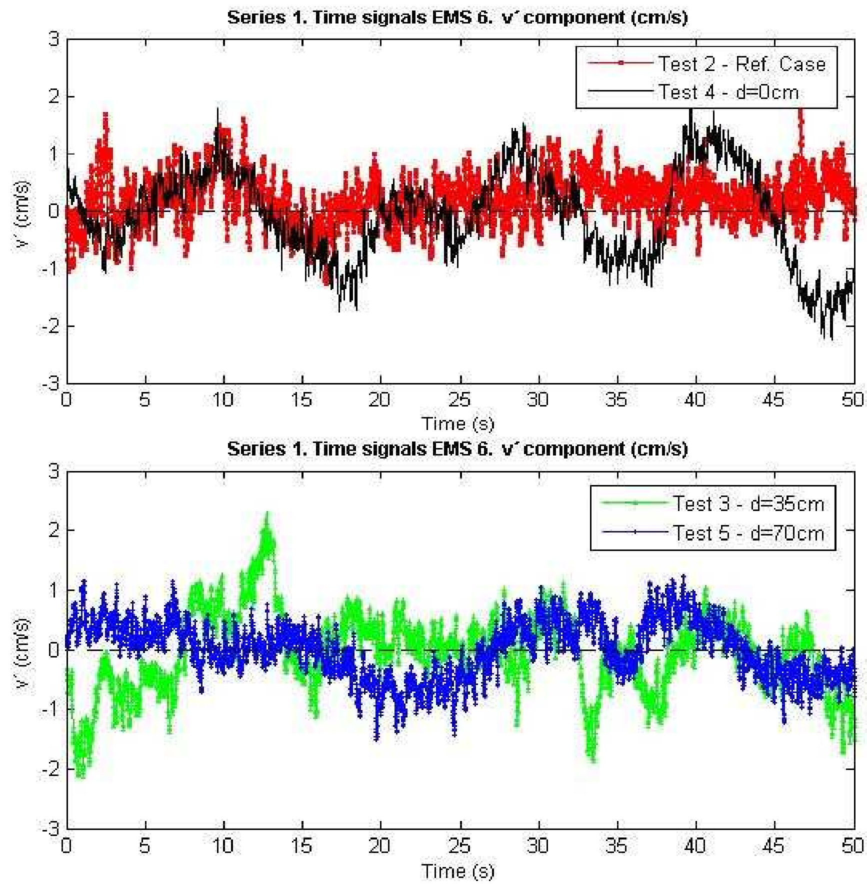

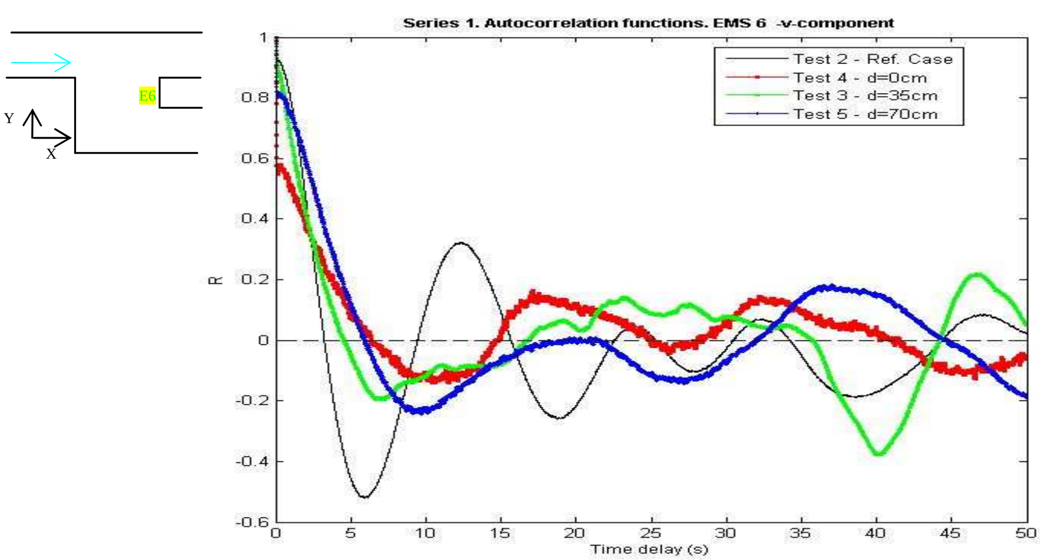

Figure 5.1.10.
Series 1. Time signals v´ (cm/s) and autocorrelation functions EMS 6 (6.47,-0.23).

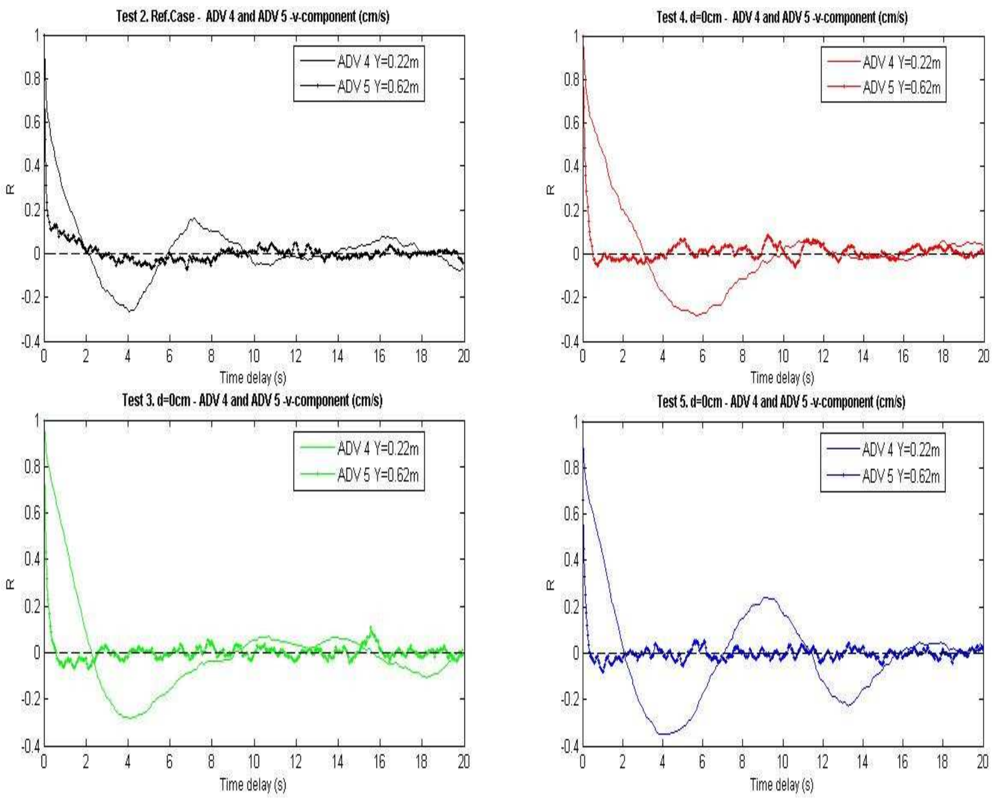

Figure 5.1.11. Series 1. Autocorrelation functions ADV 4 (5.98, 0.22) and ADV 5 (5.98,0.62).

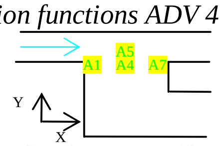

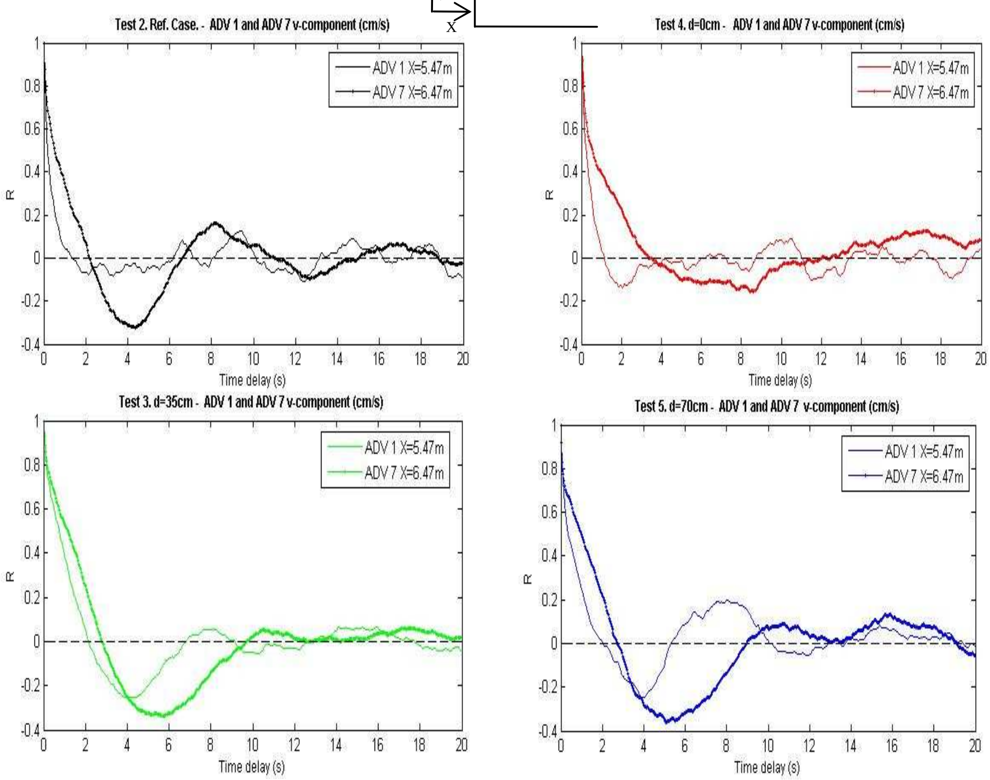

Figure 5.1.12. Series 1. Autocorrelation functions ADV 1 (5.47,0.22) and ADV 7(6.47,0.22).

5.1.2.2. Reynolds stresses.

In the present section some comparative results are included of the Reynolds stress component $\langle u'v' \rangle$, obtained from PTV data over the measurement area and results of $\langle u'v' \rangle$ and $\langle u'w' \rangle$ for different locations from the ADV measurements.

In this paragraph, u', v', w' are the fluctuating velocity components (in cm/s) obtained from the velocity series.

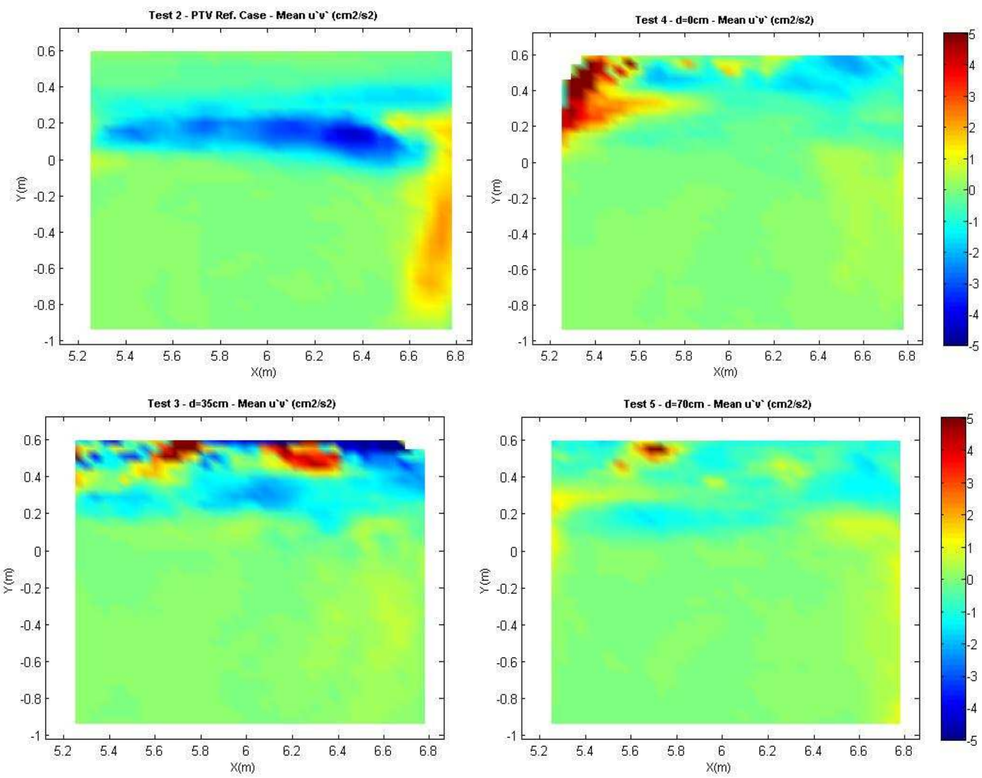

5.1.13. Series 1. Reynolds stress $\langle u'v' \rangle$ *(cm²/s²).*

As it was defined in Section 4.5., $\langle u'v' \rangle$ is negative along the harbour entrance according to the location of the mixing layer as it can be observed in Test 2 (reference case) due to the gradient between the high streamwise velocities at the river stream and the velocity within the primary gyre.

From Test 4 (d=0 cm) a displacement of the negative values is seen towards the river stream and higher stresses are observed near the edge of the groyne. This concentration is dissipated in Test 3 (d=35 cm) but high stress are observed in downstream direction.

The most significant results are obtained in Test 5 (d=70 cm), in this case the Reynolds shear stress is lower than the rest of the cases and it does not present the high values at the entrance, because the edge is located far from the corner.

It indicates that the effect of the groyne on the distribution of the stress along the entrance is significant for all cases, but the distribution is more uniform when the groyne is located far from the entrance and the high concentration of positive stresses related with high positive transverse velocities near the corner is avoided.

Reynolds stresses from ADV measurements are included in *Appendix B.*

Table 5.1.4 lists the results of $\langle u'v' \rangle$ taken from ADV measurements at points along section G (Y=0.22m), together with the values of u_{std} and v_{std} for all experiments.

			Test 2		Test 4		Test 3		Test 5	
			Ref. Case		Groyne at 0 cm		Groyne at 35 cm		Groyne at 70 cm	
Line		**X(m)**	**<u'v'>**	**u_{std} v_{std}**	**<u'v'>**	**u_{std} v_{std}**	**<u'v'>**	**u_{std} v_{std}**	**<u'v'>**	**u_{std} v_{std}**
	A1	***5.47***	-4.00	11.00	-4.00	9.00	-4.00	8.00	-3.00	6.00
G	***A4***	***5.98***	-6.00	14.00	-2.00	4.00	-3.00	9.00	-4.00	7.00
Y=0.22m	***A7***	***6.47***	-8.00	15.00	-1.00	4.00	-1.00	8.00	-2.00	5.00

Table 5.1.4. Series 1. Comparison. Reynolds stress u'v' and std. u and v-components (cm^2/s^2).

If these values are compared with the previous PTV maps, lower stresses are obtained from PTV measurements in all cases. For example, in Test 5, ADV measurements give values between -2 and -4 cm^2/s^2, but figure 5.1.13 remains in a range from -1 to 1 cm^2/s^2.

From the previous table, it is possible to conclude that all values are around 0.4 times the product of u_{std} and v_{std} at the points located along Y=0.22m as it can be expected from locations within the mixing layer.

If values of u_{std} and v_{std} are compared with the Reynolds stress components for Tests 3, the results show that the value is lower than 0.4 u_{std} v_{std} at point A7. This difference suggest that the flow pattern at the location A7 changes due to the groyne and it does not fulfil the conditions associated to the mixing layer.

The difference between PTV and ADV results with respect to the Reynolds stress component can be attributed to different flow conditions over the depth. Higher stresses are obtained from ADV measurements in all cases.

5.2. Data analysis for Series 2.

In this section, the analysis of the experiments of Series 2 is given. There are two experiments in Series 2 and have the same location of the groyne upstream the entrance than Test 3 (d=35 cm). Test 6 (n=6 piles) and Test 7 (n=5 piles) have different number of piles with respect Test 3 (7 piles).

5.2.1. Mean flow.

The same considerations will be taken into account for Series 2 as it was presented in section 5.1.

5.2.1.1. Velocity field.

Figure 5.2.1 shows the modified vector map of the mean velocity in each case. The groyne is sketched for Tests 6 and 7 as in Test 3, and the different lengths related with the experiments are appreciable. At Y=0.22m, a decrease of the velocity in all cases with groyne is seen.

The high transverse components along the harbour entrance in Test 3 are reduced in Tests 6 and 7.

The velocimetry comparison between ADV and PTV data in the next paragraph shows the numerical results for these experiments.

5.2.1.2. Velocimetry comparison ADV versus PTV.

The results are listed in *Table 5.2.1.* For this series, all ADV measurements are lower than PTV data for all cases. All points along section “H” (Y=0.62m) show higher streamwise velocities from PTV results as it can be expected from the typical (logarithmic) vertical distribution of the velocity.

After several verifications, it must be concluded that the differences between ADV and PTV noted for Series 1 (lower PTV values at the river stream) are not a consequence of a possible error during the PTV post processing. Consequently, the PTV results will be considered as they were defined until now.

New experiments with configurations of Series 1 should be carried out to obtain new PTV data and evaluate the new results with the previous analysis.

If values from ADV and PTV data for Tests 6 and 7 are compared with the reference case, it is shown that lower velocities along Y=0.22m are developed.

The ADV values are higher for Test 7 along the harbour entrance, therefore this aspect can reveal that a lower number of piles is less effective on the reduction of the velocity along the entrance and it presents more similarities with respect to the reference case.

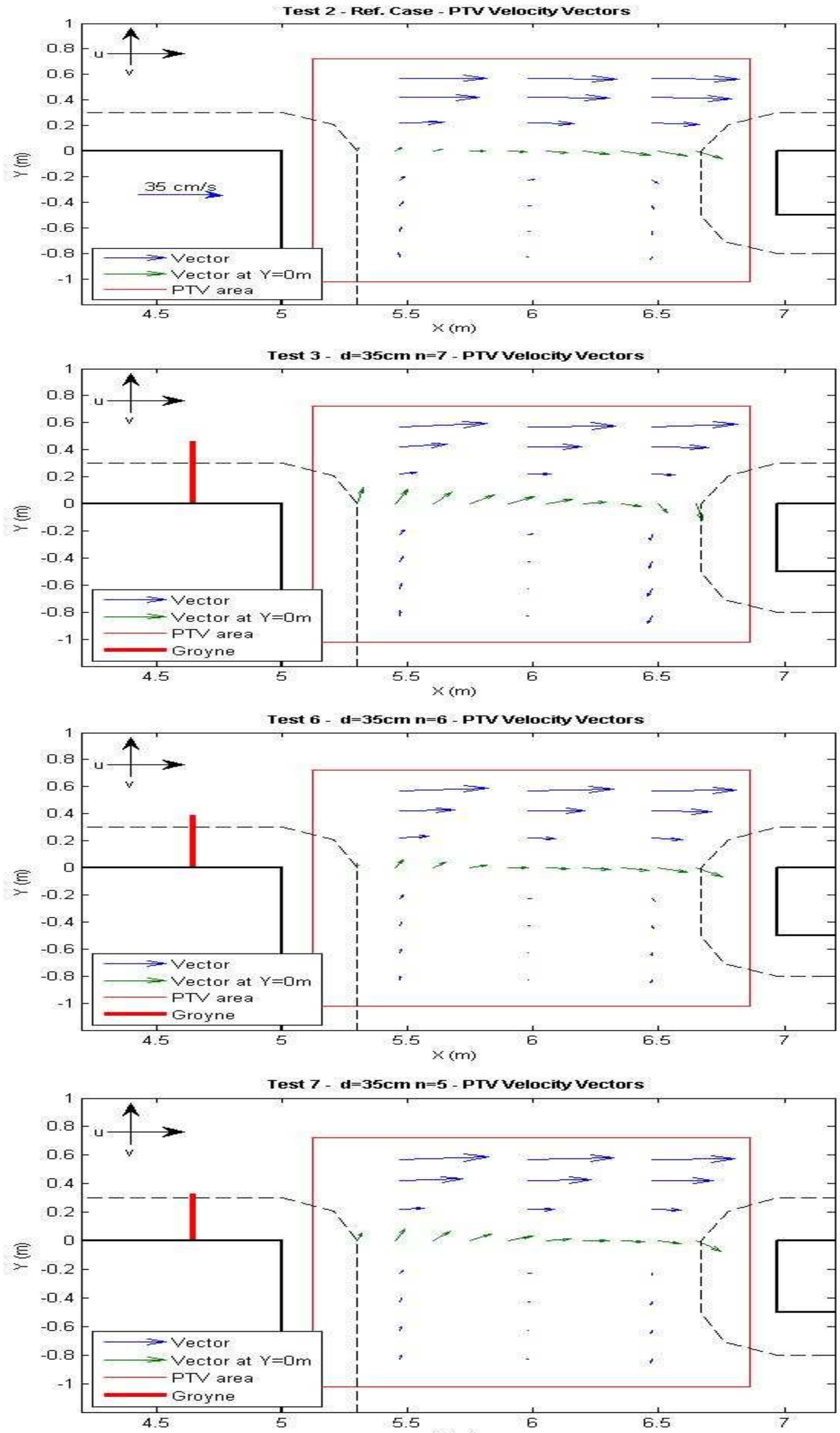

Figure 5.2.1. Series 2. Velocity vectors from PTV data.

Test 2 – Ref. Case.

POINT	Coordinates		ADV	PTV	
	X(m)	Y(m)	$\sqrt{(u^2+v^2)}$(cm/s)		Δ (cm/s)
A1	5.47	0.22	5.33	18.28	12.95
A2	5.47	0.62	31.47	36.20	4.73
A4	5.98	0.22	10.01	18.98	8.96
A5	5.98	0.62	31.06	36.60	5.54
A7	6.47	0.22	11.96	20.24	8.28
A8	6.47	0.62	29.20	36.35	7.15

Test 3 – n=7 piles

POINT	Coordinates		ADV	PTV	
	X(m)	Y(m)	$\sqrt{(u^2+v^2)}$(cm/s)		Δ (cm/s)
A1	5.47	0.22	3.75	5.60	1.85
A2	5.47	0.62	35.48	29.41	-6.07
A4	5.98	0.22	6.85	7.56	0.71
A5	5.98	0.62	34.78	29.49	-5.30
A7	6.47	0.22	7.57	8.01	0.45
A8	6.47	0.62	34.18	28.89	-5.30

Test 6 – n=6 piles

POINT	Coordinates		ADV	PTV	
	X(m)	Y(m)	$\sqrt{(u^2+v^2)}$(cm/s)		Δ (cm/s)
A1	5.47	0.22	3.08	11.71	8.63
A2	5.47	0.62	33.82	35.04	1.22
A4	5.98	0.22	5.47	11.08	5.61
A5	5.98	0.62	33.46	34.01	0.55
A7	6.47	0.22	5.94	12.26	6.32
A8	6.47	0.62	33.21	33.98	0.77

Test 7– n=5 piles

POINT	Coordinates		ADV	PTV	
	X(m)	Y(m)	$\sqrt{(u^2+v^2)}$(cm/s)		Δ (cm/s)
A1	5.47	0.22	4.58	10.31	5.73
A2	5.47	0.62	32.48	37.21	4.74
A4	5.98	0.22	6.21	10.94	4.73
A5	5.98	0.62	31.03	36.48	5.45
A7	6.47	0.22	7.50	12.85	5.34
A8	6.47	0.62	31.45	35.40	3.95

Table 5.2.1. Series 2. Comparison of flow velocities from ADV and PTV.

5.2.1.3. Streamwise velocity.

- Lateral profiles.

Figures 5.2.2 and *5.2.3* show the lateral profiles of the streamwise velocity for this series in sections A (X=5.47m) and B(X=5.98m).

Tests 6 and 7 present a higher velocity gradient along both sections, but the shift along the profile due to the presence of two mixing layers is seen in Test 6 (blue line), but it is not distinguished in Test 7 (magenta line).

- Standard deviation. Streamwise velocity.

From *Figure 5.2.4* it can be concluded that a lower number of piles modifies the location of the high standard deviation area towards the river. In these new cases, the area is wider than in Test 2, but it does not reach the downstream side of the harbour as in the reference case. For Test 7 (n=5), there is an apparent tendency towards the downstream side, but it does not develop to the downstream corner as in the reference case.

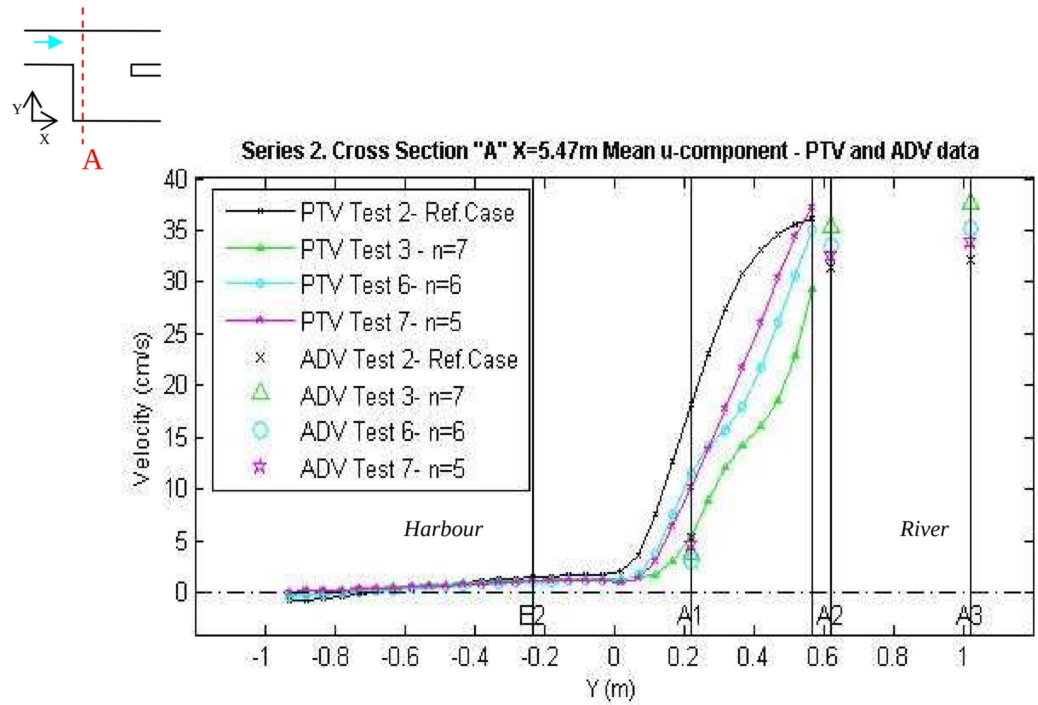

Figure 5.2.2. Series 2. Lateral profile mean u-component (cm/s). Section A. (X=5.47m).

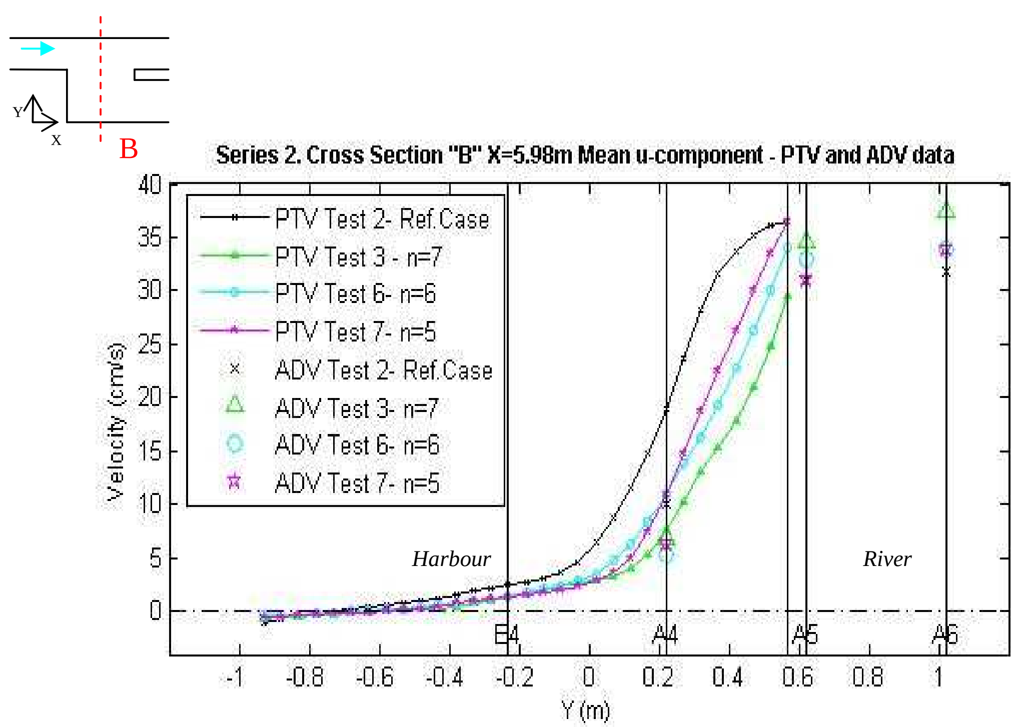

Figure 5.2.3. Series 2. Lateral profile mean u-component (cm/s). Section B. (X=5.98m).

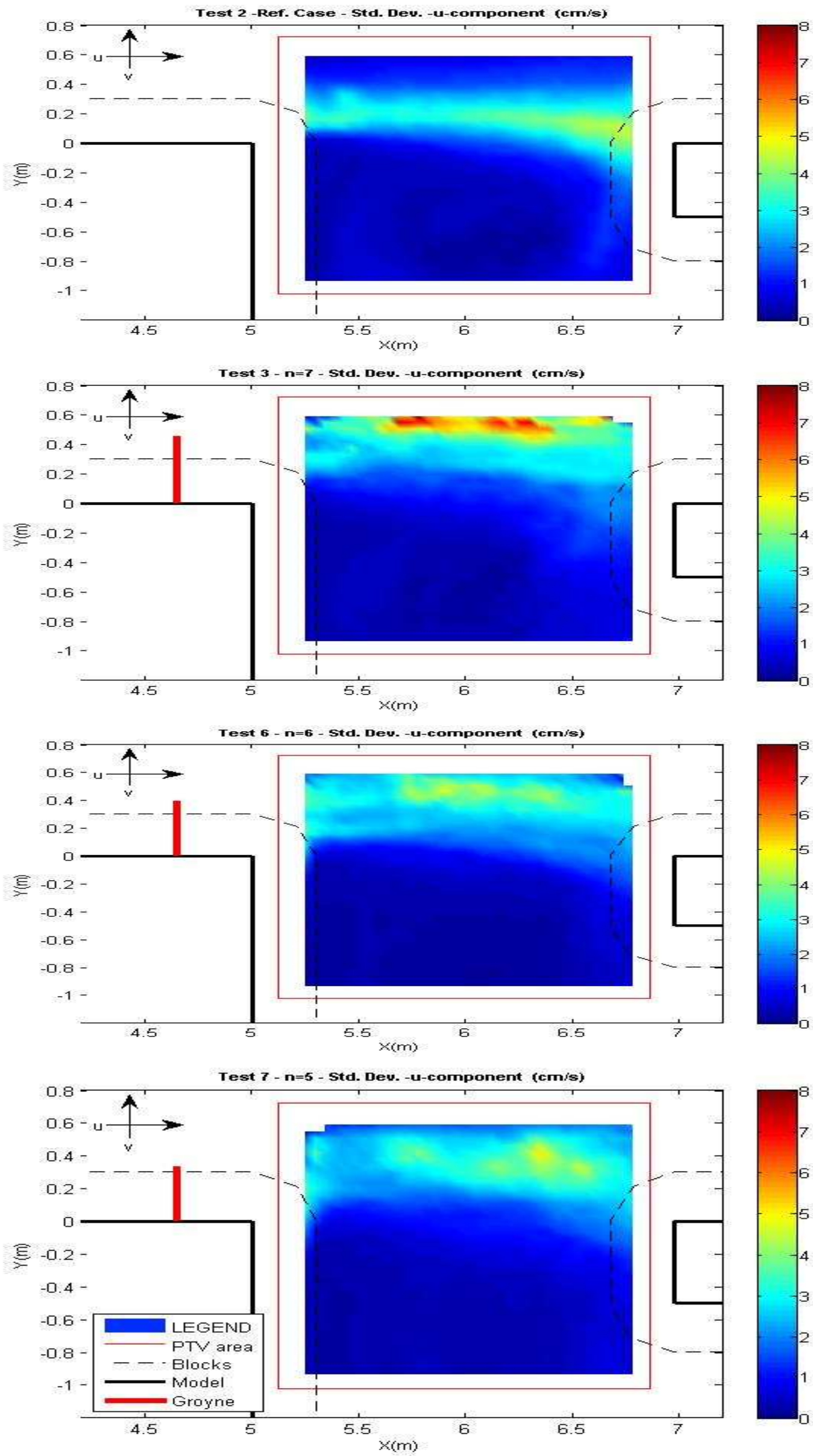

Figure 5.2.4. Series 2. Std. Deviation u-component from PTV data (cm/s).

5.2.1.4. Transverse velocity.

- Lateral profiles.

Several aspects can be discussed from *Figure 5.2.5*. First, Tests 6 and 7 present intermediate results along sections A and B, between the reference case and Test 3. It means that the variations in the transverse velocity decrease with the number of piles.

The second aspect concerns with the high values given by ADV measurements in Test 7 at the river stream.

From these results, it can be concluded that Test 6 presents better conditions in relation with the transverse component, because high negative values at the river stream can imply a higher exchange into the harbour basin.

In addition, an additional aspect is taken from these profiles. Test 3 provides higher transverse velocities in Section “C” than Tests 6 and 7. In this section, experiments of Series 2 present lower values than the reference case. As a result, lower inflow has to be expected for these cases near the downstream side of the harbour.

- Standard deviation. Transverse velocity.

Figure 5.2.6 presents the plots of the standard deviation v_{std} for Series 2. It is noted that with a lower number of piles the high standard deviation values of Test 3 disappear at the river stream, but it has to be noted that Test 7 presents the same trend towards the downstream side of the harbour basin as the reference case. This tendency is less appreciable in Test 6.

Together with the results of the streamwise velocity, it can be concluded that the configuration of five piles is less effective than the other cases. Its effect on the velocity gradient, and consequently, on the production term is significant, but the standard deviation results show that the mixing layer moves towards the harbour basin as in the reference case.

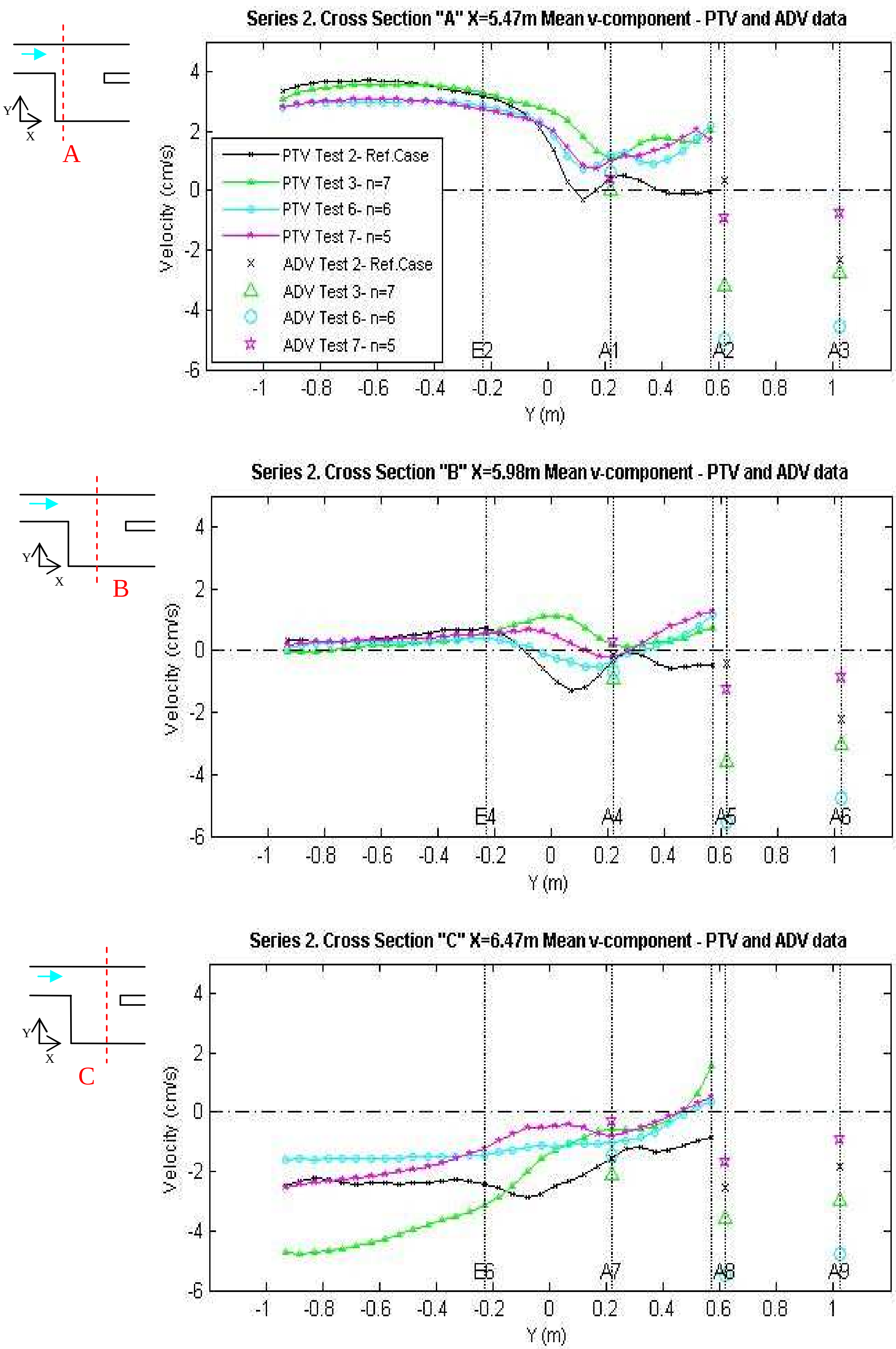

Figure 5.2.5. Series 2. Mean v-component (cm/s).
Sections A(X=5.47m), B(X=5.98m) and C(X=6.47m).

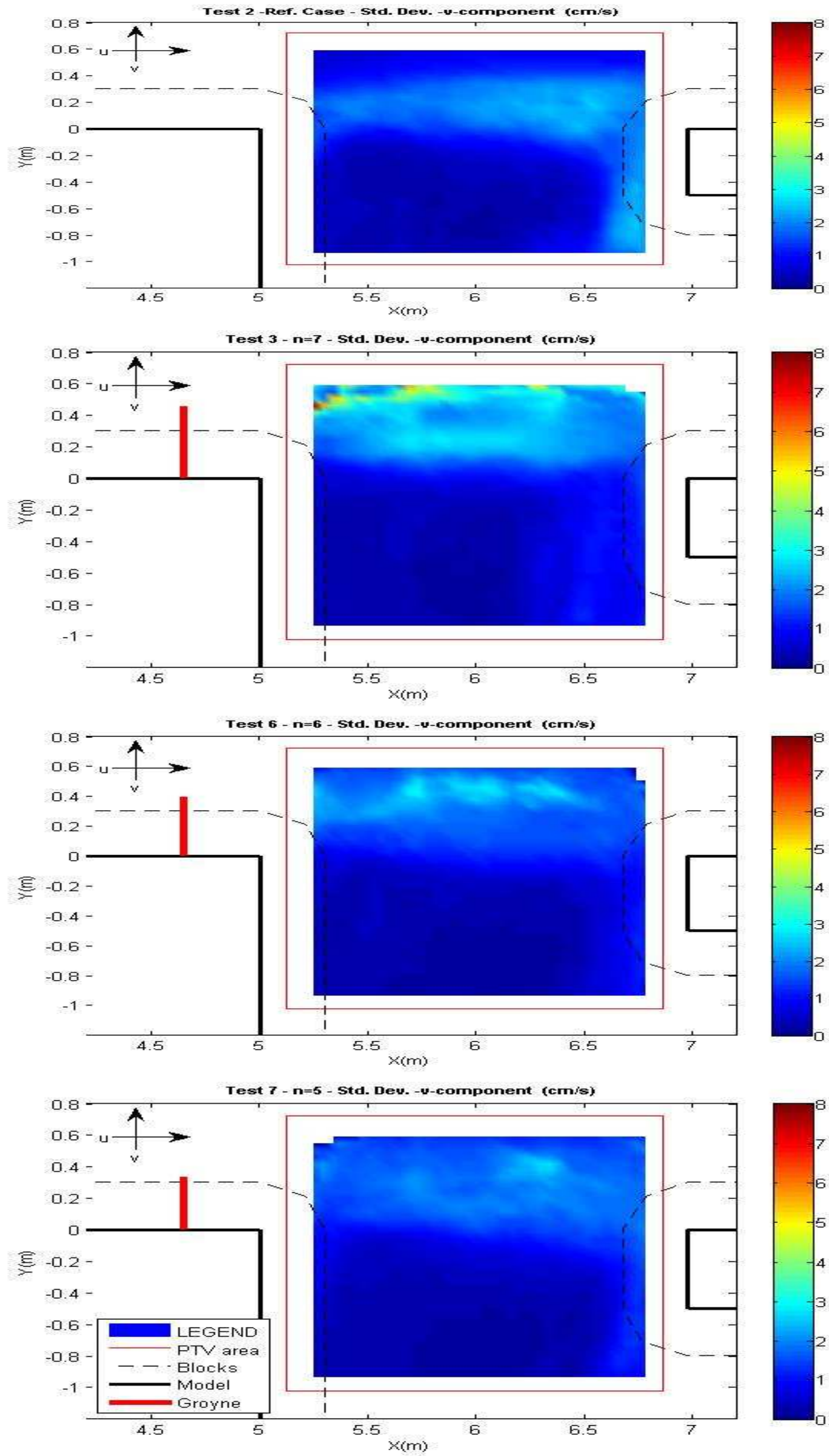

Figure 5.2.6. Series 2. Std. Deviation v-component from PTV data (cm/s).

5.2.1.5. Estimation of flow exchange through the harbour entrance.

Figure 5.2.7 shows the lateral profile of the mean transverse velocity for Series 2 along section "F", together with the mean EMS values at locations E2, E4 and E6.

From these mean transverse velocities the inflow and outflow rates obtained as it was described in Section 5.1.1.5 are obtained. These values are listed in *Table 5.2.2.* The percentages of reduction/increase with respect the reference case are given in *Table 5.2.2*.b. Positive values denote an increase in the inflow or outflow rates as in Series 1.

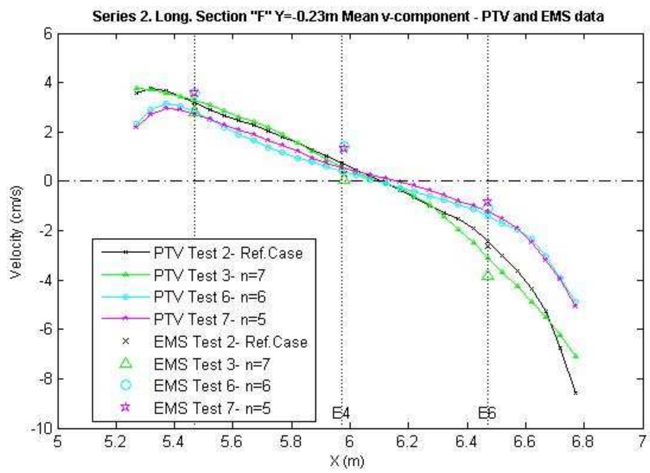

Figure 5.2.7. Series 2. Lateral profile of mean v-component at Section "F"(Y=-0.23m).

	Section F		Section HE	
	Q_{in} (l/s)	Q_{out} (l/s)	Q_{in} (l/s)	Q_{out} (l/s)
Test 2 – Reference Case.	-2.36	2.44	-2.93	0.86
Test 3 – n=7 piles	-2.58	2.49	-1.30	2.44
Test 6 – n=6 piles	-1.35	1.85	-1.26	1.11
Test 7 – n=5 piles	-1.26	1.96	-0.70	1.50

Table 5.2.2 a. Series 2. Inflow and outflow rates for sections "F" and "HE".

	Section F		Section HE	
	% Q_{in}	% Q_{out}	% Q_{in}	% Q_{out}
Test 3 – n=7 piles	9.55	2.54	-55.67	184.59
Test 6 – n=6 piles	-42.66	-24.16	-57.15	28.71
Test 7 – n=5 piles	-46.51	-19.41	-76.13	75.14

Table 5.2.2.b. Series 2. Reduction rates of inflow and outflow results. Sections "F" and "HE".

From these results, a clear difference is observed between tests 6 and 7, in comparison with Test 3. High rates of reduction in the inflow values are observed for Series 2. These percentages are higher for Test 6 at Section "F" and the values obtained at Section "HE" present symmetric results for this configuration which are not present in other cases.

Figure 5.2.8 shows the inflow and outflow rates for Series 2 along sections "F" and "HE" as it was explained for Series 1 in the previous section.

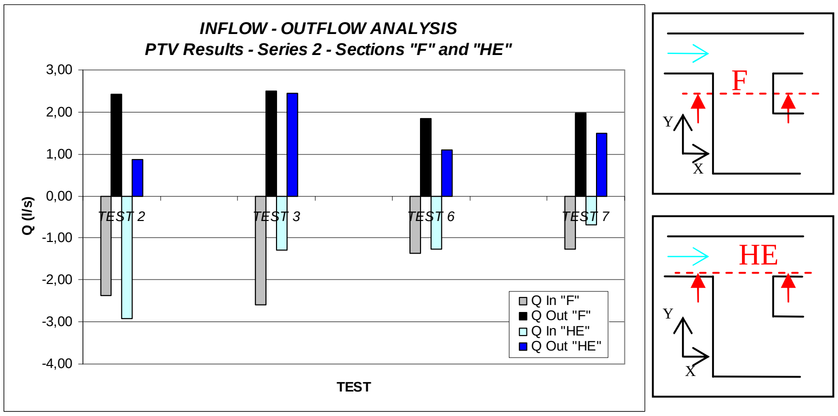

Figure 5.2.8. Series 2. Inflow and outflow rates for Sections "F" and "HE".

From Figure 5.2.8 it can be observed that Test 6 presents the lower rates than the other cases, except for the value of the inflow across section "HE", as it was describe above.The results from Test 6 do not present high asymmetry between inflow and outflow values as it can be seen in Test 3.

From these results, the configuration with six piles presents higher effects on the mean transverse velocities and the related exchange across the harbour entrance than the other cases.

5.2.1.6. Location and streamwise velocity at the centre of the mixing layer.

The same procedure described in Section 5.1.1.6 it is applied to obtain the streamwise velocity at the mixing layer and its width.

Table 5.2.3 lists the values for Tests 6 and 7, together with the reference case and Test 3, to compare the new results.

		Mixing layer centre		
CASE	X(m)	u_c (cm/s)	δ (cm)	y_c (cm)
Test 2 - Ref. Case	5.47	19.32	0.35	0.22
	5.98	19.26	0.43	0.21
	6.47	19.53	0.5	0.2
Test 3 - n =7 piles	5.47	20.02	0.50	0.47
	5.98	19.36	0.6	0.45
	6.47	18.75	0.6	0.38
Test 6 - n =6 piles	5.47	18,85	0.55	0.4
	5.98	18,18	0.55	0.38
	6.47	18,91	0.52	0.38
Test 7 - n =5 piles	5.47	19,87	0.50	0.35
	5.98	20,34	0.50	0.35
	6.47	19,34	0.55	0.30

Table 5.2.3. Series 2. Characteristics of the mixing layer.

The values of the mixing layer width in these experiments are close to the results of Test 3. No variation is present along the harbour entrance in δ values. However, experiments of Series 2 present lower y-coordinates of the mixing layer centre.

It implies that the mixing layer has the same width for all cases with the groyne at d =35 cm, but the centre moves towards the harbour basin when the number of piles decrease.

Figure 5.2.9 presents the lateral profile of the streamwise velocity along section “A” for each experiment and the mixing layer width. Each double arrow represents the mixing layer width for each case.

The most significant result from these figures is the uniformity of the profile for Test 7. In this case, the shift due to the presence of the second mixing layer is absent and displays the same distribution given by the reference case but with a larger mixing layer width.

From Tests 3 and 6 can be noted that the slope of the first part of the profile is higher in Test 6. According with the relation between the velocity gradient and the production term (see Chapter 3), Test 6 will reveal a higher term and consequently, it will imply a higher development of eddy structures along the entrance.

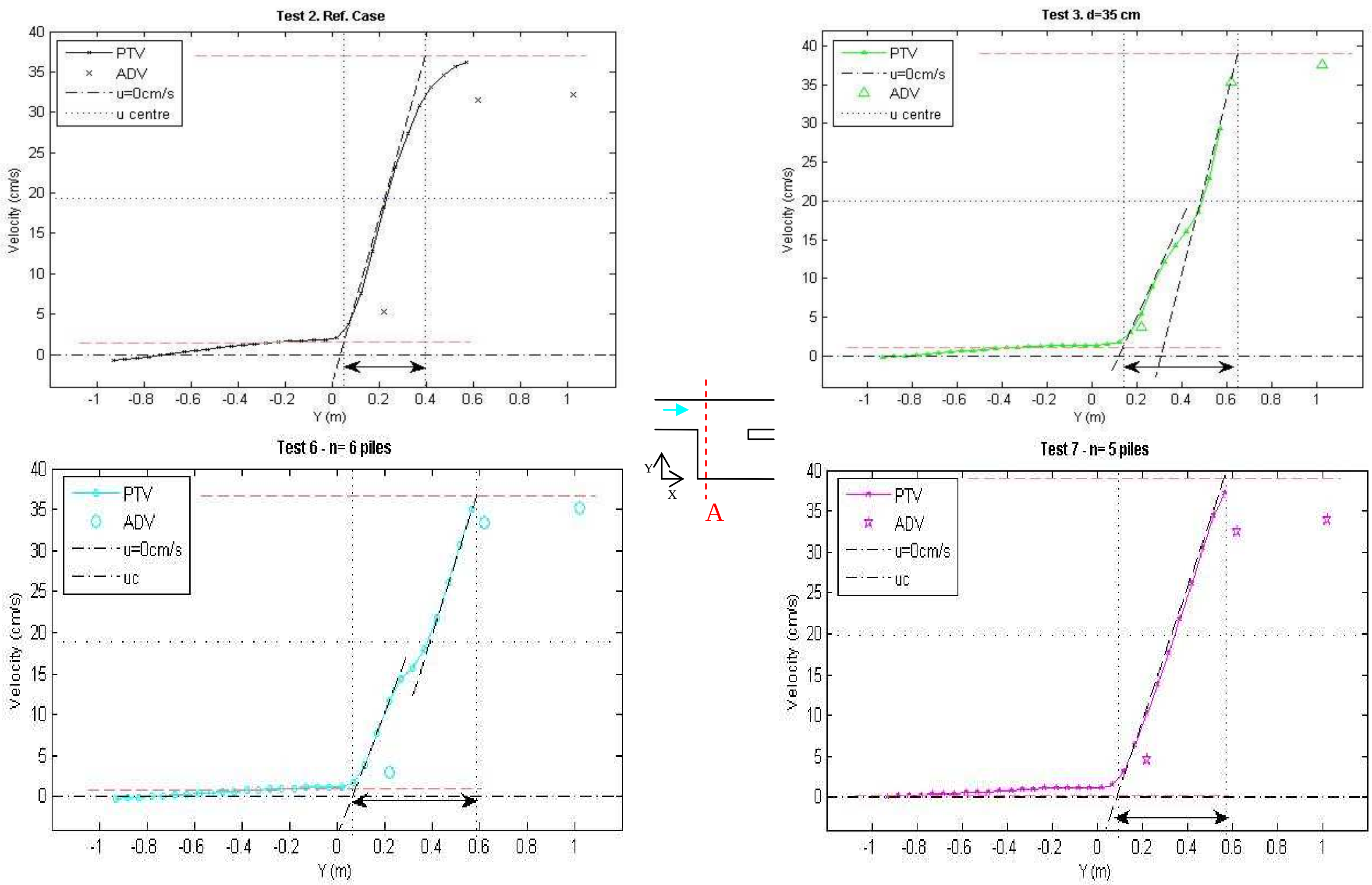

Figure 5.2.9. Series 2. Streamwise velocity profile from PTV and mixing layer width. Section A (X=5.47m).

5.2.2. Turbulence properties.

5.2.2.1. Autocorrelation analysis.

Figure 5.2.10 shows the autocorrelation functions for the transverse component in location E6 (X=6.47m and Y=-0.23m) for Test 2 (black line), Test 3 (green line), Test 6 (blue line) and Test 7 (magenta line).

As it was discussed for Series 1, Test 3 does not present the periodicity and time scales of the reference case. However, from the configurations of Series 2 can be established that the effect of the pile groyne decreases for a low number of piles and consequently the autocorrelation profile turns into the periodic shape shown in Test 2.

From these results, it can be concluded that the results obtained with six and seven piles at this locations are similar, but when the length decreases significantly, the behaviour in this point correspond with the pattern of the reference case.

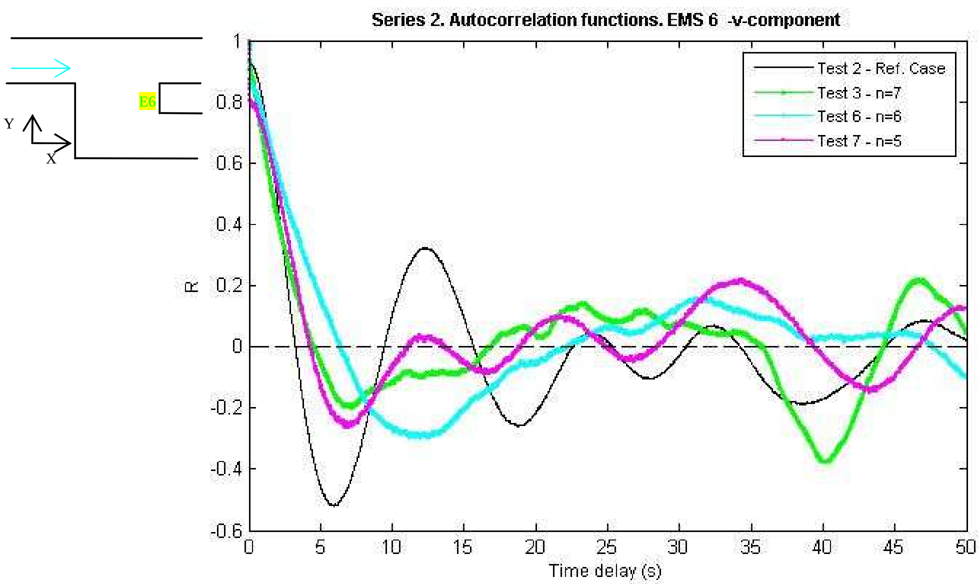

Figure 5.2.10. Series 2. Autocorrelation functions EMS 6.

Figure 5.2.11 shows the autocorrelation functions from ADV measurements in locations A4 (Y=0.22m) and A5(Y=0.62m).

Figure 5.2.12 presents the autocorrelation functions from ADV measurements in locations A1 (X=5.47m) and A1(Y=6.47m).

From these points it is shown that Test 7 has lower amplitudes in location A4 and longer time scales.

In comparison with Test 3 (n=7), both cases give longer time lengths than Test 3 and as a results, it can be concluded that a low number of piles generates larger time scales along the harbour entrance.

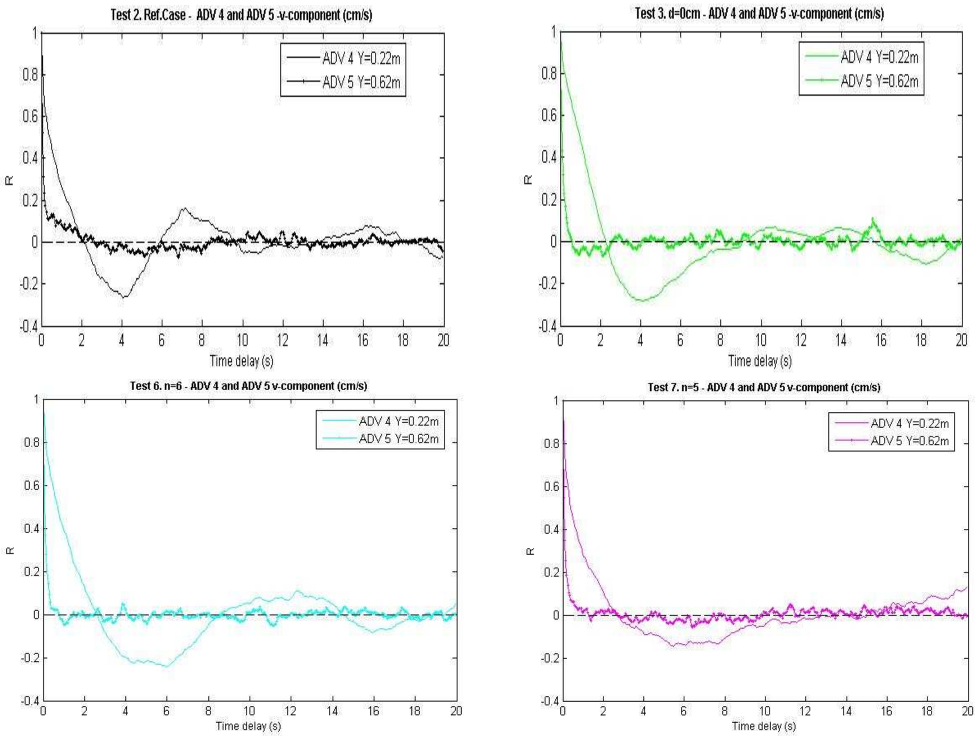

Figure 5.2.11. Series 2. Autocorrelation functions ADV 4 (5.98,0.22) and ADV 5 (5.98,0.62).

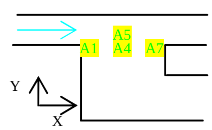

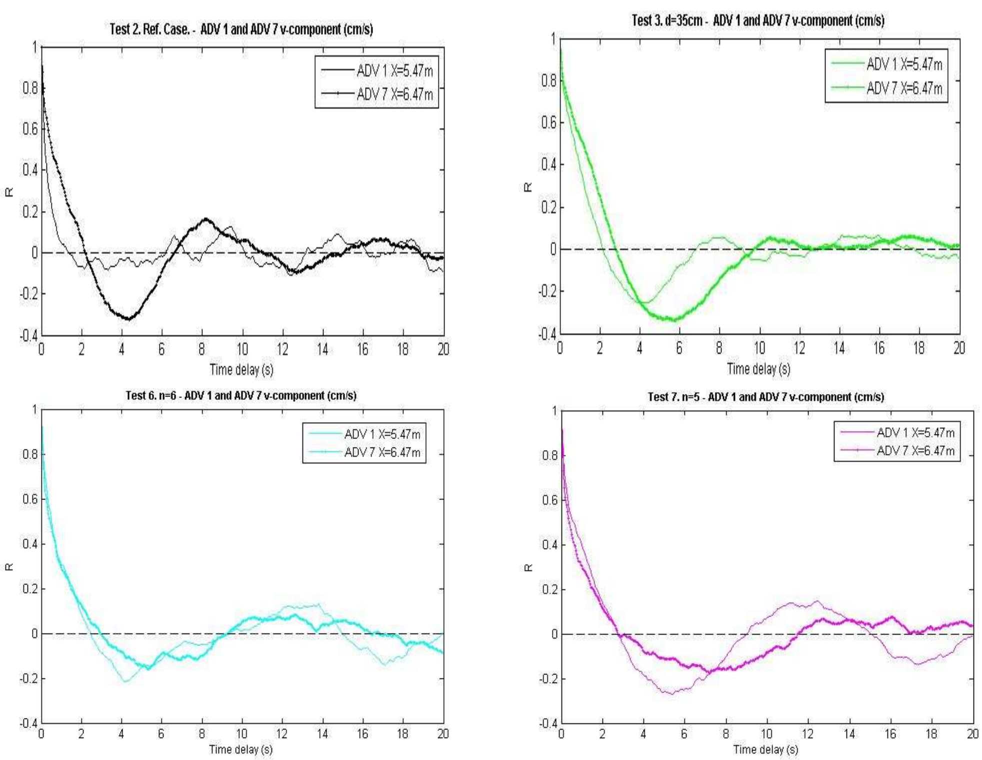

Figure 5.2.12. Series 2. Autocorrelation functions ADV 1 (5.47, 0.22) and ADV 7(6.47, 0.22).

5.2.2.2. Reynolds stresses.

As it was discussed for Series 1, Reynolds shear stresses are obtained for Tests 6 and 7 from PTV measurements. *Figure 5.2.13* presents results of Tests 2 (upper-left plot), 3, 6 and 7 (down-right plot).

A clear decrease on the Reynolds stress can be observed in Test 6 and 7, in comparison with the results of Test 3. However, a small area of positive values is observed in Test 7 that it can be attributed to the lower effect of this configuration which has a shorter length and consequently, it seems to present a weak tendency to the distribution observed in the reference case.

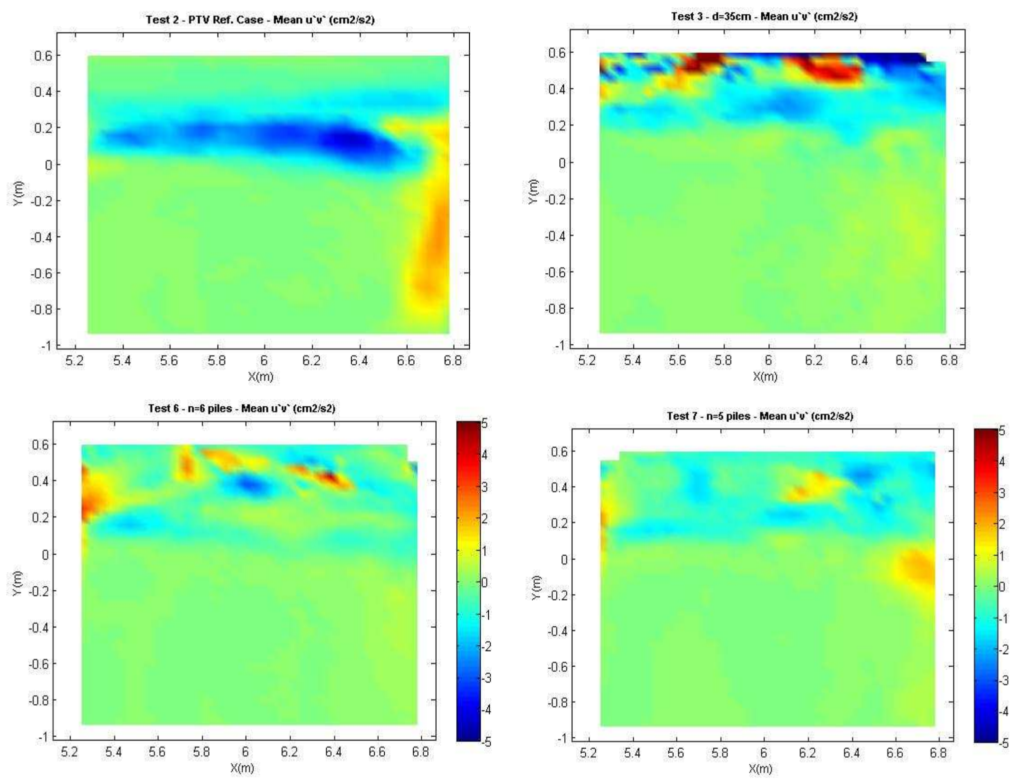

5.2.13. Series 2. Reynolds stress $\langle u'v' \rangle$ (cm²/s²).

Table 5.2.4 lists the values of u_{std} and v_{std} for all experiments at points with Y=0.22 m.

			Test 2		Test 3		Test 6		Test 7	
			Ref. Case		n=7		n=6		n=5	
Line		**X(m)**	<u'v'>	u_{std} v_{std}	<u'v'>	u_{std} v_{std}	<u'v'>	u_{std} v_{std}	<u'v'>	u_{std} v_{std}
	A1	***5.47***	-4.00	11.00	-4.00	8.00	-1.46	4.42	-3.04	7.33
G	***A4***	***5.98***	-6.00	14.00	-3.00	9.00	-1.57	4.63	-2.42	6.00
Y=0.22m	***A7***	***6.47***	-8.00	15.00	-1.00	8.00	-0.88	3.66	-2.25	7.18

Table 5.2.4. Series 2. Comparison. Reynolds stress u'v' and std. u and v-components (cm^2/s^2).

The values of $\langle u'v' \rangle$ are around 0.4 times the $u_{std}v_{std}$ at the points located along the mixing layer for the reference case.

This characteristic is present in other experiments at location A1 (near the upstream corner), but it differs in Tests 3 and 6, in which $\langle u'v' \rangle$ is lower than 0.4 times the value of $u_{std}v_{std}$.

From these results it can be concluded that Test 6 gives the lowest values along the entrance when ADV measurements are used for the analysis, which are in accordance with the results obtained from PTV data.

5.3. Data analysis for Series 3.

Finally, experiments of Series 3 are presented. In this section, the comparison will not be carried out with the reference case.

For these configurations, Test 8 (n=5piles, s =4.5 cm) will be compared with Test 7 (n=5 piles, s =3 cm) and Test 9 (n=6piles, s =2 cm) will be compared with Test 6 (n=6 piles, s =3 cm). Consequently, it will be possible to observe differences between tests with the same conditions (number of piles and location), except for the aperture between piles.

Consequently, each stage of the analysis will be developed in pairs. The first pair of experiments will show effects of using a wider hole between piles and the second, the effect of a narrow distance.

5.3.1. Mean flow.

5.3.1.1. Velocity field.

Figure 5.3.1.a shows the modified vector map of the mean velocity for Test 8. The groyne is sketched for Test 8 with dotted red lines to represent the different gap between piles. Its reference case (Test 7, s =3cm) is plotted as well.

A clear decrease in the transverse velocity neat the upstream corner is shown with respect Test 7.

Figure 5.3.1.b shows the modified vector map of the mean velocity for Test 9. In this case, the difference between tests is not perceptible from the vector maps. The Velocimetry comparison follows this subsection.

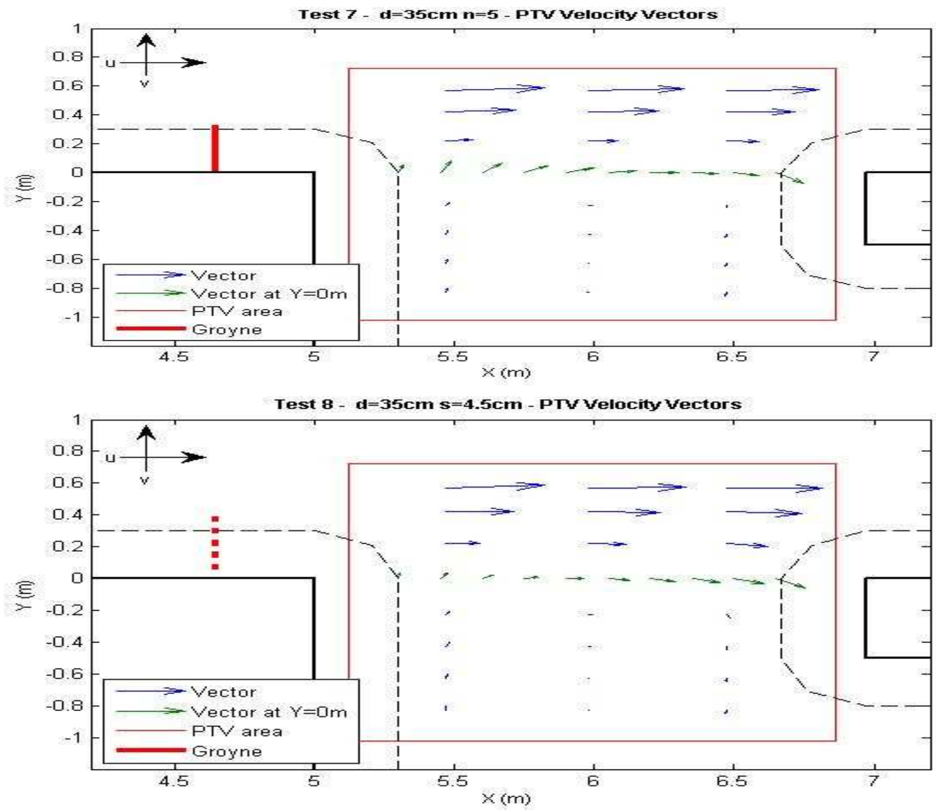

Figure 5.3.1.a. Series 3. s =4.5 cm. Velocity vectors from PTV data.

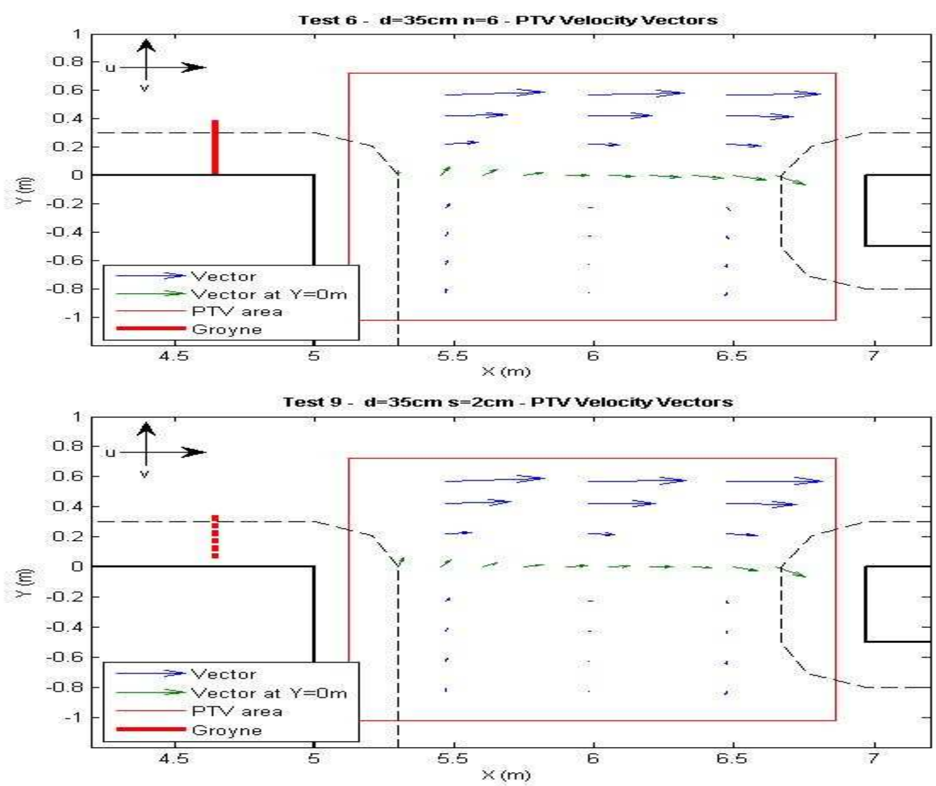

Figure 5.3.1.b. Series 3. s =2cm. Velocity vectors from PTV data.

5.3.1.2. Velocimetry comparison ADV versus PTV.

The results are listed in *Table 5.3.1.* The first aspect to discuss it is the effect on the river stream. From Test 8 it is seen that the velocities at Y=0.62 m are lower than the case with s =3 cm.

On the other hand, Test 9 gives higher velocities along this line. It suggests that a narrow gap between piles generates higher velocities at the river stream due to the reduction of the cross sectional area near the right bank where the groyne is located.

However, the effects along the mixing layer (Y=0.22m) are opposite. Test 8 (s =4.5cm) shows higher values along the harbour entrance. It means that a larger distance between piles creates higher velocities near the entrance.

As a consequence, these results show that the decrease of the distance between piles is an advantage to reduce the velocities near the entrance but it presents the drawback of the generation of higher velocities at the river stream

Test 7 – n=5 piles s=3cm

POINT	Coordinates		ADV	PTV	
	X(m)	Y(m)	$\sqrt{(u^2+v^2)}$(cm/s)		Δ (cm/s)
A1	5.47	0.22	4.58	10.31	5.73
A2	5.47	0.62	32.48	37.21	4.74
A4	5.98	0.22	6.21	10.94	4.73
A5	5.98	0.62	31.03	36.48	5.45
A7	6.47	0.22	7.50	12.85	5.34
A8	6.47	0.62	31.45	35.40	3.95

Test 6 – n=6 piles s=3cm

POINT	Coordinates		ADV	PTV	
	X(m)	Y(m)	$\sqrt{(u^2+v^2)}$(cm/s)		Δ (cm/s)
A1	5.47	0.22	3.08	11.71	8.63
A2	5.47	0.62	33.82	35.04	1.22
A4	5.98	0.22	5.47	11.08	5.61
A5	5.98	0.62	33.46	34.01	0.55
A7	6.47	0.22	5.94	12.26	6.32
A8	6.47	0.62	33.21	33.98	0.77

Test 8 –n=5 s=4.5cm

POINT	Coordinates		ADV	PTV	
	X(m)	Y(m)	$\sqrt{(u^2+v^2)}$(cm/s)		Δ (cm/s)
A1	5.47	0.22	3.80	12.18	8.38
A2	5.47	0.62	32.34	34.60	2.26
A4	5.98	0.22	6.49	14.63	8.14
A5	5.98	0.62	31.86	34.18	2.32
A7	6.47	0.22	8.17	14.71	6.54
A8	6.47	0.62	31.39	34.18	2.80

Test 9 – n=6 s=2cm

POINT	Coordinates		ADV	PTV	
	X(m)	Y(m)	$\sqrt{(u^2+v^2)}$(cm/s)		Δ (cm/s)
A1	5.47	0.22	2.42	9.33	6.90
A2	5.47	0.62	33.83	36.93	3.11
A4	5.98	0.22	4.47	9.76	5.29
A5	5.98	0.62	33.51	36.90	3.39
A7	6.47	0.22	5.51	11.99	6.47
A8	6.47	0.62	33.05	36.04	2.98

Table 5.3.1. Series 3. Comparison of flow velocities from ADV and PTV.

5.3.1.3. Streamwise velocity.

- Lateral profiles.

Figures 5.3.2 and *5.3.3* show the lateral profiles of the streamwise velocity in sections A (X=5.47m) and B(X=5.98m).

From the first figure a clear difference between Tests 7 (s =3) and Test 8 (s =4.5) is shown. The larger gap presents the deviation along the profile for the presence of two mixing layers. This aspect is not found with the narrow gap.

It can be concluded that this shift along the profile appears for cases with a high number of piles (as in Test 6) or with a wider distance between piles (due to the increase of the total length of the array).

It is identified that the groyne does not create this effect when the length of the groyne is equal to the width of the embankment (as in Test 7 (L=27m) and Test 9 (L=28m)).

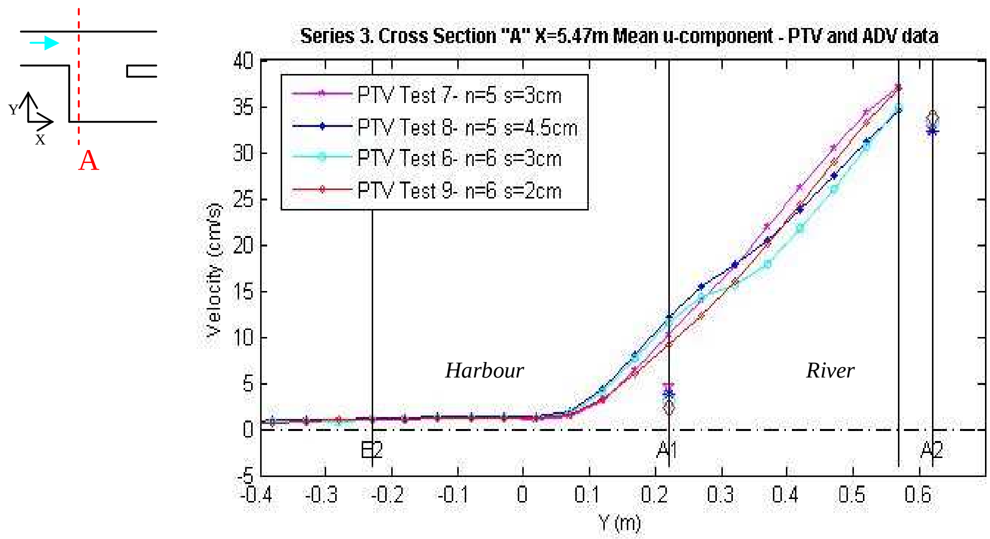

Figure 5.3.2. Series 3. Lateral profile mean u-component. Section A. (X=5.47m).

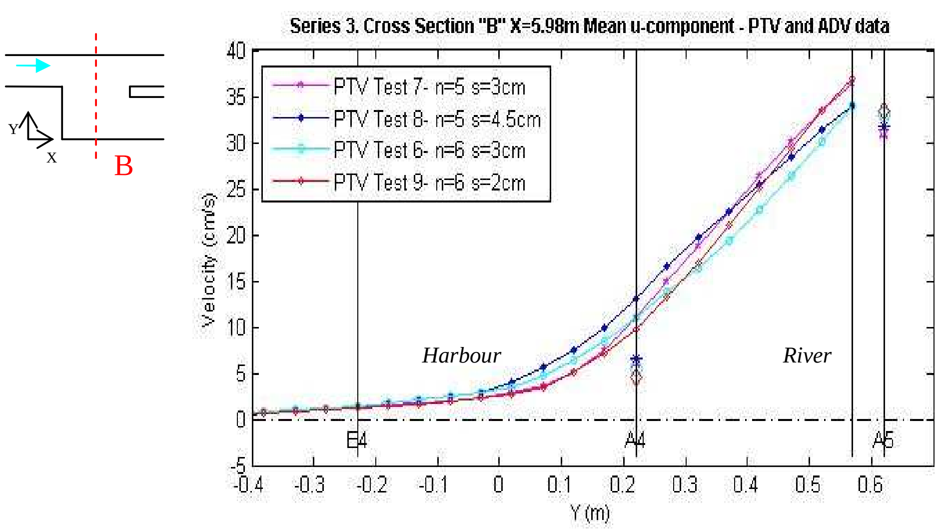

Figure 5.3.3. Series 3. Lateral profile mean u-component. Section B. (X=5.98m).

- Standard deviation. Streamwise velocity.

From *Figure 5.3.4.a.* a similar pattern between both cases (Test 7 and Test 8) is found, but a higher trend towards the downstream corner of the entrance is present for the wider case.

It can be attributed to the fact that the flow passes across the piles in Test 8 with a lower disturbance, and consequently, for this case, the flow follows similar paths near the embankment than in the reference case.

From *Figure 5.3.4.b.* an area with high u_{std} values is found in Test 9 which can be associated to a higher generation of eddy structures due to the larger which develops downstream the edge.

As it can be expected, this effect is a result of a higher strength that the groyne is producing against the flow.

5.3.1.4. Transverse velocity.

- Lateral profiles.

For this series, sections “A” and “C” are considered, because no significant results were found for the previous series from section B.

From *Figure 5.3.5* it is remarkable that Test 8 (s =4.5 cm) shows the highest differences with respect to the rest of experiments. This configuration presents the highest velocity values at the downstream side and the lowest results at the upstream part (section A), as a result, a higher asymmetry is found.

No differences are found between Test 6 (n=6 piles) and Test 9 (s =2 cm). For this reason, there is no apparent effect on the distribution of the mean transverse velocity when the distance between piles is reduced.

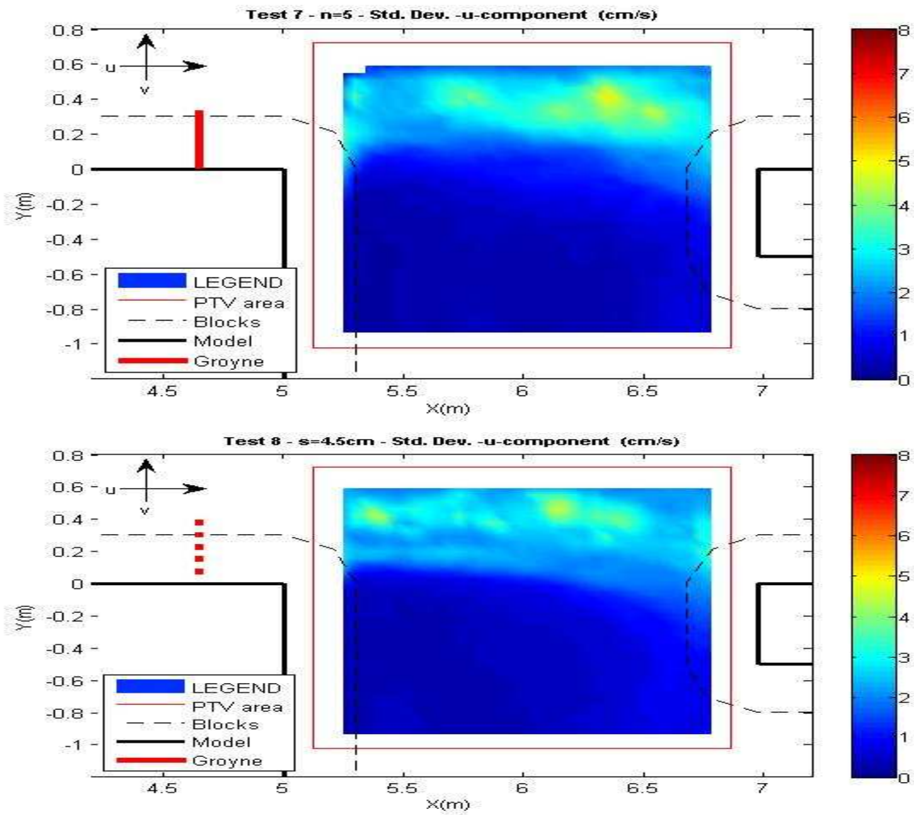

Figure 5.3.4.a. Series 3. s=4.5 cm. Std. Deviation u-component from PTV data (cm/s).

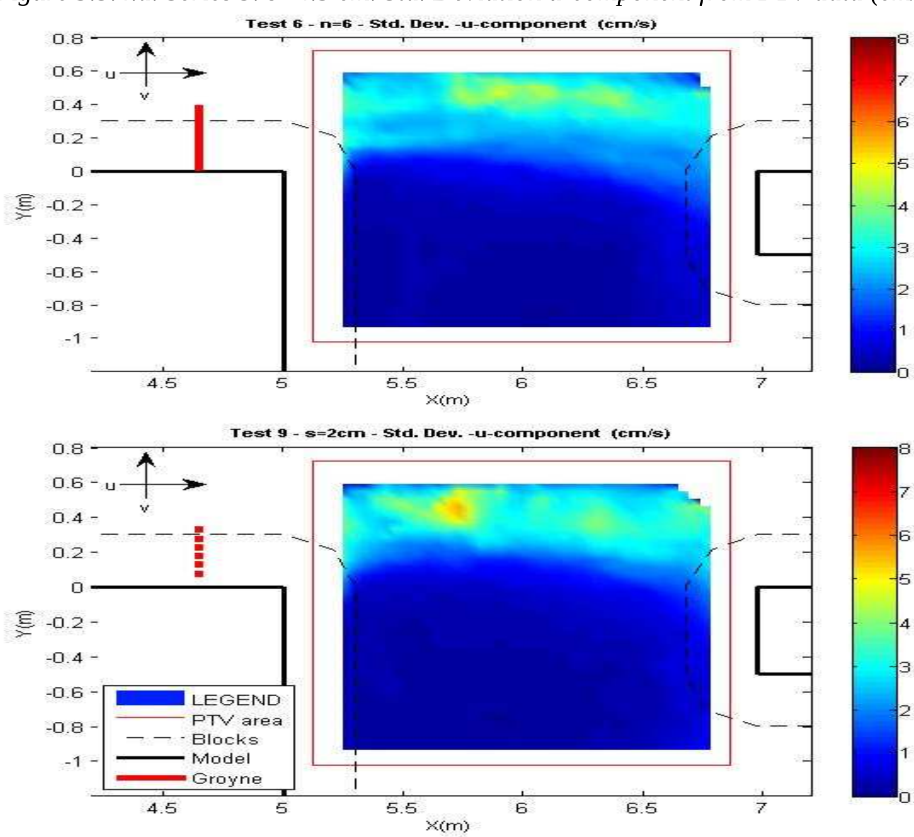

Figure 5.3.4.b. Series 3. s=2cm. Std. Deviation u-component from PTV data (cm/s).

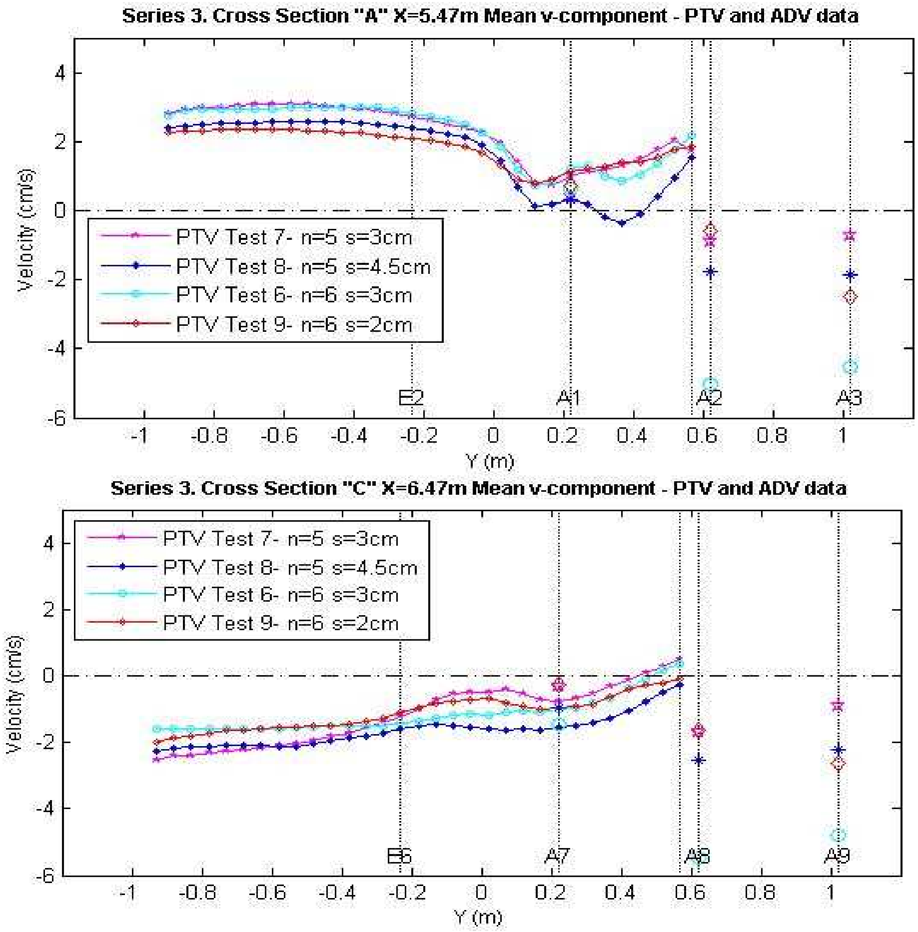

Figure 5.3.5. Series 3. Mean v-component.
Sections A(X=5.47m), B(X=5.98m) and C(X=6.47m).

- *Standard deviation. Transverse velocity.*

Figure 5.3.6. a. and *Figure 5.3.6.b.* present the results of the standard deviation v_{std} for Series 3.

As it has been seen for the streamwise velocity, the high area for the case with the wider gap shifts towards the basin as it was contemplated for the reference case without groyne.

Together with the results of the streamwise velocity, it can be considered that the configuration with split piles is less effective than the other cases in relation with the distribution of the mean and standard deviation values over the harbour entrance area.

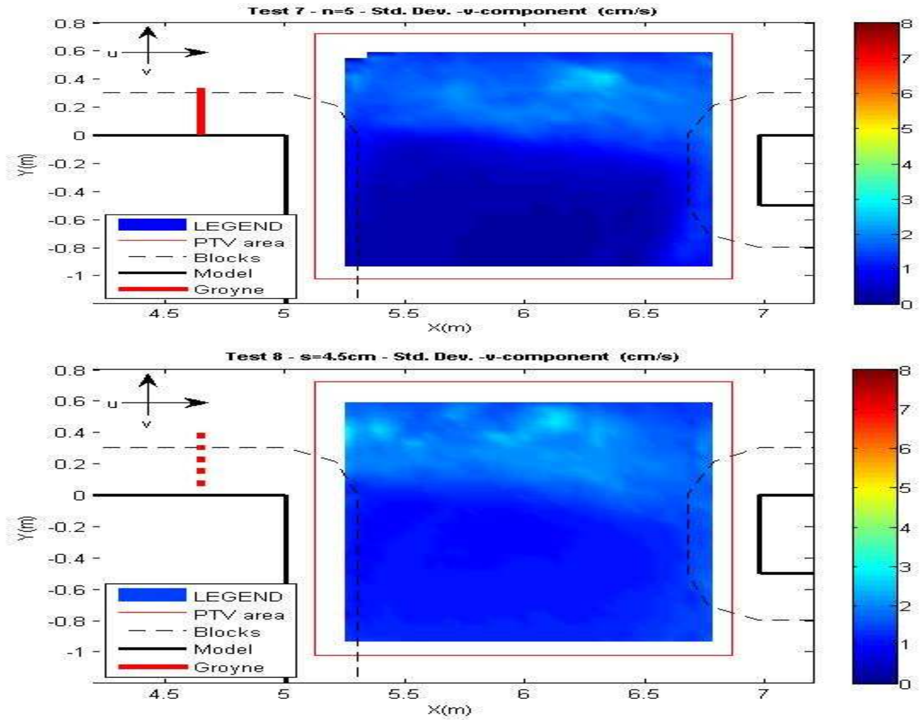

Figure 5.3.6.a. Series 3. s=2 cm. Std. Deviation v-component from PTV data (cm/s).

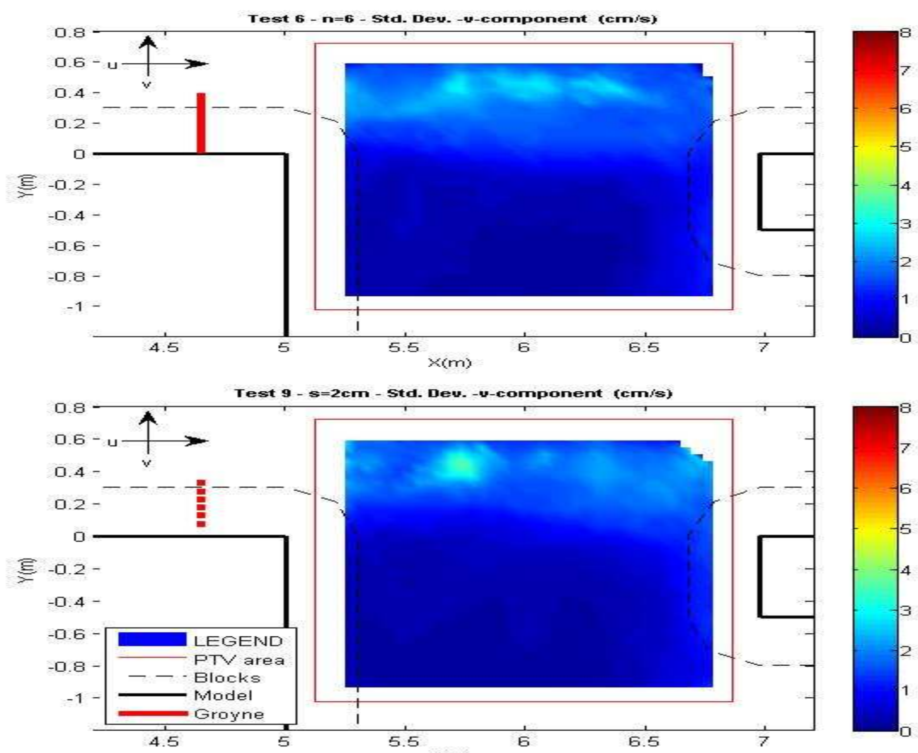

Figure 5.3.6.b. Series 3. s=2 cm. Std. Deviation v-component from PTV data (cm/s).

5.3.1.5. Estimation of flow exchange through the harbour entrance.

Figure 5.3.7 presents the lateral profile along Section "F" (Y=-0.23m) of the mean transverse velocities obtained from PTV data. The results of the inflow and outflow rates are listed in *Table 5.3.2*. and percentages of reduction are given in *Table 5.3.2.b.*

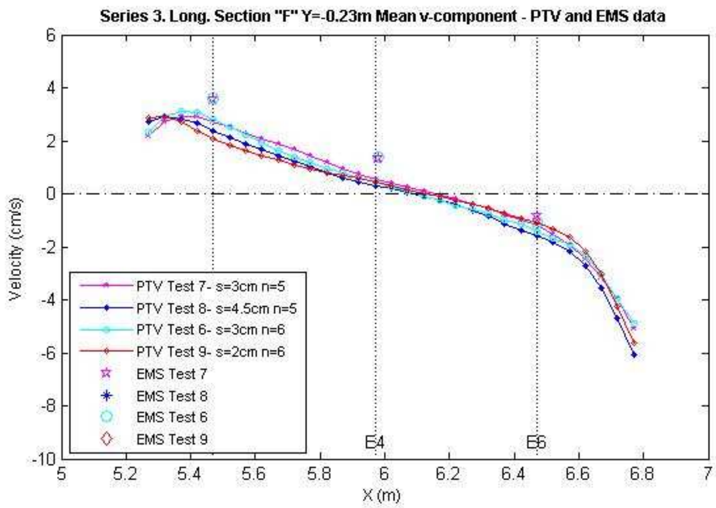

Figure 5.3.7. Series 3. Lateral profile of mean v-component at Section "F"(Y=-0.23m).

	Section F		***Section HE***	
	Q_{in} (l/s)	***Q_{out} (l/s)***	***Q_{in} (l/s)***	***Q_{out} (l/s)***
Test 7- n=5 s=3cm	-1.26	1.96	-0.70	1.50
Test 8- n=5 s=4.5cm	-1.57	1.64	-1.72	0.96
Test 6- n=6 s=3cm	-1.35	1.85	-1.26	1.11
Test 9- n=6 s=2cm	-1.22	1.54	-0.81	0.94

Table 5.3.2.a. Series 3. Inflow and outflow rates for sections "F" and "HE".

	Section F		***Section HE***	
	% Q_{in}	***% Q_{out}***	***% Q_{in}***	***% Q_{out}***
Test 7- n=5 s=3cm	-46.51	-19.41	-76.13	75.14
Test 8- n=5 s=4.5cm	-33.35	-32.61	-41.27	11.26
Test 6- n=6 s=3cm	-42.66	-24.16	-57.15	28.71
Test 9- n=6 s=2cm	-48.49	-36.59	-72.26	9.57

Table 5.3.2.b. Series 3. Reduction rates of inflow and outflow results. Sections "F" and "HE".

From these results, a higher inflow rate is obtained in both sections in Test 8. However, Test 9 gives lower inflow rates and lower outflow rates than Test 6.

The asymmetry in Test 7 is not present in Test 8. For this experiment, rates at Section F show equal values of inflow and outflow results.

Figure 5.3.8 shows the inflow and outflow rates for Series 3 along Sections "F" and "HE".

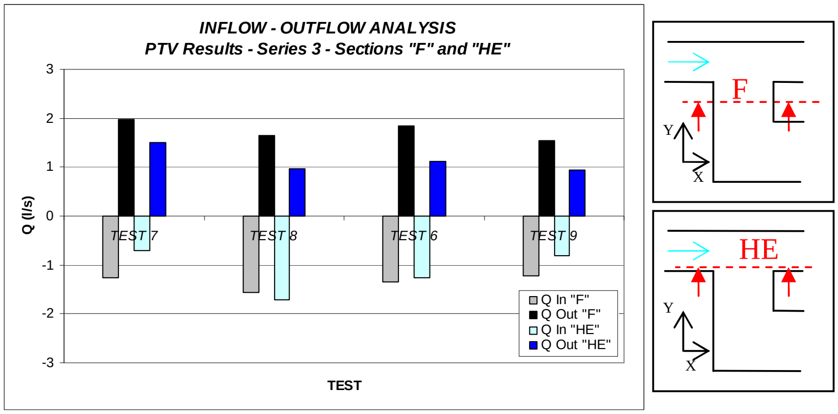

Figure 5.3.8. Series 3. Inflow and outflow rates for Sections "F" and "HE".

From Figure 5.3.8 it can be drawn that Test 6 presents the lowest rates than the other cases, except for the value of the inflow across section "HE".

The results from Test 6 do not present high asymmetry between inflow and outflow values as it can be seen in Test 7.

From these results, the configurations with six piles (Tests 6 and 9) present higher effects on the mean transverse velocities and the related exchange across the harbour entrance than the other cases.

The configuration with s =2cm is the best configuration to reduce the inflow and outflow rates through the harbour entrance.

5.3.1.6. Location and streamwise velocity at the centre of the mixing layer.

Table 5.3.3 lists the values for Tests 8 and 9, together with the Tests 6 and 7, to compare the new results with the previous configurations of Series 2.

		Mixing layer centre		
CASE	X(m)	u_c (cm/s)	δ (cm)	y_c (cm)
Test 7 - n=5 s=3cm	5.47	19.87	0.50	0.35
	5.98	20.34	0.50	0.35
	6.47	19.34	0.55	0.30
Test 8 - n=5 s=4.5cm	5.47	18.81	0.56	0.35
	5.98	19.48	0.60	0.35
	6.47	18.77	0.65	0.25
Test 6 - n=6 s=3cm	5.47	18.85	0.55	0.4
	5.98	18.18	0.55	0.38
	6.47	18.91	0.52	0.38
Test 9 - n=6 s=2cm	5.47	18.82	0.45	0.35
	5.98	18.82	0.48	0.33
	6.47	18.46	0.55	0.32

Table 5.3.3. Series 3. Characteristics of the mixing layer.

From the first pair of experiments, larger values of the mixing layer width are obtained for s =4.5 cm. It can be attributed to the larger length of the pile array. However, the y-coordinate of the centre is similar in each section to Test 7.

However, Test 9 presents lower values of the mixing layer width in comparison with Test 6. It implies that a narrow distance between piles produces a decrease of the mixing layer width, but the y-coordinates are close to the harbour entrance. This reduction in the y-coordinate can be attributed to the fact that the edge of the array is located near the embankment (L=28m instead of L=33m in Test 6).

Figure 5.3.9 presents the lateral profile of the streamwise velocity along section “A” for each experiment and the mixing layer width. Each double arrow represents the mixing layer width for each case.

The most significant result from these figures is the presence of two mixing layers in Test 8. The shift along the lateral profile is present for this configuration. However, from Test 9 is obtained that this effect disappears for s =2 cm.

From these results can be concluded that the total length of the pile array plays an important rule in the velocity gradient of the streamwise velocity and, consequently, on the production term.

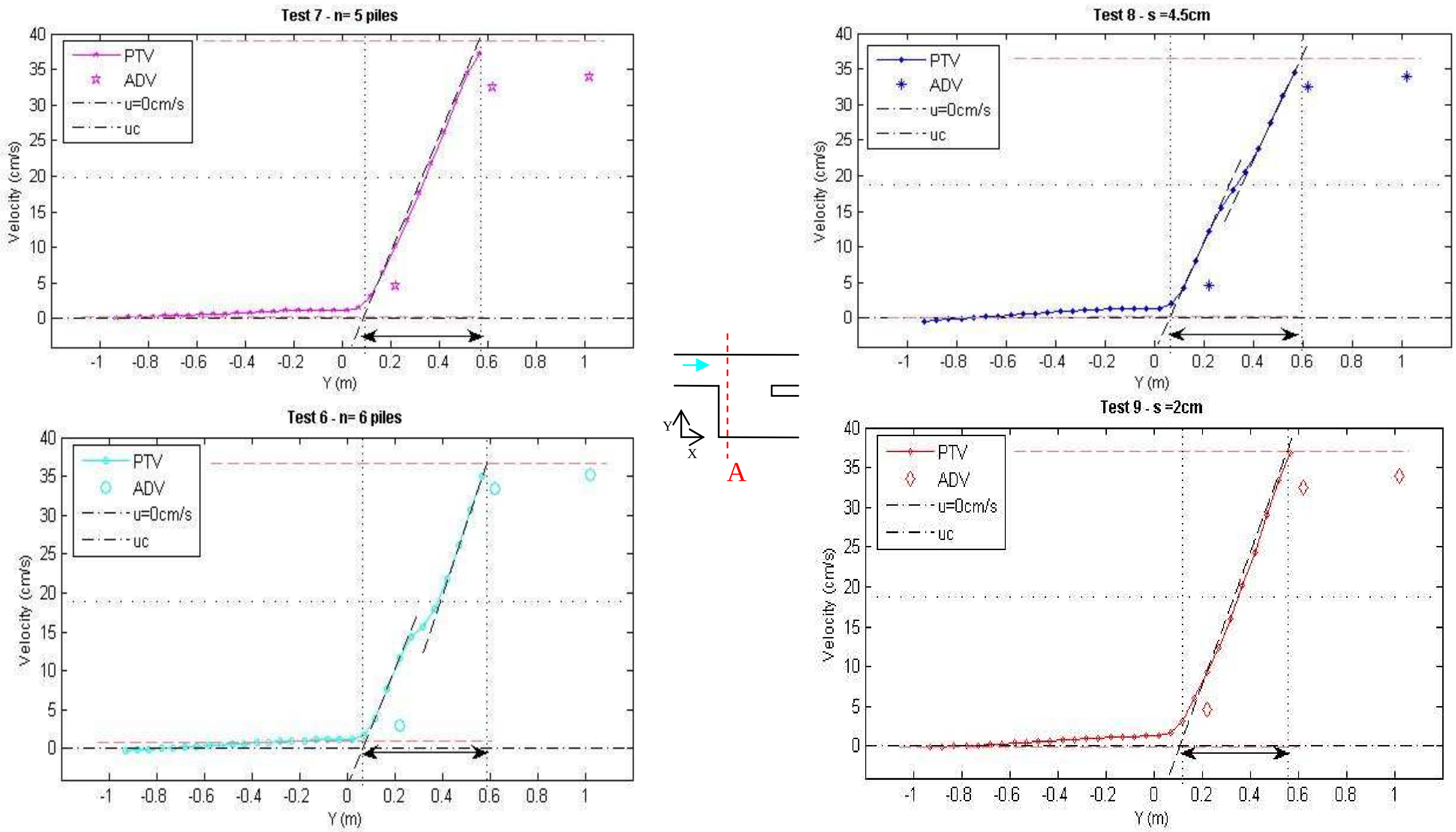

Figure 5.3.9. Series 3. Streamwise velocity profile from PTV and mixing layer width. Section A (X=5.47m).

5.3.2. Turbulence properties.

5.3.2.1. Autocorrelation analysis.

Figure 5.3.10 shows the autocorrelation functions for the transverse component in location E6 (X=6.47m and Y=-0.23m) for Test 7 (magenta line), Test 8 (blue line), Test 6 (cyan line) and Test 9 (red line).

If cases with five piles are compared (Tests 7 and 8), no differences in time scales and periodicity are found. However, Test 8 (s =4.5cm) presents higher amplitudes and the range through negative correlation values is larger than in Test 7.

From Test 9, it is significant that all correlation values are close to zero and some periodicity which it is not present in Test 6. This aspect reveals that both experiments of Series 3 are close to the reference case without groyne. On one hand, Test 8 has larger space between piles and then it generates lower effect on the flow. On the other hand, Test 9 presents a lower total length and it implies a higher proximity of the mixing layer into the harbour entrance.

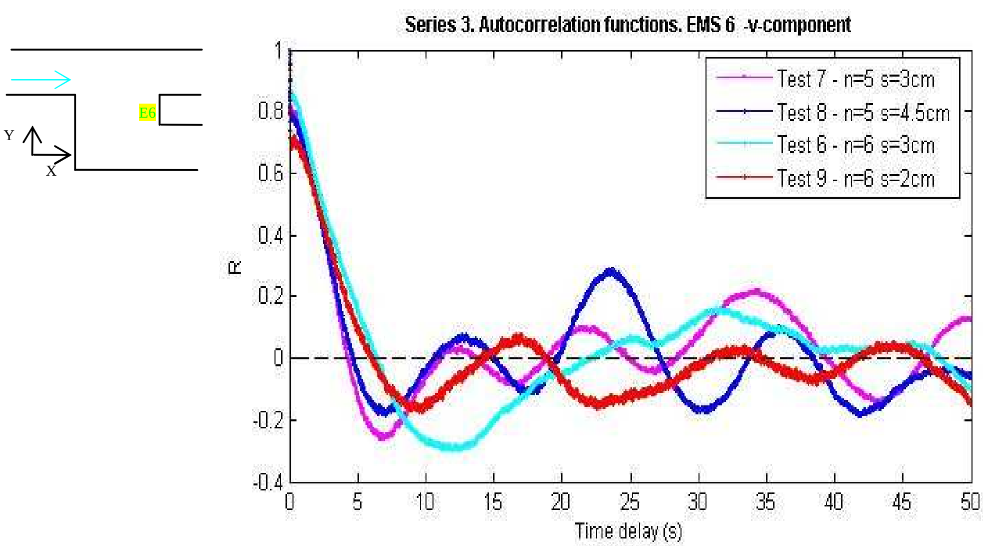

Figure 5.3.10. Series 3. Autocorrelation functions EMS 6.

Figure 5.3.11 shows the autocorrelation functions from ADV measurements in locations A4 (Y=0.22m) and A5(Y=0.62m). *Figure 5.3.12* presents the autocorrelation functions from ADV measurements in locations A1 (X=5.47m) and A1(Y=6.47m).

From the first set of figures, it is clear the difference between Tests 7 and 8. Test 8 presents a clear time length of 12 seconds and high periodicity, which it is not obtained with other cases.

From the second set, high similarity is found between autocorrelation functions A1 and A7 in Test 8.

These results confirm that a space between piles of 1.5 times the width of each pile gives similar results than the case without structure upstream the entrance.

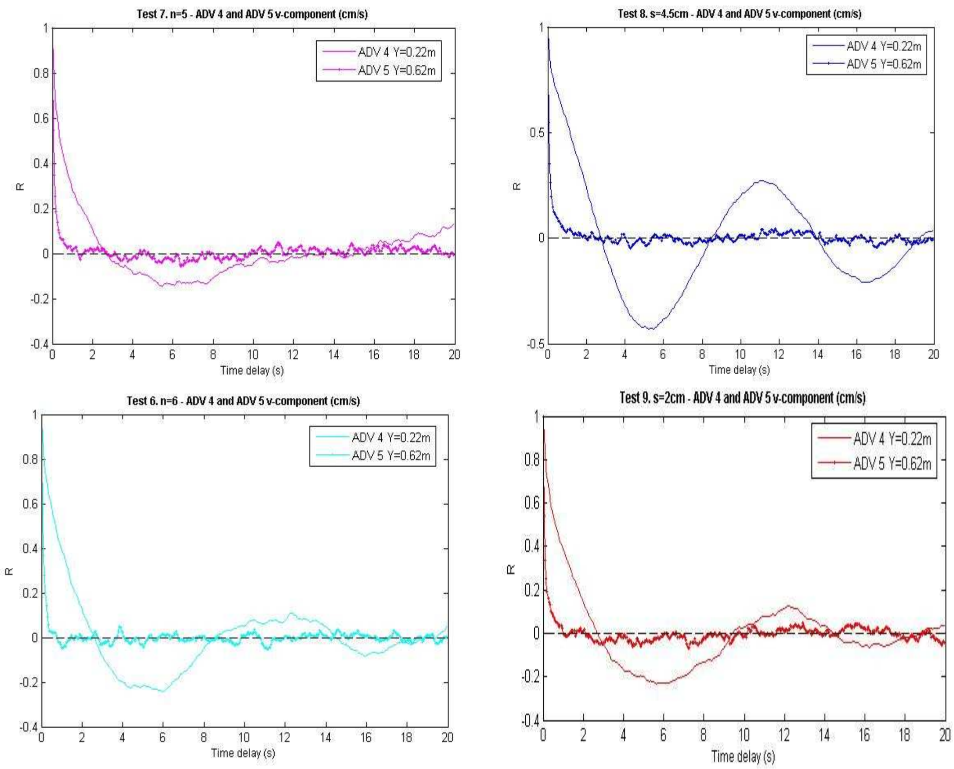

Figure 5.3.11. Series 3. Autocorrelation functions ADV 4 (5.98, 0.22) and ADV 5 (5.98,0.62).

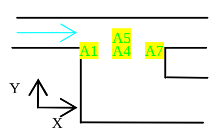

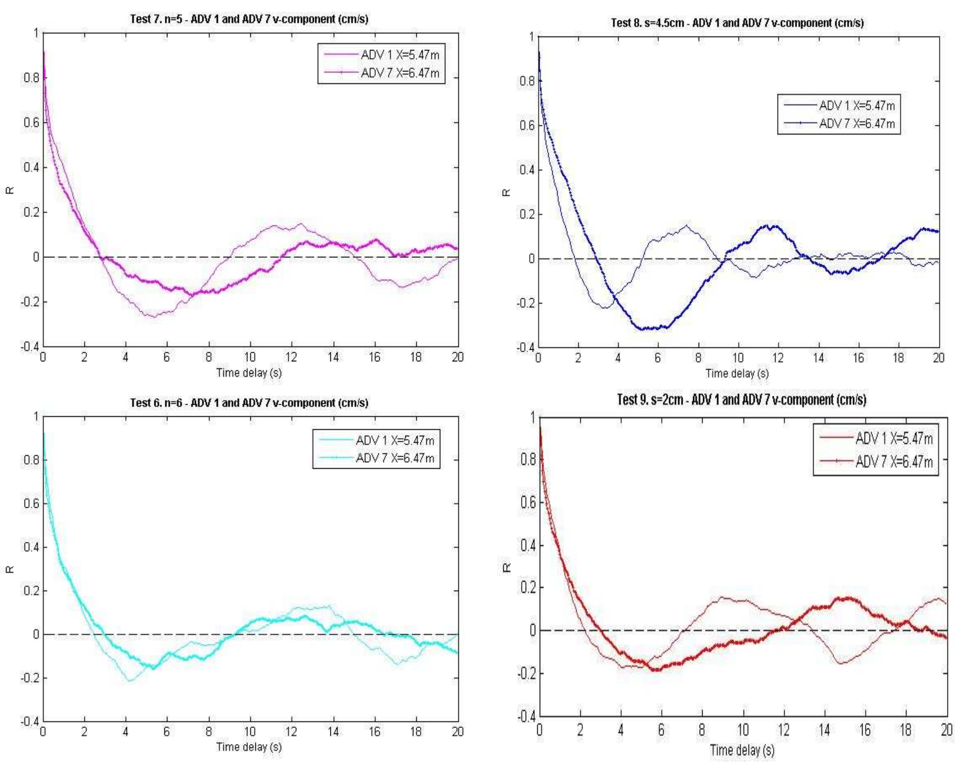

Figure 5.3.12. Series 3. Autocorrelation functions ADV 1 (5.47, 0.22) and ADV 7(6.47, 0.22).

5.3.2.2. Reynolds stresses.

Figure 5.3.13 presents results of Series 3, in comparison with Tests 6 and 7.

The first figures compare the case with five piles and a wider distance between piles (Test 8). From these results can be noted that the experiment of Series 3 presents higher stresses due to the larger distance between piles.

From figure 5.3.13.b. it can be observed that Test 9 (s =2cm) shows an area of high negative stresses at the upper-right corner of the PTV area. These results are not present in the other cases, but it can be attributed to the absence of results at the river stream and therefore, it is possible that these values are present at other locations far from the harbour entrance in downstream or upstream direction, but they cannot be perceived by the camera.

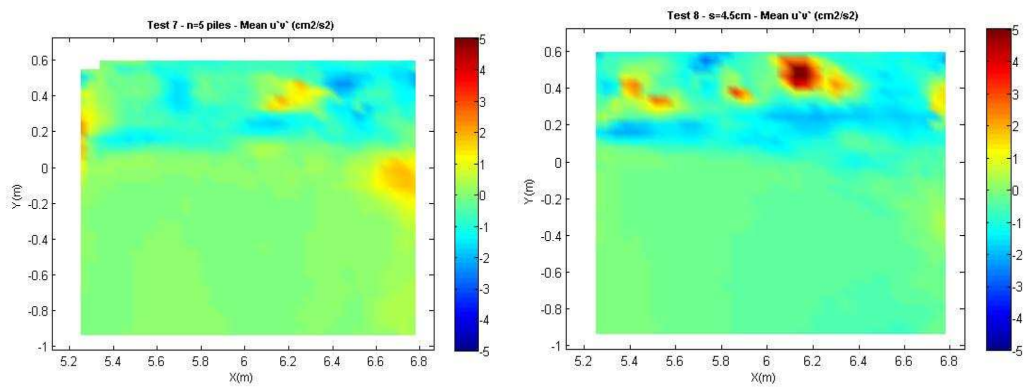

5.3.13.a. Series 3. Tests 7 and 8. Reynolds stress $\langle u'v' \rangle$ (cm^2/s^2).

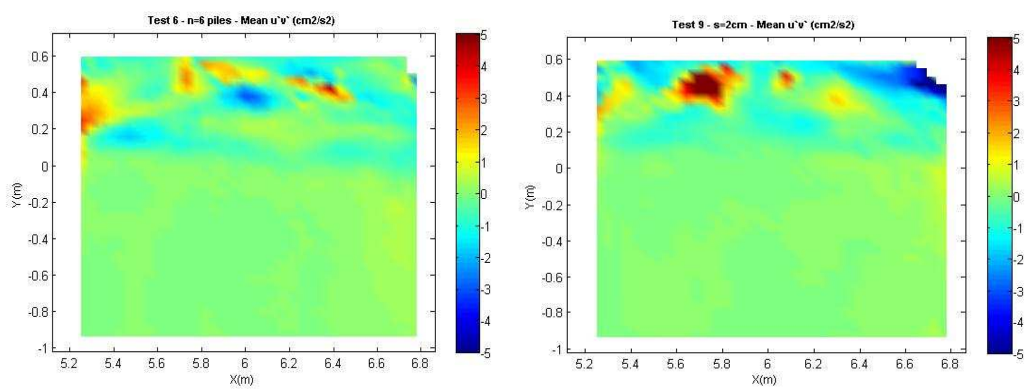

5.3.13.b. Series 3. Tests 6 and 9. Reynolds stress $\langle u'v' \rangle$ (cm^2/s^2).

If Tests 8 and 9 are compared, it is clear that lower stresses are obtained for the experiment with the narrow space between piles. Consequently, these results confirm that the configuration with s larger than the width of the piles does not improve the effect of the groyne in relation with the reduction of the production term.

Table 5.3.4 lists the values of u_{std} and v_{std} for all experiments at points with Y=0.22 m.

From the ADV measurements, lower values of the Reynolds stresses are obtained for Test 8, which implies an opposite result in comparison with the previous plots, where Test 7 appears to be a more suitable configuration.

			Test 7		Test 8		Test 6		Test 9	
			n=5 s=3cm		n=5 s=4.5cm		n=6 s=3cm		n=6 s=2cm	
Line		**X(m)**	**<u'v'>**	**u_{std} v_{std}**	**<u'v'>**	**u_{std} v_{std}**	**<u'v'>**	**u_{std} v_{std}**	**<u'v'>**	**u_{std} v_{std}**
	A1	***5.47***	-3.04	7.33	-2.04	6.16	-1.46	4.42	-1.63	3.87
G	***A4***	***5.98***	-2.42	6.00	-2.32	5.97	-1.57	4.63	-1.01	3.90
Y=0.22m	***A7***	***6.47***	-2.25	7.18	-1.60	5.91	-0.88	3.66	-2.12	6.80

Table 5.3.4. Series 3. Comparison. Reynolds stress u’v’ and std. u and v-components (cm^2/s^2).

In relation to Test 9, the result at location A7 agrees with the high values which have been observed in Figure 5.3.13.b.

5.4. Summary Data Analysis.

From the data analysis of the previous three series, several conclusions can be drawn:

- The mean velocity field for all experiments does not present high differences within the harbour basin. However, significant differences were found along the harbour entrance in relation with the velocity gradient and the streamwise profile from different cross sections at the entrance. The resulting shift on the lateral profile due to the presence of two mixing layers is more evident in cases with large number of piles and higher proximity to the upstream corner.

- From the standard deviation analyses for both velocity components, it has been observed that the high standard deviation area shifts towards the river stream for cases with a longer groyne length and a proximal location from the entrance. It was observed that the configuration with a wider gap between piles does not improve the results of the regular case (s =3cm).

- A decrease on the inflow and outflow rates through the harbour entrance obtained from PTV data is shown for all cases with groyne in comparison with the reference case. Test 9 (s =2cm) presents the lowest reduction rates for both values. Consequently, it can be concluded that a narrow space between piles generates lower mean transverse velocities along the harbour entrance and lower exchange rates.

- The experimental results indicate that the mixing layer centre is shifted towards the river stream for all cases, but the deviation towards the stream is more significant for Tests 4 and 3. It implies that the groyne located near the entrance is more effective than the other cases with lower lengths or other configurations.

- The different configurations for the groyne from all experiments have appreciable consequences on the downstream development of the mixing layer width. The mixing layer width is two times the value of the reference case at X=5.47m for Test 4. This configuration (groyne at d=0 cm) presents the wider mixing layer along the entrance and the furthest y-coordinates from the harbour basin.

- Autocorrelation analyses of the transverse fluctuations calculated from EMS and ADV measurements for all experiments of Series 1, 2 and 3 show that Test 5 (groyne at d=70 cm) and Test 8 (s =4.5 cm) present the most relevant differences with respect the other experiments. For theses experiments a high periodicity is found and the time scales are reduced in comparison with the reference case and other configurations. For the rest of the experiments, a shift to larger length-scales is also visible in autocorrelation distributions. The presence of the groyne acts as a large-scale disturber, which pushes the present coherent structures to larger length-scales.

- The Reynolds shear stresses are always higher in the reference experiment and the lower values are obtained from Tests 6 and 9, which are located 35 cm upstream the entrance, but they present different space between piles (s). The Reynolds stresses can be considered as an identifier of a different downstream evolution of the large horizontal vortices for different configurations of the groyne.

Different results are obtained from the configurations of the groyne depending on the aspect which is considered in each stage of the analysis.

In general, a higher effect on the turbulence properties and the mean flow has been observed for configurations located near the upstream corner and with a larger number of piles. However, in some circumstances, the configurations located further from the entrance (Test 5) has presented similar results with respect the other cases, but with the advantage of reducing the high disturbances near the entrance.

In relation with the separation between piles, it was found that a distance larger than the width of each pile does not provide improved results. From the narrow configuration can be concluded that the differences observed for this geometry are favourable in relation with the inflow/outflow rates, but it does not give better results for other stages of the analysis. However, it can be attributed to the reduced length that this groyne presents. Similarities between tests with the same groyne length but with different number of piles and space between them have been found.

To end this chapter, it is concluded that a groyne with a spacing between piles around 2/3 of the width and a total length of the sheet (L) according to Test 6, which ranges from Y=0.06m to Y=0.39m (of a total river width of 1.20m), located at a distance d~=L upstream the entrance seems to be the best configuration to reduce the exchange in the present model.

More research has to be developed to determine the best configuration for groynes close to the entrance or further from the case which has been studied in this thesis (d=35 cm) in order to establish the effect of changing the total length or the gap between piles when the array is located in different positions.

CHAPTER 6.

NUMERICAL MODELLING.

6.1. Introduction.

The harbour scale model of this study has been performed to provide a data set in order to verify the applicability of a two-dimensional (2D) numerical model for the simulation of the velocity field developed downstream a groyne structure located near the harbour entrance.

The aim of this section is to determine the accuracy of the numerical model *FinLab* on the resolution of mixing layer flows when a pile groyne is implemented in the model.

FinLab is in principle a fully 3D numerical model for the computation of shallow water flow and transport processes in rivers and coastal waters created by R.J. Labeur at Svasek Hydraulics and further developed at the TU Delft.

In this study the 2D-mode is applied. The numerical basis of *FinLab* is the finite element method.

6.2. Theoretical background.

6.2.1. Shallow Water Equations.

The Shallow Water Equations (SWE) result when simplifying the Navier-Stokes equations using the following assumptions *(Vreugdenhil, 1994)* for large scale motion: inviscid and hydrostatic flow of an incompressible homogeneous fluid whose vertical extent is small compared to the horizontal size of the domain.

In fact, the equations are integrated over the depth and, therefore, the resulting flow description is two-dimensional. The derivation given below is based on *Vreugdenhil (1994).*

6.2.1.1. Three-dimensional shallow-water equations.

Navier-Stokes equations

The Navier-Stokes equations were introduced in Chapter 3 and describe conservation of mass and momentum (see eq. 3.3 and 3.4).

$$\frac{\partial(\rho u_i)}{\partial t}+\frac{\partial(\rho u_i u_j)}{\partial x_j}=-\frac{\partial p}{\partial x_i}+[\mu\left(\frac{\partial u_i}{\partial x_j}+\frac{\partial u_j}{\partial x_i}\right)]_j \tag{6.1}$$

The equation of continuity was described as well, and it will be used in the following paragraphs.

$$\frac{\partial \rho}{\partial t}+\frac{\partial(\rho u_i)}{\partial x_i}=0 \tag{6.2}$$

Surface and bottom boundary conditions.

In order to obtain solutions of the differential equations it is necessary to establish boundary conditions. For the derivation of the SWE, first of all the conditions at the free water surface and at the solid bottom are set.

The kinematic conditions say that water particles will not cross either boundary. For the solid bottom, this means that the *normal* velocity component must vanish:

$$u\frac{\partial z_b}{\partial x}+v\frac{\partial z_b}{\partial y}-w=0 \text{ at } z = z_b \tag{6.3}$$

where z_b is the bottom level, measured from some horizontal reference level.

At the free surface, the surface may be moving by itself. Then the *relative* normal velocity must vanish:

$$\frac{\partial z_h}{\partial t}+u\frac{\partial z_h}{\partial x}+v\frac{\partial z_h}{\partial y}-w=0 \text{ at } z = z_h \tag{6.4}$$

where z_h is the surface level measured from the same horizontal reference level.

Secondly, dynamic boundary conditions deals with the forces acting at the boundaries. At the bottom it is assumed that the viscous fluid “sticks” to the bottom, i.e.

$$u=v=0 \tag{6.5}$$

which is called the “*no-slip” condition*.

At the free surface, continuity of stresses is assumed, i.e. the stresses in the fluid just below the free surface are assumed to be the same as those in the air just above. This means that surface tension is not taken into account. For pressure, it is found that $p=p_a$, where p_a is the atmospheric pressure.

Boundary-layer form.

The equations (6.1) and (6.2) can be simplified with the assumptions on the scales from the previous paragraph and the consideration of the *hydrostatic pressure distribution*:

$$\frac{\partial p}{\partial z}=-\rho g \tag{6.6}$$

By integrating from the free surface using boundary condition:

$$p = g\int_{z_b}^{z_h} \rho dz + p_a \tag{6.7}$$

Density can be assumed to be constant over the depth, giving the special case:

$$p = \rho g(z_h - z_b) + p_a \tag{6.8}$$

From the last equation, the pressure gradients in (6.8) can be determined, e.g.

$$\frac{\partial p}{\partial z} = \rho g\frac{\partial z_h}{\partial x} + g(z_h - z_b)\frac{\partial \rho}{\partial x} + \frac{\partial p_a}{\partial x} \tag{6.9}$$

Collecting all results so far, the momentum equation becomes: (6.10)

$$\frac{\partial u}{\partial t} + \frac{\partial}{\partial x}(u^2) + \frac{\partial}{\partial y}(uv) + \frac{\partial}{\partial z}(uw) + g\frac{\partial z_h}{\partial x} + \frac{g}{p_o}(z_h - z_b)\frac{\partial \rho}{\partial x} + \frac{1}{p_o}\frac{\partial p_a}{\partial x} - \frac{1}{p_o}\{\frac{\partial \tau_{xx}}{\partial x} + \frac{\partial \tau_{xy}}{\partial y} + \frac{\partial \tau_{xz}}{\partial z}\} = 0$$

$$\frac{\partial v}{\partial t} + \frac{\partial}{\partial x}(uv) + \frac{\partial}{\partial y}(v^2) + \frac{\partial}{\partial z}(vw) + g\frac{\partial z_h}{\partial y} + \frac{g}{p_o}(z_h - z_b)\frac{\partial \rho}{\partial y} + \frac{1}{p_o}\frac{\partial p_a}{\partial y} - \frac{1}{p_o}\{\frac{\partial \tau_{yx}}{\partial x} + \frac{\partial \tau_{yy}}{\partial y} + \frac{\partial \tau_{yz}}{\partial z}\} = 0$$

This set, together with the equation (6.2), is called the ***“3D shallow water equations*”.**

6.2.1.2. Two-dimensional shallow-water equations.

The final step towards the 2D-SWE involves integration of the horizontal momentum equations and the continuity equation over the depth. If the water depth is denoted by $h=z_h - z_b$, the result of the integration over the depth is:

(6.11)

$$\frac{\partial}{\partial t}(hu) + \frac{\partial}{\partial x}(hu^2) + \frac{\partial}{\partial y}(huv) + gh\frac{\partial z_h}{\partial x} + \frac{gh^2}{2p_o}\frac{\partial \rho}{\partial x} - \frac{1}{p_o}\tau_{bx} - \frac{\partial}{\partial x}(hT_{xx}) - \frac{\partial}{\partial y}(hT_{xy}) = 0$$

$$\frac{\partial}{\partial t}(hv) + \frac{\partial}{\partial x}(huv) + \frac{\partial}{\partial y}(hv^2) + gh\frac{\partial z_h}{\partial y} + \frac{gh^2}{2p_o}\frac{\partial \rho}{\partial y} - \frac{1}{p_o}\tau_{by} - \frac{\partial}{\partial x}(hT_{xy}) - \frac{\partial}{\partial y}(hT_{yy}) = 0$$

Together with (6.2) these equations form the **2D *shallow-water equations***. The lateral stresses include viscous friction, turbulent friction and differential advection:

$$T_{ij} = \frac{1}{h}\int_{z_b}^{z_h}\{v(\frac{\partial u_i}{\partial x_j} + \frac{\partial u_j}{\partial x_i}) - \overline{u'_i u'_j} + (u_i - \bar{u}_i)(u_j - \bar{u}_j)\}dz \tag{6.11.b}$$

6.2.2. Finite elements.

The numerical model *FinLab* is a finite-element method (FEM). This method is very flexible for the representation of complicated geometries. FEM is a method of spatial discretization and it can be chosen any method for integrating in time.

In the FEM, the region is divided into a number of basic elements of triangular, but irregular, shape. The unknowns *h, u, v* are approximated by piecewise smooth functions on each element, i.e. in any point (x, y) it is possible to interpolate linearly between the values at the nodes (the corners of the triangle). In this way, the unknowns are defined in the entire region by a sum of piecewise continuous functions.

$$g(x,y,t)=\sum_{i=1}^{N} g_i(t)\phi_i(x,y) \tag{6.12}$$

The fields *u*, *v* are similarly interpolated, using the same interpolation functions but different coefficients. The functions φ is precisely determined by the following requirements:

- φ_i is defined in the entire region.
- φ_i is linear in each element.
- φ_i is 1 in node I, and 0 in all other nodes.

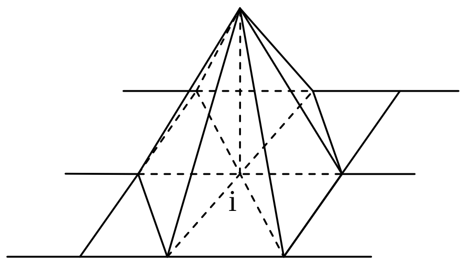

Figure 6.1 Example of piecewise linear interpolation function.
(Vreugdenhil, 1994)

Then, the equations to be solved are multiplied by weighting functions $w_j(x,y)$ and integrated over the area.

6.3. Model description.

In the following sections, experimental data is compared with the results of the 2D numerical model, *FinLab*. The velocity components are discretized in space using triangles.

FinLab uses continuous piecewise linear interpolation functions for the pressure and discontinuous piecewise linear functions for the velocity vector.

The Elder formulation is used to model turbulence with boundary conditions derived from conventional wall functions. In the following subsections, the main parameters of the numerical model are described.

To make a good comparison possible, the numerical model should use the same conditions than the scale model.

6.3.1. Geometry.

The computation domain starts five metres upstream the harbour entrance and represents the geometry of the harbour model from that point to the end of the flume.

The same coordinate system used for the laboratory experiments and the data analysis (see Section 4.5) is employed. Consequently, the domain of the numerical model ranges from X=0m (beginning of the river stream) to X=10m (threshold of the model) and Y=-1.8m (harbour basin right side) to Y=1.2m (left bank of the river stream).

The origin of the Y-axis is located at the right bank of the river stream. The reference point O (0,0) is located 5 metres upstream the harbour entrance. Consequently, the upstream corner has coordinates (5,0).

The coordinate Z=0m is located at the water depth level established as one of the boundary conditions downstream the harbour entrance.

The water depth is 0.14m, as a result, the bottom is located at Z=-0.14 m. *Figure 6.2.a* shows the geometry considered in FinLab.

6.3.2. Spatial discretization.

The size of a spatial calculation step is a compromise between the minimum required mesh size with which the harbour model can be reproduced and the maximum number of mesh points to make the computation feasible.

The domain was discretized with a structured grid of 16,365 triangular cells, in which the mesh size is equal to approximately half the water depth. In the area of interest, the harbour entrance, the resolution is increased to approximately 1/5 of the water depth.

With this resolution, the coherent structures larger than the water depth can be resolved. *Figure 6.2.b.* presents the numerical grid with the area of the harbour entrance where the resolution was increased.

6.3.3. Time step.

The temporal step size is related to the time scale of the process being examined, i.e. the coherent structures in the mixing layer between the river and the harbour. The Courant number based on the velocity was set to approximately 3 resulting in a time step t = 0.5s.

6.3.4. Simulation period.

The simulation period is determined by the time necessary to obtain a dynamic equilibrium situation.

A period of 2500 s (5000 time steps) is established to get a time range with stable results (from step 4000 to 5000).

With this time period, the model needs between 2-4 hours to develop a simulation.

6.3.5. Boundary and flow conditions.

Some boundary conditions are required to model the harbour. The different boundaries in the problem are shown in *Figure 6.2.b.*

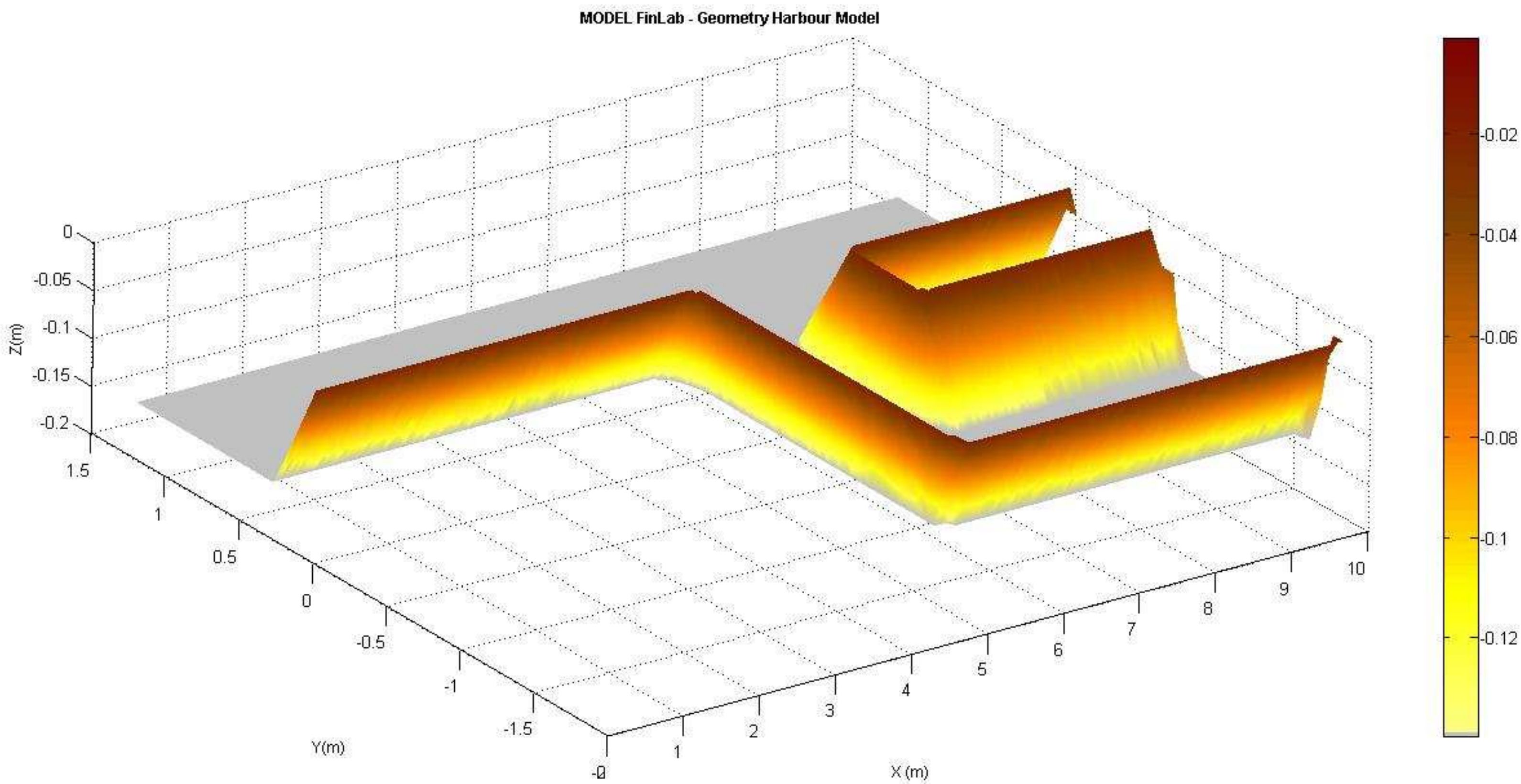

Figure 6.2.a. Geometry of the harbour model with FinLab.

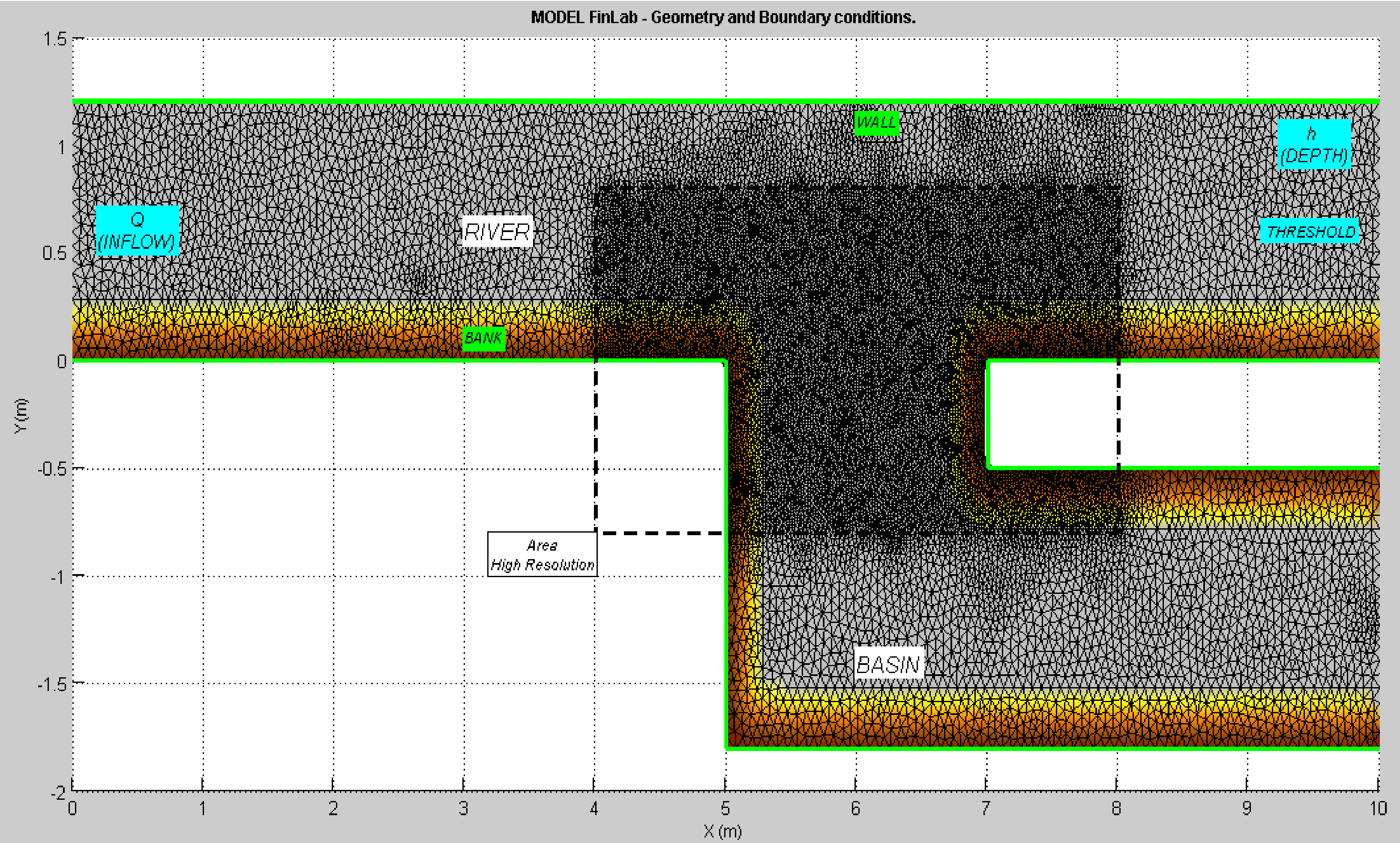

Figure 6.2.b. Boundary conditions and cells of the harbour model with FinLab.

These boundary conditions are the wall at the left bank of the river stream, the geometry of the harbour basin and the surface level, which is set at the downstream end whereas the flow discharge is prescribed at the inflow boundary.

The flow conditions are chosen in accordance with experiment Test 2 (Reference Case) to establish the same state in the model as in the experiments, before the implementation of the groyne.

6.3.6. Parameters of the numerical model.

- Bottom friction

The bottom friction can be defined by different parameters. For this model, the Chezy roughness coefficient C ($m^{1/2}/s$) is used. This coefficient increases with channel size and it follows the expression:

$$C = \frac{R^{1/6}}{n}$$

where n is the Manning's roughness factor ($s/m^{1/3}$) and R is the hydraulic radius (m).

In general, C varies from 30 $m^{1/2}/s$ (small rough channels) to 90 $m^{1/2}/s$ (large smooth channels). The following values of the Chezy roughness coefficient were established for the numerical model.

Material	n	h(m)	R(m)	C($m^{1/2}/s$)
Glass	0.01	0.14	0.1097	**69**
Stone	0.029	0.14	0.1097	**24**

Table 6.1. Chezy coefficients.

Figure 6.3 shows the previous values of the bottom friction at the harbour model.

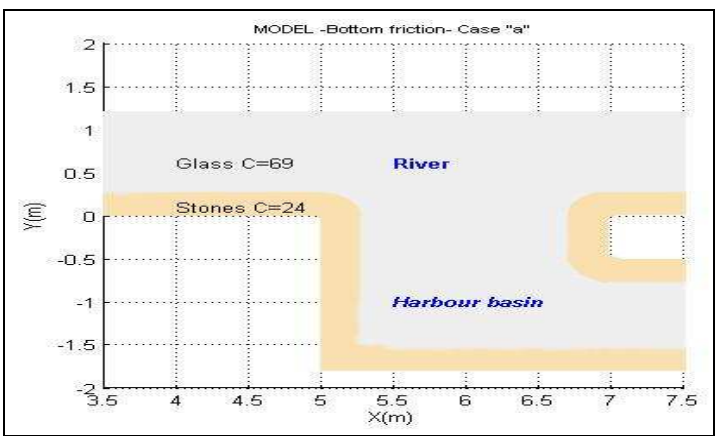

Figure 6.3. Distribution of Chezy coefficients in FinLab.

The bottom friction will be modified at the location of the groyne to include the effect of the groyne on the numerical modelling.

- Eddy viscosity

An assumption is made that the Reynolds stresses are related to the velocity gradients of the flow by a viscosity analogous to the molecular viscosity, i.e. a turbulent or eddy viscosity. While the molecular viscosity is a property of the fluid, the eddy viscosity is a property of the flow.

FinLab presents the simplest model for channel flows, the Elder formulation. This formulation uses a depth-averaged eddy viscosity υ_t, given by the following expression (taken from *Van Prooijen, 2004*):

$$\upsilon_t = \beta \cdot u_* \cdot h = \beta \cdot \sqrt{c_f} \cdot U \cdot h \tag{6.13}$$

in which *h* is the water depth, *U* is the depth-averaged streamwise velocity and the parameter β could be considered the dimensionless eddy viscosity and it may range from approximately 0.07 to about 0.3. The Chezy coefficient is related with the bed friction coefficient by means of the following expression (also included in Appendix D):

$$C = \sqrt{\frac{g}{c_f}} \tag{6.14}$$

From Table 6.1., the results of the bed friction coefficient for both materials (glass and stones) are 0.0022 and 0.017, respectively.

The eddy viscosity is considered at the numerical model from the expression as follows:

$$\upsilon_t = \upsilon_0 + \beta \cdot u_* \cdot h = \upsilon_0 + \beta \cdot \sqrt{c_f} U \cdot h \tag{6.15}$$

where υ_0 and β will vary depending on the case.

6.4. Numerical results.

6.4.1. Previous considerations.

As *FinLab* obtains the depth-averaged velocity field, PTV results from Test 2 (Reference case) and Test 6 (groyne case) have to be transformed into averaged values over the depth. *Appendix C* gives the description of this transformation into depth-averaged values.

Before the comparison between the numerical model and the laboratory experiment with groyne, the definition of the reference case in the numerical model has to be accomplished.

Several parameters of the numerical model were calibrated to get a good agreement between the reference experiment and *FinLab*.

The model case with the same conditions as Test 2 will be labelled *Case “0”*. In Several combinations (Case “a” to Case “f”) were performed to achieve the best example to get the reference case in *FinLab*. The model case with the implementation of the groyne will be labelled *Case 1*.

6.4.2. Case 0. Reference case.

In the following, the streamwise and transverse components of the velocity from the numerical results will be symbolized by U and V. In addition, PTV results from the reference experiment (Test 2) after the transformation into depth-averaged values will also be denoted by U and V.

6.4.2.1. First case – Case “a”.

For the first numerical simulation, the following parameters were established.

Case	Q(l/s)	C ($m^{1/2}/s$)	υ_o (m^2/s)	β
“a”	39.3	24 / 69	$1\cdot10^{-5}$	0.1

Table 6.2. Parameters FinLab. Case “a”.

The magnitude of υ_o has been chosen one order lower than the second term of the equation 6.15. As c_f is 0.0022, and U_{mean} is equal to 33.2 cm/s at the river stream for Test 2 (see Appendix C), the second term results in $2.2\cdot10^{-4}$ m^2/s. Consequently, υ_o is defined as $1\cdot10^{-5}$ m^2/s.

In order to adjust the numerical model with the reference case of the experiments, several aspects are taken into account:

- The lateral profile of the mean streamwise velocity along the harbour entrance.
- The distribution of the standard deviation of the transverse velocity, V_{std}.

	Ref. Case. Exp.	***FinLab Case “a”***
U_{mean}(y=0.59m)	33.2	27.15

Table 6.3. Results of U_{mean} (cm/s) at the river stream for Case “a”.

As it can be observed in *Table 6.3*, the value of the mean streamwise velocity at the river stream (Y=0.59m) is lower for the numerical model.

From these results it was concluded that the value of the flow discharge taken from the experiments does not correspond with the velocities given by PTV data (it would correspond with a higher inflow) and consequently, the numerical model gives lower velocities than the reference case.

After several verifications, it was concluded that the velocities given by the PTV algorithm correspond with the real velocity values from the experiments. For this reason, this incongruity can be attributed to an error in the flow meter during the laboratory experiments, and, as a result, the flow conditions will be modelled with a different value of the discharge which will be determined by comparison with the results from the experiment (PTV).

Fortunately, this change does not affect the previous data analysis (Chapter 5) because the value of the flow discharge was constant during all the experiments and was not used during the data processing.

6.4.2.2. Change inflow boundary condition – Cases "b", "c" and "d".

Several cases with different values of the flow discharge were analysed. In these combinations, the rest of parameters remain equal to Case "a", except for the flow discharge.

Case	Q(l/s)	C ($m^{1/2}$/s)	υ_o (m^2/s)	β
"b"	**42**	24 / 69	$1 \cdot 10^{-5}$	0.1
"c"	**45**	24 / 69	$1 \cdot 10^{-5}$	0.1
"d"	**48**	24 / 69	$1 \cdot 10^{-5}$	0.1

Table 6.4. Parameters FinLab. Cases "b", "c" and "d".

Figure 6.4.a represents the lateral profiles of the mean streamwise velocity at section "A"(X=5.47m) for Cases "a", "b", "c" and "d", together with the PTV results of Test 2.

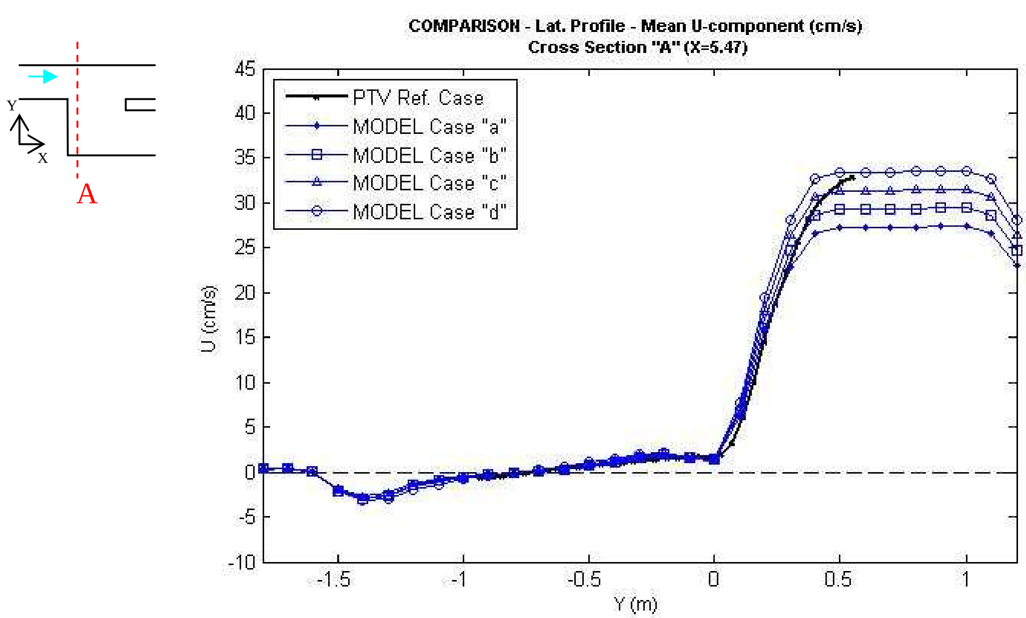

Figure 6.4.a Lateral profile of mean U-component. Section A (X=5.47m). Cases "a", "b", "c" and "d".

From the profiles of *Figure 6.4.a* it can be identified that the gradient of the U-component along the cross section is similar for all cases. The profile diverges at the river stream, providing a higher river velocity in accordance with the inflow value. Case "d" reaches the value of the PTV results at the river stream in comparison with the experiment (black line).

As it is listed in *Table 6.5*, Case "d" presents the same mean streamwise velocity at the river stream than the experiment, with an inflow condition of 48 l/s.

Ref. Case. Exp.	***Case "a"***	***Case "b"***	***Case "c"***	***Case "d"***
33.2	27.15	29.20	31.25	33.29

Table 6.5. Results of U_{mean} (cm/s) at the river stream for Cases "a", "b", "c" and "d".

All cases present the same velocities within the harbour basin (from Y=-0.5 to Y=0m) and they fit in with the PTV profile.

Figure 6.4.b presents the distribution of the standard deviation of the transverse velocity (V_{std}) at the same cross section. From these plots it can be remarked that the peak is higher for the case with the largest flow discharge.

However, no effect is observed in the position of this peak because all cases present the same y-coordinate which is close to Y=0m (harbour entrance line). This location corresponds with the apex of the entrance (the vertex of the corner where it starts the transition between river and harbour).

For this reason, it can be concluded that the inflow does not influence the distribution of V_{std} in space, but the values within the harbour basin are higher for cases with larger inflow and consequently, they deviate from the PTV profile (black line).

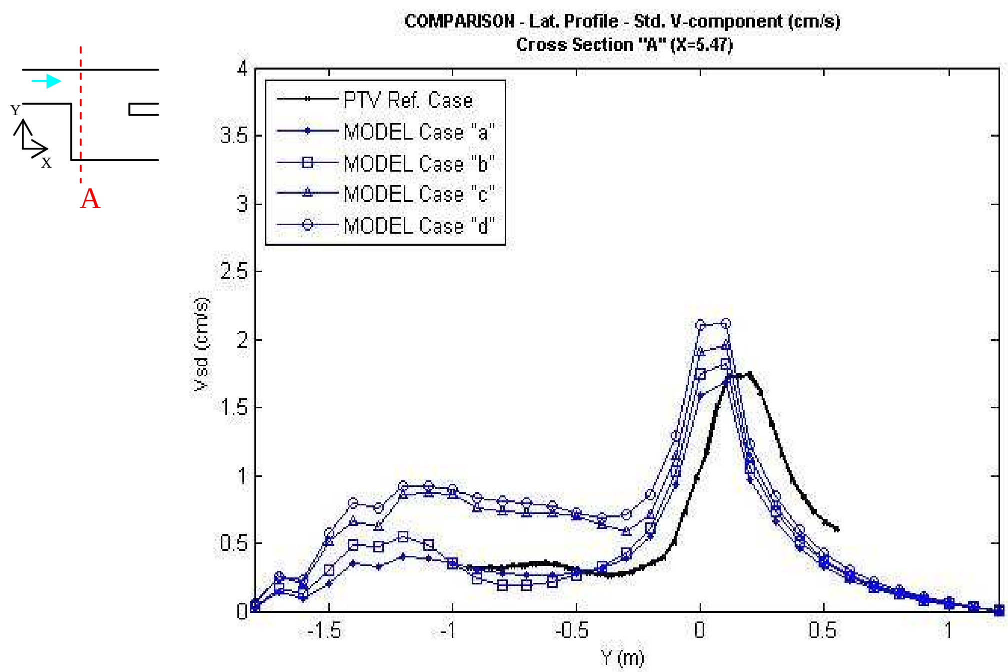

Figure 6.4.b Lateral profile of Std V-component. Section A (X=5.47m).
Cases "a", "b", "c" and "d".

From the previous results it can be concluded that the inflow condition for Case “d” (48 l/s) will be defined as the reference flow discharge in *FinLab*.

In order to search improvements for this combination, two changes in the viscosity parameters were performed to analyse the variations in the numerical results.

6.4.2.3. Changing the eddy viscosity - Cases “e” and “f”.

To determine the effect of the viscosity parameters in the numerical results, two new cases were performed with *FinLab*. These cases have the same inflow condition as Case “d”.

Case “e” presents a higher value of β, the dimensionless eddy viscosity, and *Case “f”* shows a higher υ_o.

Case	Q(l/s)	C ($m^{1/2}$/s)	υ_o(m^2/s)	β
“e”	48	24 / 69	$1{\cdot}10^{-5}$	0.15
“f”	48	24 / 69	$1{\cdot}10^{-4}$	0.10

Table 6.6. Parameters FinLab Cases “e” and “f”.

The same considerations are applied with these two cases to determine the variations in the numerical results.

Ref. Case. Exp.	***Case “d”***	***Case “e”***	***Case “f”***
33.2	33.29	33.27	33.2

Table 6.7. Results of U_{mean} (cm/s) at the river stream for Cases “d”, “e” and “f”.

As it is listed in the previous table, the consideration of the mean river velocity does not provide any interesting difference between cases because the mean value of the river stream velocity remains constant for all combinations.

However, if the lateral profile of the mean U-component is considered, see *Figure 6.5.a*, in that case, a deviation in Case “f” (magenta line) is presented within the harbour basin (Y=-1.2m).

From *Figure 6.5.b,* V_{std} decreases for Case “e” (green line) within the harbour basin and consequently, it provides a better result in accordance with the experiment.

In contrast, V_{std} is null for all points along cross section X=5.47m in Case “f”. In this case the initiation of the coherent structures is suppressed by the high viscosity.

The results of Cases “d” and “e” present the right magnitude of the viscosity equation (first term one order lower than the second term, see equation 6.15) to obtain reasonable results.

From the new value of β, a better agreement between the reference experiment and the model is achieved, but it has not been possible to obtain an improved accordance between model and experiment in relation with the V_{std} distribution, which is shifted 10 cm towards the harbour basin with respect to PTV results. A possible improvement could lie in the roughening of the slopes. Rougher slopes will shift the mixing layer towards the river.

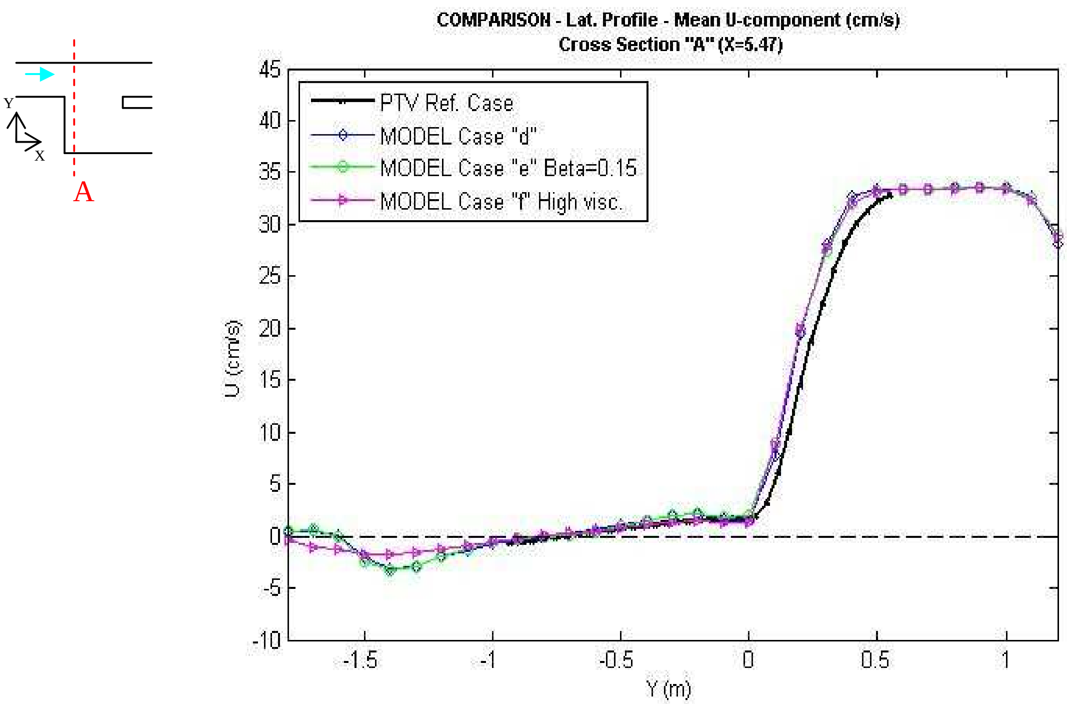

Figure 6.5.a Lateral profile of mean U-component. Section A (X=5.47m). Cases "d", "e" and "f".

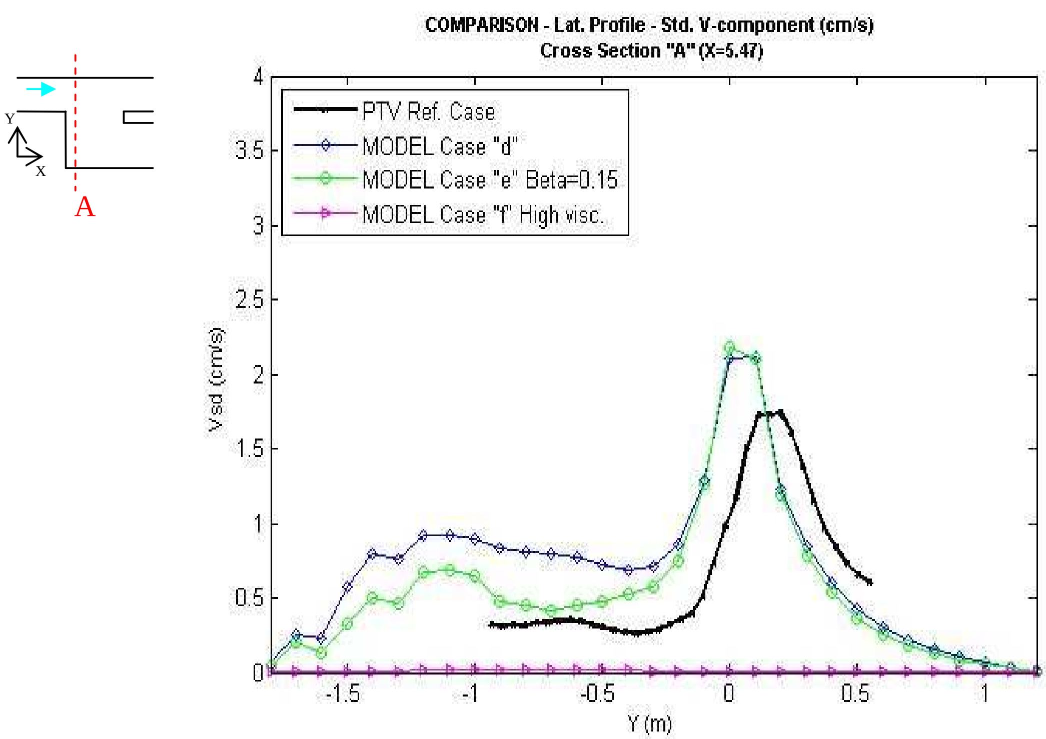

Figure 6.5.b Lateral profile of Std V-component. Section A (X=5.47m). Cases "d", "e" and "f".

6.4.2.4. Validation turbulence properties.

Case "e" will be defined as the Case "0" of the numerical model, the model case which reproduces the flow conditions of the reference experiment without groyne.

The average flow conditions of the reference experiment are accomplished by this case, but the turbulence properties have not been analysed until now.

In this paragraph, the Reynolds shear stress $\overline{u'v'}$ and the autocorrelation functions for the reference experiment are compared with the model Case "0".

Figure 6.6 shows the distribution of the Reynolds shear stress $\overline{u'v'}$ over the PTV area and the results of the numerical model for Case "0".

The left figure corresponds with the distribution of $\overline{u'v'}$ for the laboratory experiment. A region with negative values covers the harbour entrance, which are characteristics of the mixing layer area due to the gradient of the streamwise velocity from river to harbour.

This region is also present in the model results but with a narrower width and it develops in downstream direction towards the river stream instead of being developed towards the basin.

The downstream side of the entrance presents high positive values of the shear stress for the experiment which are not present in the model case. The region is concentrated near the downstream corner in FinLab.

Figure 6.7 gives the autocorrelation functions at locations E6, A1, A4, A5 and A7 for both cases: experiment and model.

The left figure presents the autocorrelation functions from the experimental results. There is a clear difference between the time scales at the river stream (A5, magenta line) and at the harbour basin (E6, blue line). The time scales increase going downstream with a value of 12 seconds at location E6.

However, the numerical model presents the same autocorrelation functions for all cases, and the results do not depend on the location of the point. The development of the coherent structures is not represented.

As a result, all these points present the same time scales and it implies that the model is not modelling properly the differences between the mixing layer and the river stream which are characteristic of different flow regimes.

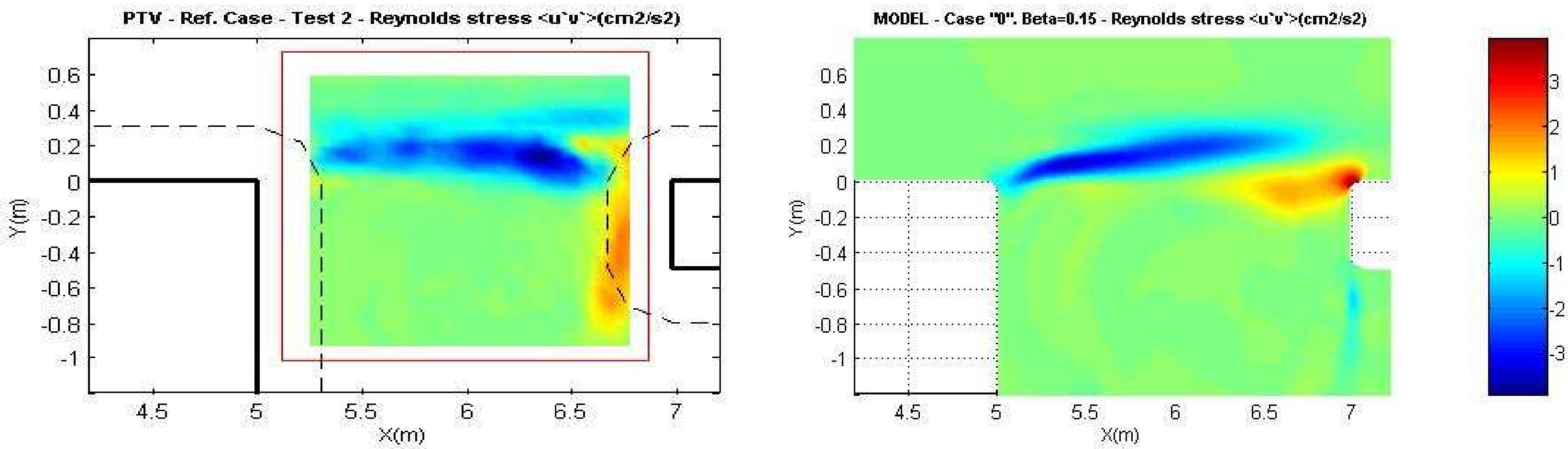

Figure 6.6 Distribution of $\overline{u'v'}$ (cm^2/s^2). Reference experiment and model Case "0".

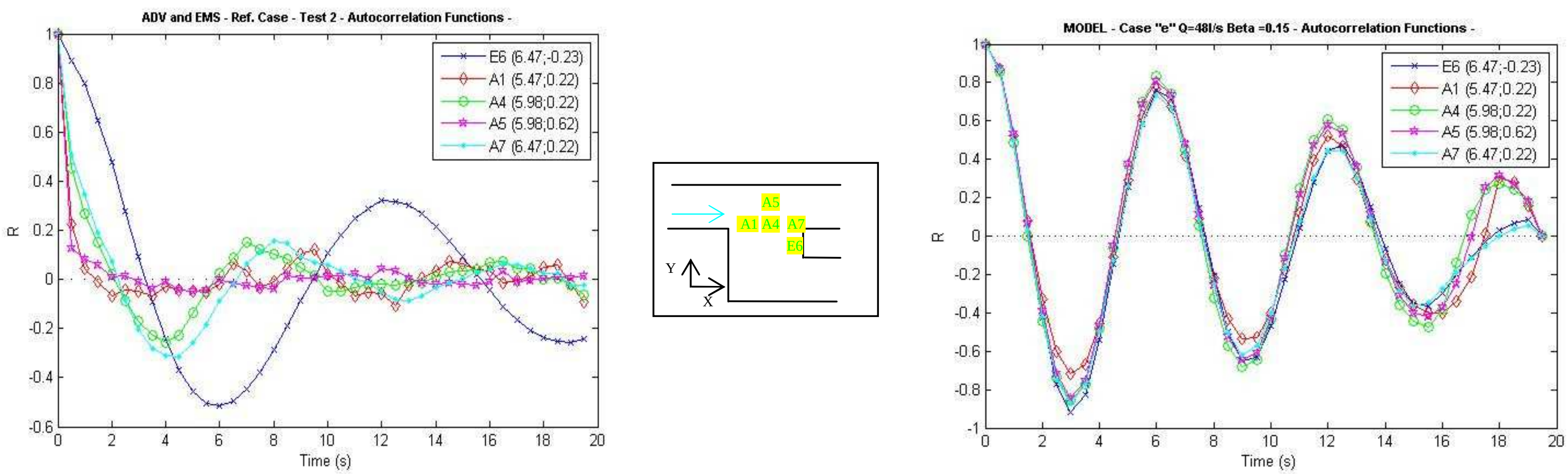

Figure 6.7 Autocorrelation functions. Reference experiment and model Case "0".

6.4.3. Case 1. Groyne.

Once the reference simulation has been set up, the implementation of the effect of the groyne on the model has to be carried out. For this purpose, a variation on the roughness coefficient will be applied to simulate the groyne upstream the entrance.

A different roughness coefficient will be established by considering the loss of energy produced at the river stream due to the piles. The same methodology which is applied in other models (Delft 3D, HEC-RAS, etc.) to implement the effect of piers is used. The assumption of this new Chezy coefficient and finding its proper value are described in *Appendix D*. After the considerations given in Appendix D, a value of C=1 $m^{1/2}/s$ is defined for the new model case.

6.4.3.1. Model case with Chezy C=1.

The low roughness coefficient is established in an array of cells between the points (4.65, 0.06) and (4.65, 0.39), the same coordinates where the groyne was defined at the experiment (Test 6). This model case is labelled Case "1" and it has the same conditions as Case "0".

Case	Q(l/s)	C ($m^{1/2}/s$)	$\upsilon_o(m^2/s)$	β
"1"	48	**1** / 24 / 69	$1 \cdot 10^{-5}$	0.15

Table 6.8. Parameters FinLab Case "1".

At this point, both experiments (reference and groyne) will be compared with the model cases "0" and "1".

Figure 6.8.a shows the lateral profile of the mean streamwise velocity for these four cases. As it is shown in this figure and listed in table 6.9, the model case "1" presents higher velocities at the river stream as a consequence of the change of the flow direction at the location of the new roughness.

Ref. Case. Exp.	***Groyne Case Exp***	***Case "0"***	***Case "1" C=1***
33.2	32.58	33.27	40.93

Table 6.9. Results of U_{mean} (cm/s) at the river stream for Cases "0" and "1" and experiments.

This increase on the river velocities is shown in *Appendix E* (figure E.1) where the colormaps of the mean U-component are given. The high roughness blocks the flow at the river stream and it follows going round the modified cells.

The high bottom friction reduces the velocities near the edge of the groyne in a similar manner as it was observed in the experiments, but lower values of the streamwise velocity are observed along the harbour entrance for the model, which are much lower than in the experiment.

Moreover, a closer look in Figure 6.8.a from results of Case "1" (cyan line) shows a peak on the mean streamwise velocity at Y=0 m. This peak is also shown in figure E.1 and it corresponds with the flow which is diverted through the right side of the modified cells (the groyne starts at Y=0.06m and the flow separates opposite the array towards the river stream and the embankment, respectively). This deviation is not present at the laboratory experiment because the flow passes through the piles, but in the numerical model, the cells form a continuous line.

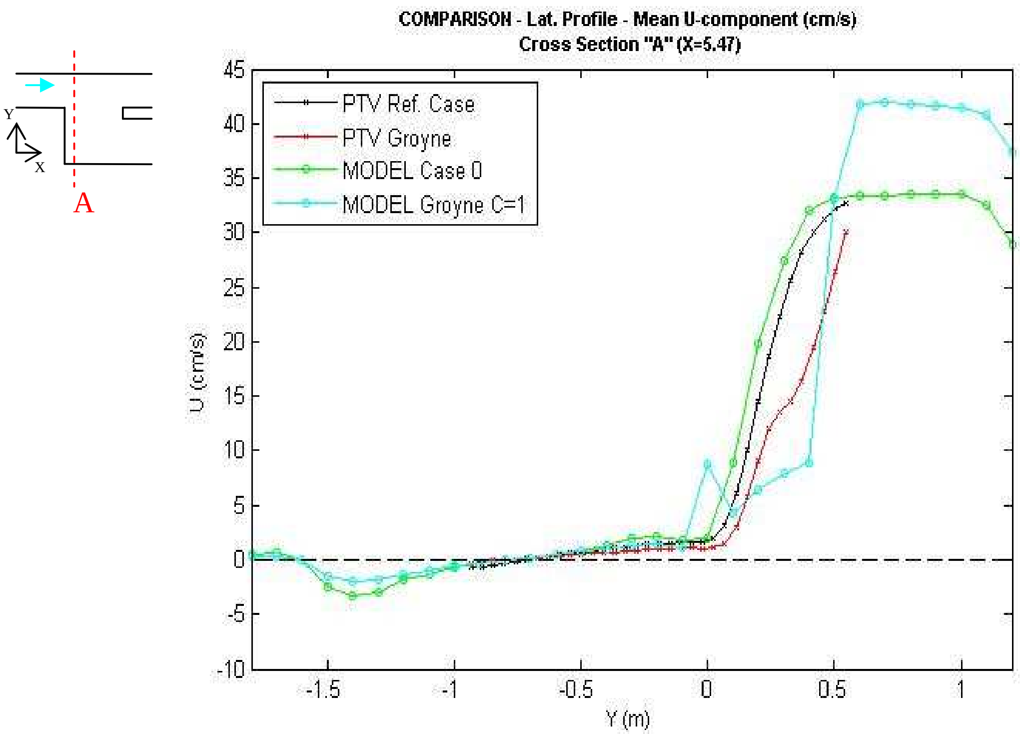

Figure 6.8.a Lateral profile of Mean U-component. Section A (X=5.47m). Cases "0" and "1"(C=1).

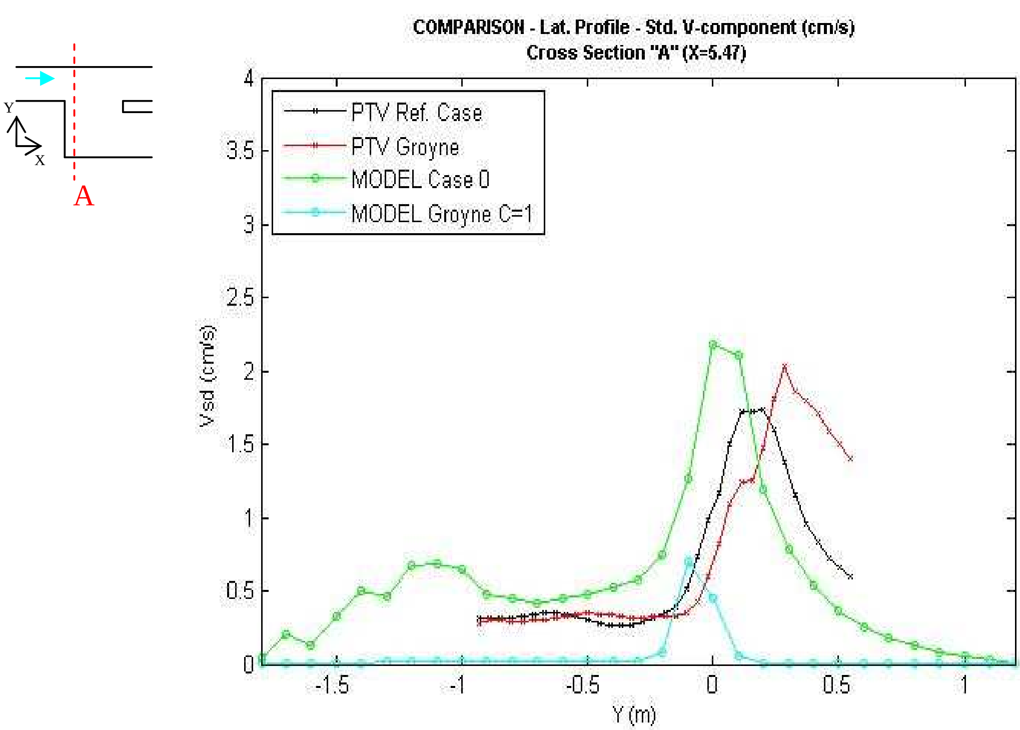

Figure 6.8.b Lateral profile of Std V-component. Section A (X=5.47m). Cases "0" and "C=1".

From figure 6.8.a, other differences with respect the experiment with groyne (red line) can be found.

The slope is steeper for the numerical model. The experiment presents a gradual change from river velocity to harbour velocity, but it is not the case for the model, in which the mean streamwise velocity drops significantly near Y=0.5 m.

Moreover, the variation on the PTV profile (red line at Y=0.3m) due to the presence of two mixing layers (one due to the edge of the groyne and other owing to the interface river-harbour) is not found at the model.

In *Figure 6.8.b* the distributions of the standard deviation of the V-component are plotted. The experiment with groyne (Test 6, red line) does not differ much from the reference experiment (black line), however a clear reduction of V_{std} is found. From Appendix E (figures E.3 and E.4), it can be observed that Case “1” does not show deviation values over the whole model area.

It means that this simulation offers constant results in the time and consequently, no fluctuation of the flow regime is obtained. As a result, no production term and no turbulence are found.

A clear example is found in *Figure 6.9,* in which the Reynolds shear stress for Test 6 and Case “1” is plotted. The numerical model gives zero values over the whole area, except for a small area near the upstream corner.

The comparison of the time signals from Cases “0” and “1” explains why the results of the model dhow the previous behaviour.

From *figure 6.10*, the right plot presents the time signal at locations A1, A4 and A7 (Y=0.22m) for the case with the modified roughness upstream the harbour entrance. The fluctuation of these signals is insignificant (the vertical axis ranges from 0.055 to 0.07 m/s). On the other hand, the left figure displays the signals of the same points and it is present a clear fluctuation which varies from 0.18 to 0.24 m/s.

In conclusion, Case “1” is not valid for the purpose of this thesis and the comparison with the experiment is not feasible due to the absence of turbulence and only conclusions regarding the average flow field can be drawn.

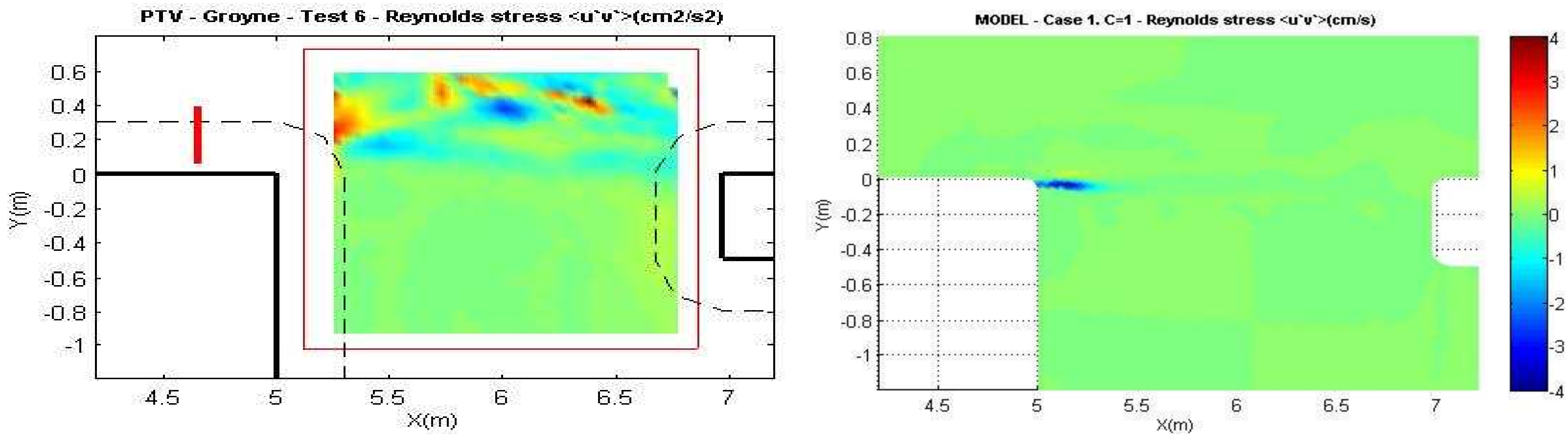

Figure 6.9 Distribution of $\overline{u'v'}$ (cm^2/s^2). Groyne experiment Test 6 and model Case “1” C=1.

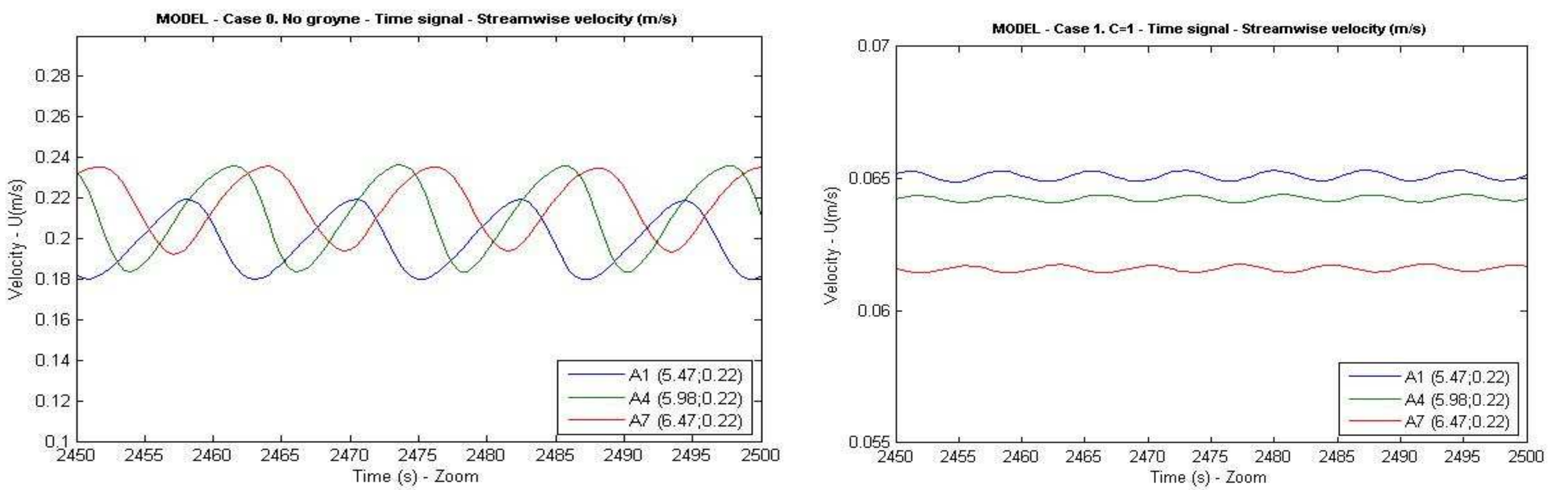

Figure 6.10 Time signal of U-component at points A1, A4 and A7.

6.4.3.2. Effect of the high roughness.

As it was stated in the previous paragraph, the modification of the roughness to C=1 $m^{1/2}/s$ was not successful and here a variation of this parameter is established to search for improved results of the numerical simulation.

For this purpose, the Chezy coefficient is varied to C=2 and 5 $m^{1/2}/s$, respectively, to observe the differences with Case C=1.

From *Figure 6.11* a clear decrease of the mean river velocity can be observed for cases C=2 (cyan-stared line) and C=5 (cyan-circled line). As expected the mean streamwise velocity decreases at the river stream due to the lower effect of the roughness in case C=5, and it fits with the model Case "0"(green line).

However, a higher similarity is found between Case C=2 and the experiment with groyne (red line), in which the profile follows the same tendency of the experiment and it presents the variation resultant of the presence of two mixing layers.

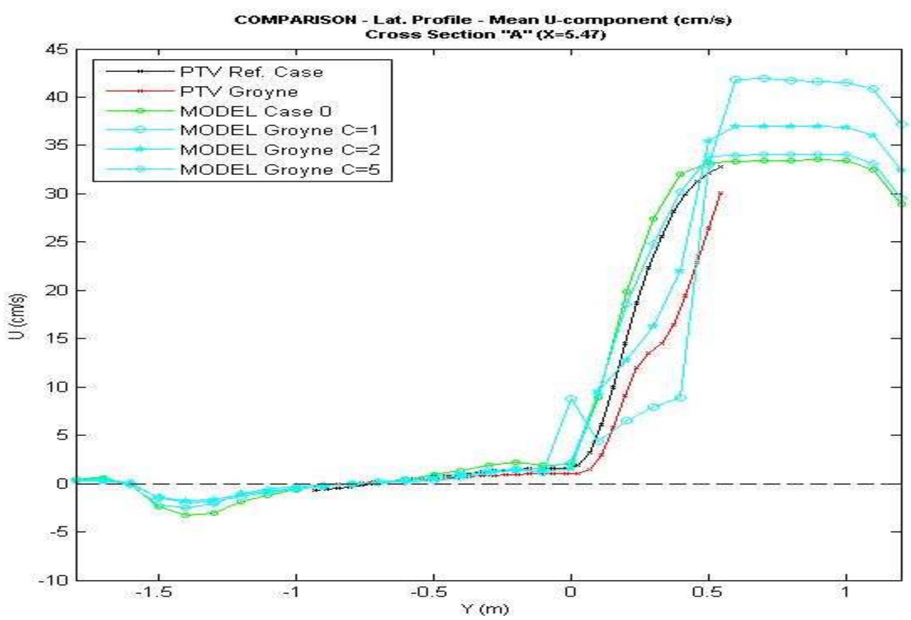

Figure 6.11 Lateral profile of mean U-component (cm/s). Section "A" (X=5.47m). Cases C=1, 2 and 5.

From the comparison of the different time signals for Cases with C=1, 2 and 5 $m^{1/2}/s$ in *Figure E.5* (Appendix E) and the colormaps given in *Figure E.6* some remarks can be made.

A clear tendency to a constant value is observed in the first two cases in figure E.5. As a result, Case C=2 presents the same feature as the previous model simulation in spite of the improved results with respect the streamwise velocity profile discussed above. However, the signal for Case C=5 displays the pattern shown in figure 6.10 for Case "0" and the absence of fluctuation is avoided, but if figure E.6 is considered, the result obtained from the modified roughness C=5 looks approximately the same as the case without groyne. It indicates that this magnitude for the roughness coefficient is not suitable to represent the blocking effect due to the groyne.

6.5. Summary.

From the simulations carried out in this chapter the following conclusions can be drawn:

Good agreement was found between the experiments and the model for the reference case without groyne. After several modifications, like the flow discharge and the dimensionless viscosity coefficient, similarities are found between both cases with respect the mean flow field and the Reynolds shear stress distribution.

However, a better study of the reference model case has to be performed to find viable modifications in the programme to improve the present results.
An example would be the reduction of the high velocities produced near the downstream corner of the harbour entrance.

The case with the groyne was not simulated properly. Several reasons could be possible. The parameterization of the groyne by an increased roughness (and subsequently an increased eddy viscosity) is not appropriate. Another reason could be the lack of artificial disturbances to start up the coherent structures.

As it is shown in Van Prooijen (2004), these disturbances are required in mixing layers. In case of the groyne, the mixing layer is wider, leading to a less strong enhancement of disturbances. Apparently, the suppressing effect of the viscosity is stronger than the enhancement of the disturbances by the shear. A similar effect was observed by increasing the viscosity. In that case, the suppressing effect also dominated.

In conclusion, the model especially needs improvement to simulate the dynamic behaviour of the flow. Some recommendations are given in the next chapter.

CHAPTER 7.

CONCLUSIONS AND RECOMMENDATIONS.

In this chapter the main conclusions are written down and recommendations are given on the continuation of this project.

From the results of the experiments and the numerical model, several conclusions are drawn in Section 7.1 and recommendations are done in Section 7.2.

7.1. Conclusions.

The results of the thesis suggest that data analysis from the laboratory experiments, in combination with numerical modelling, can be a powerful tool with which to gain insight into the effect of the groyne on the exchange process and the consequences of its location. The geometry based on the scale harbour model gave a good agreement between the modelled reference case and the experiment. However, no agreement was found for the case with groyne due to the high viscosity developed by the different bottom friction established at the groyne location.

7.1.1. Experiments.

As it was explained in section 5.4, different results are obtained from the configurations of the groyne. In general, a higher effect on the turbulence properties and the mean flow field has been observed for configurations located near the upstream corner and with a larger number of piles.

A discrepancy between the flow discharge given by the flow meter and the velocities obtained from the PTV and ADV measurements was found during the data analysis. As the flow discharge was constant for all experiments, this parameter was not relevant during the analysis, but it had to be modified during the set up of the numerical model in order to obtain the same flow field (see Chapter 6, section 6.4).

The configuration located further from the entrance (Test 5) has presented similar results with respect other cases, but with the advantage of reducing the high disturbances near the harbour entrance. For this configuration, the changes in the flow direction and the high disturbances are created far from the entrance.

A larger distance between piles does not improve the results during the analysis.

Similarities between tests with the same groyne length but with different number of piles and distances between them have been found. Consequently, the total length has to be considered as a crucial parameter of the configuration of the groyne.

According to the conclusions drawn from the data analysis, it can be concluded that the alternative with a distance between piles around 2/3 of the width and a total length of the sheet (L) which ranges from Y=0.06m to Y=0.39m (of a total river width of 1.20m), located at a distance d~=L upstream the entrance seems to be the best configuration to reduce the exchange in the model studied in the present project.

7.1.2. Numerical model.

Numerical simulations were carried out for the reference case and for the case with an upstream groyne. The results of the reference simulation were, after a calibration process, fairly well. The mean flow and the turbulence intensities were reproduced. However the dynamic development of the eddies in the mixing layer was poorly simulated. The time scale of the eddies did not increase as followed from the autocorrelation functions.

The poor simulation of the eddy development had its influence on the simulation of the case with the upstream groyne. The wider mixing layer did result in a flow without eddies. Apparently, the damping effect of the viscous term dominated over the production due to the shear.

7.2. Recommendations.

The recommendations are focused on the continuation of the study of groyne structures and its implementation in numerical models to gain insight in its behaviour. Recommendations are made in the area of improving and varying the experiments and the calibration of the model to represent the groyne.

7.2.1. Experiments.

- Groyne configuration and harbour geometry.

The geometry of the piles (width, shape) and the harbour basin (area and location of the entrance) were established in advance. The location of the pile sheet was established upstream of the corner at a distance similar to the total length of the array as a general case (d=35cm), and other configurations were established from this stage.

To find out how the groyne could be improved a simple laboratory experiment could be carried out and modelled numerically, in which the flow pattern is not as complex as in this case. A possible proposal could be the modelling of a river without harbour basin to study the effect of the groyne on the river stream.

- Measurement techniques.

Using an acoustic technique as the ADV, velocity measurements were taken at different locations over the depth in points A1 and A7, but data was not valid in many cases due to the low correlation of the signals. In addition, this possibility was introduced in the laboratory experiments after the completion of the first series and it was not possible to establish the vertical profile at the mixing layer for the reference case. Different measurement points over the vertical would provide information about the effect on the flow over the depth.

As the PTV area did not cover the river stream, it was not possible to compare the ADV measurements near the left wall of the river stream with the PTV data. The current PTV area was chosen according to the most convenient dimensions to obtain a good resolution. In order to capture a larger area, the use of two cameras would be an option, but specific attention would be necessary to fix the cameras in the correct orientation. The location of the camera in a higher point with a different configuration would be another alternative.

- Data processing

It is recommended to control the number of particles per frame and the light intensity to allow reliable Particle Tracking Velocimetry. The background images were not totally white due to the strips between plates of the flume. A white background is recommended to obtain high-quality results from the PTV post-processing.

7.2.2. Numerical model.

- Groyne parameterization.

The assumption established to implement the groyne on the numerical model was based on a change on the bottom friction. This assumption is based on the relation between the roughness and the energy loss which is produced due to the presence of the groyne at the river stream.

The increase of the bottom friction also leads to an increase in eddy viscosity at the groyne. On the one hand this seems correct: the turbulence created downstream of the groyne leads to a higher eddy viscosity. On the other hand, in reality the turbulence might grow to large coherent structures. The groyne initiates coherent structures. This last effect is not taken into account by the higher eddy viscosity. The higher eddy viscosity even dampens existing fluctuations. For this reason, it is strongly recommended to reconsider the parameterization of the groyne on both effects.

- Eddy development.

One of the main conclusions of the numerical simulations was that the eddy development was not reproduced properly. This can be improved in different ways.

A possibility is to introduce artificial perturbations, see e.g. Van Prooijen (2003). In this way the coherent structures are triggered. Another, but not replacing, possible way is to reconsider the eddy viscosity model. Other closure models, like the Smagorinsky- or k-ε models could be applied.

REFERENCES.

Barneveld H.J. et al, (2007). *Reductie Sediment in Havens.* Rijkswaterstat RIZA.

Booij R., (1986). *Measurements of exchange between river and harbour*. Delft University of Technology, Delft, The Netherlands.

Christiansen H. et al., (2005). *Reducing Harbor Siltation, Part II. Case Study of Parkhafen in Hamburg.* ASCE. Journal of Waterway, Port, Coastal and Ocean Engineering.

Davidson L. (2003). *An Introduction to Turbulence Models*. Department of Thermo and Fluid Dinamics. Chalmers University of Technology. Goteborg, Sweden.

Eysink *(1990). Morphological response of tidal basins to change*. Proc. 22nd Coastal Engineering Conference, ASCE, Delft, The Netherlands.

Van Schijndel, S.; Kranenburg, C. (1999). *Reducing the siltation of a river harbour.* Journal of Hydraulic Res., Vol. 36, No. 5, pp803-814.

Langendoen E.J., (1992). *Flow patterns and transport of dissolved matter in tidal harbours*. Communications on hydraulic and geotechnical engineering, Report n^o.92-8. Delft University of Technology, Delft, The Netherlands.

PIANC, (2006). *Minimizing Harbour Siltation.* PIANC. Working Group 43.

Raudkivi J., (1996). *Permeable Pile Groins.* ASCE, Journal of Waterway, Port, Coastal and Ocean Engineering.

Uijttewaal and Booij, (2000). *Effects of shallowness on the development of free-surface mixing layers.* Physics of Fluid, Vol.12, No.2.

Uijttewaal W.S.J., (2007*). Turbulence in Hydraulics CT5310.* Delft University of Technology, Delft, The Netherlands.

Van Prooijen B.C., (2004). *Shallow Mixing Layers.* Communications on hydraulic and geotechnical engineering, Report n^o.04-1. Delft University of Technology, Delft, The Netherlands.

Van Prooijen and Uijttewaal, (2002). *A linear approach for the evolution of coherent strucutres in shallow mixing layers*. Physics of Fluid.

Van Schijndel, S. (1998). *Reducing the Siltation of a River Harbour.* Journal of Hydraulic Research, Delft University of Technology, Delft, The Netherlands.

Vreugdenhil C.B., (1994). *Numerical methods for shallow-water flow*. Water science and technology library, Volume 13, Utrecht University. Utrecht, The Netherlands.

Winterwerp J.C., (1992). *Reducing Harbour Siltation, Part I: Methodology*. ASCE, Journal of Waterway, Port, Coastal and Ocean Engineering, 2002.

Winterwerp J.C. et. al., (1994). *The Current Deflecting Wall: A Device to Minimize Harbour Siltation*. Dock Harbour Authority, pp.243-246.

Appendices.

Appendix A.

Coordinates Measurement Points.

"Ax" is the point of the harbour model which corresponds with the same location than the measurement point "ADV x".

"Ex" is the point of the harbour model which corresponds with the same location than the measurement point "EMS x".

"Ux" is the point of the harbour model which corresponds with the same location than the measurement point located upstream the pile groyne "EMS Ux".

Table A.1. Coordinates of measurement points.

NAME	***POINT***	***X***	***Y***	***L. SECT.***	***C. SECT.***	***DESCRIPTION***
A1	*ADV 1*	5.47	0.22	"G"	"A"	Mixing layer.
A2	*ADV 2*	5.47	0.62	"H"	"A"	Intermediate stream line.
A3	*ADV 3*	5.47	1.02	"I"	"A"	Stream line near the left bank of the river.
A4	*ADV 4*	5.98	0.22	"G"	"B"	Mixing layer.
A5	*ADV 5*	5.98	0.62	"H"	"B"	Intermediate stream line.
A6	*ADV 6*	5.98	1.02	"I"	"B"	Stream line near the left bank of the river.
A7	*ADV 7*	6.47	0.22	"G"	"C"	Mixing layer.
A8	*ADV 8*	6.47	0.62	"H"	"C"	Intermediate stream line.
A9	*ADV 9*	6.47	1.02	"I"	"C"	Stream line near the left bank of the river.
A10	*ADV 10*	6.78	0.62	"G"	"D"	Intermediate stream line.
A11	*ADV 11*	6.78	1.02	"I"	"D"	Stream line near the left bank of the river.
E1	*EMS 1*	5.47	-1.35	"E"	"A"	Primary gyre. Inside the harbour basin.
E2	*EMS 2*	5.47	-0.23	"F"	"A"	Primary gyre. Near the entrance.
E3	*EMS 3*	5.98	-1.35	"E"	"B"	Primary gyre. Inside the harbour basin.
E4	*EMS 4*	5.98	-0.23	"F"	"B"	Primary gyre. Near the entrance.
E5	*EMS 5*	6.47	-1.35	"E"	"C"	Primary gyre. Inside the harbour basin.
E6	*EMS 6*	6.47	-0.23	"F"	"C"	Primary gyre. Near the entrance.
E7	*EMS 7*	6.78	-1.35	"E"	"D"	Stagnation point between gyres.
E8	*EMS 8*	6.78	-0.85	-	"D"	End of the block which divides river-harbour.
E9	*EMS 9*	7.98	-1.35			New location for series 4. Harbour basin.
E10	*EMS 10*	7.98	-0.85			New location for series 4.
E11	*EMS 11*	9.14	-0.85			New location for series 4.
E12	*EMS 12*	9.14	-0.85			New location for series 4. End of the basin.
U1	*EMS U1*	3.82	0.35			Upstream the pile groyne.
U2	*EMS U2*	3.82	0.55			Upstream the pile groyne.
U3	*EMS U3*	3.82	0.95			Upstream the pile groyne.

Appendix B.

Data Analysis. Tables - Reynolds shear stresses.

The present appendix includes the tables which list the Reynolds stresses $\langle u'v' \rangle$ and $\langle u'w' \rangle$ obtained from ADV measurements.

These values are obtained at points located in Sections "B" and "G".

- Line "B". Points A4, A5 and A6. Cross section located at X=5.98 m.

These points are placed from Y=0.22 m to Y=1.02 m.

- Line "G". Points A1, A4 and A7. Longitudinal section along the harbour entrance in which Y=0.22 m.

Table B.1 shows the Reynolds shear stress values $\langle u'v' \rangle$ and $\langle u'w' \rangle$ for the previous points along the mixing layer and the stream river for each experiment.

			Test 2		Test 4		Test 3		Test 5	
			Ref. Case		Groyne at 0 cm		Groyne at 35 cm		Groyne at 70 cm	
Line		**X(m)**	**<u'v'>**	**<u'w'>**	**<u'v'>**	**<u'w'>**	**<u'v'>**	**<u'w'>**	**<u'v'>**	**<u'w'>**
	A1	***5.47***	-4.00	1.00	-4.00	-1.00	-4.00	-1.00	-3.00	-1.00
G	***A4***	***5.98***	-6.00	-0.02	-2.00	-0.42	-3.00	-1.00	-4.00	-0.50
Y=0.22m	***A7***	***6.47***	-8.00	0.09	-1.00	-0.17	-1.00	-1.00	-2.00	0.15

			Test 2		Test 4		Test 3		Test 5	
			Ref. Case		Groyne at 0 cm		Groyne at 35 cm		Groyne at 70 cm	
Line		**Y(m)**	**<u'v'>**	**<u'w'>**	**<u'v'>**	**<u'w'>**	**<u'v'>**	**<u'w'>**	**<u'v'>**	**<u'w'>**
	A4	***0.22***	-6.00	-0.02	-2.00	-0.42	-3.00	-1.00	-4.00	-0.50
B	***A5***	***0.62***	1.00	0.43	-3.00	0.42	-2.00	1.00	-3.00	0.35
X=5.98m	***A6***	***1.02***	-0.12	1.00	-0.03	1.00	-0.25	0.31	-0.24	0.47

Table B.1. Series 1. Reynolds shear stresses u'v' and u'w' from ADV data (cm^2/s^2).

For the case with groyne at d=0 cm (Test 4), $\langle u'v' \rangle$ becomes lower at points A4 and A7. The highest difference is shown at location A7, where $\langle u'v' \rangle$ changes from -8 cm^2/s^2 in Test 2 to -1 cm^2/s^2 in this case. For Test 3, $\langle u'w' \rangle$ becomes lower at the river (point A6) than in Tests 2 and 4.

Test 5 presents some variations of the Reynolds stress $\langle u'v' \rangle$ and it reaches higher values at location A4, differing from the previous cases. This characteristic only appears in the reference case.

Table B.2. gives the Reynolds shear stress values $\langle u'v' \rangle$ and $\langle u'w' \rangle$ for each experiment of Series 2 and Series 3. Other statistic values are presented in Appendix B.

From this table, Test 6 presents the lowest values of the Reynolds shear stress along both lines. From this results, it can be deduced that this configuration gives lower production term along line G (Y=0.22m) in terms of shear stress values.

If the Reynolds stresses given by the previous table are considered, no important differences are shown between Tests 7 and 8 , however, Test 6 presents lower values near the downstream side of the entrance (A7) and this result can be attributed to the lower length of the groyne in Test 9.

			Test 7		Test 8		Test 6		Test 9	
			n=5 s=3cm		n=5 s=4.5cm		n=6 s=3cm		n=6 s=2cm	
Line		**X(m)**	**<u'v'>**	**<u'w'>**	**<u'v'>**	**<u'w'>**	**<u'v'>**	**<u'w'>**	**<u'v'>**	**<u'w'>**
	A1	***5.47***	-3.04	-0.57	-2.04	-0.80	-1.46	-0.55	-1.63	-0.47
G	***A4***	***5.98***	-2.42	-0.90	-2.32	-0.45	-1.57	0.09	-1.01	-0.46
Y=0.22m	***A7***	***6.47***	-2.25	-0.82	-1.60	-0.26	-0.88	0.21	-2.12	-0.59

			Test 7		Test 8		Test 6		Test 9	
			n=5 s=3cm		n=5 s=4.5cm		n=6 s=3cm		n=6 s=2cm	
Line		**Y(m)**	**<u'v'>**	**<u'w'>**	**<u'v'>**	**<u'w'>**	**<u'v'>**	**<u'w'>**	**<u'v'>**	**<u'w'>**
	A4	***0.22***	-2.42	-0.90	-2.32	-0.45	-1.57	0.09	-1.01	-0.46
B	***A5***	***0.62***	-0.37	0.86	-0.71	1.03	-0.81	1.17	-0.80	1.42
X=5.98m	***A6***	***1.02***	-0.22	0.62	-0.11	0.71	-0.18	0.46	-0.19	-0.02

Table B.2. Series 2 and 3. Reynolds shear stresses u'v' and u'w' from ADV data (cm^2/s^2).

Appendix C.

PTV depth-averaged transformation.

In order to establish the depth-averaged velocity for the PTV results the logarithmic law for the vertical distribution is used.

Nezu and Nakagawa (1993) discuss that the logarithmic law is inherently valid only in the wall region. However, in practical applications it is still commonly assumed that the logarithmic law describes the velocity distribution over the entire depth of uniform, steady open-channel flows.

The velocity distribution can be described by the logarithmic law:

$$u = \frac{u_*}{k} \ln\left(\frac{z}{z_0}\right) \tag{C.1}$$

where k denotes the Von Karman constant (equal to 0.41), z the depth, u is the streamwise velocity at level z and u_* is the friction velocity.

The friction velocity is given by $u_* = \sqrt{c_f} \cdot U$ (*Van Prooijen, 2004)*, where U is the time-averaged streamwise velocity over the depth and c_f is the bed friction coefficient.

The bed friction coefficient c_f for turbulent flows over a smooth bottom is determined by the relation (*Van Prooijen , 2004)*:

$$\frac{1}{\sqrt{c_f}} = \frac{1}{k}[\ln(\mathrm{Re}\sqrt{c_f}) + 1] \tag{C.2}$$

in which Re denotes the depth-based Reynolds number, given by $\mathrm{Re} = \frac{U \cdot h}{\upsilon}$, where U is the time-averaged streamwise velocity and υ is the kinematic viscosity, equal to 10^{-6} m^2/s. The parameter z_0 in equation (C.1) is given by $z_0 = \frac{k_s}{30}$, in which k_s is the Nikuradse coefficient.

From Manning's equation for mean velocity in uniform flows (taken from *Gonzalez et. al, 1996*; according to Chen, 1991), the Manning's roughness factor n ($s/m^{1/3}$) and k_s can be related as

$$n = \frac{K_n}{\sqrt{g}} \frac{35}{162} \cdot \left(\frac{k_s}{30}\right)^{1/6} \tag{C.3}$$

where K_n depends on the unit system and values of n used. It results in 1 for metric units if n is read from the values given in Chow's tables.

In that case, n and k_s are related as

$$n = 0.0391 \cdot k_s^{1/6} \tag{C.4}$$

For the present study, *n* is equal to 0.01 at the river stream (glass) and k_s results in 0.00028.

From PTV measurements of Test 2, if Y=0.59m is considered (last Y-coordinate with data within the PTV area) then u_{PTV} results 36.5 cm/s at the surface.

The purpose is to determine the averaged velocity value over the depth to obtain a ratio between the surface velocity (PTV) and the averaged velocity.

A first estimation of 30 cm/s for the averaged velocity is established to define the Reynolds number and the bed friction coefficient.

After several iterations to determine the correct logarithmic profile, it was found that the ratio between the average and the surface velocity, Φ, is equal to 0.91.

Data	**U_{PTV}(m/s)**	**h(m)**	**υ(cm^2/s)**	**n**	**k_s (m)**	**u_{PTV} (m/s)**
	0.332	0.14	0.01	0.01	0.00028	0.365

Last iteration	**U_{PTV}(m/s)**	**Re**	**c_f**
	0.332	46480	0.0022

↓

Results	**U_{PTV} (m/s)**	**Z_{mean} (m)**	**Φ=U_{PTV}/ u_{PTV}**
	0.33	0.058	***0.91***

Table C.1. Flow parameters from PTV data in Test 2.

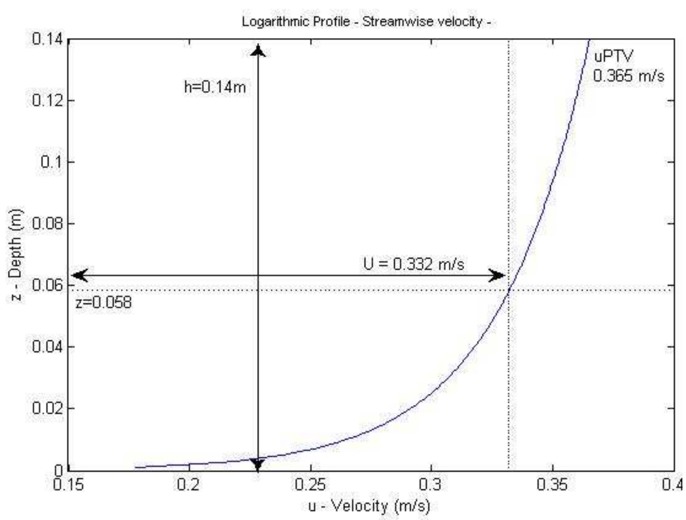

Figure C.1. Streamwise velocity profile from results of Test 2.

Consequently, the PTV results from Test 2 were transformed with this ratio to compare FinLab outcomes with the laboratory experiments.

Appendix D.

Numerical Model. Chezy coefficient to implement the groyne.

The flow resistance due to a groyne can be estimated from the effect of the blocking of the flow by its piles. The Chezy roughness coefficient will be modified at the location of the pile groyne according to the effect of that blocking.

The Chezy coefficient is related with the bed friction coefficient by means of the following expression:

$$C = \sqrt{\frac{g}{c_f}} \tag{D.1}$$

If the bed friction coefficient can be related with the energy loss coefficient for a row of piles, c_{loss-u}, by the following expression:

$$c_f = c_{loss-u} \cdot \frac{h}{\Delta x} \tag{D.2}$$

with h the water depth and Δx the size of the cell.

For a row of piles perpendicular to the U-direction the energy loss coefficient perpendicular to the flow is given by:

$$c_{loss-u} = \frac{N \cdot C_D \cdot d_{pile}}{2\Delta y}\left(\frac{A_{tot}}{A_{eff}}\right)^2 \tag{D.3}$$

in which

A_{tot} is the total cross section area ($A_{tot} = \Delta y$)
A_{eff} is the effective wet cross sectional area (A_{tot} minus the area blocked by piles).
C_D is the drag coefficient of a pile
d_{pile} is the diameter of a pile (in the case of a cylindrical shape)
N is the number of piles.

The drag coefficient, C_D, is a function of the shape of an object, orientation to flow, grouping and boundary conditions.

Drag coefficients are used to estimate the force due to the water moving around the piers, the separation of the flow and the resulting wake that develops downstream. D rag coefficients for bridge piers have been derived from experimental data (Lindsey, 1938) for various cylindrical shapes.

The following table, taken from *HEC_RAS Reference Manual (2008),* shows some typical drag coefficients that can be used for piers:

Pier shape	***Drag coefficient C_D***
Circular pier	1
Elongated piers with semicircular ends	1.33
Square nose piers	2

Table D.1. Typical drag coefficients for various pier shapes

For the case being, a value of the drag coefficient C_D equal to 2.00 is established.
From the flow conditions of the experiments, with a total depth h equal to 0.14m, the previous parameters are:

$$A_{tot} = h \cdot w + \frac{h^2}{2} \tag{D.4}$$

$$A_{blocked} = l \cdot N \cdot h - A_b \tag{D.5}$$

Parameter	***Value***
A_{tot}	0.1358 m^2
A_b	0.0081 m^2
$A_{blocked}$	0.0213 m^2
A_{eff}	0.1145 m^2
C_D	2.00
d_{pile} (l)	0.03 m
N	6 piles
$C_{loss\text{-}u}$	**1.9**

Table D.2. Typical drag coefficients for various pier shapes.

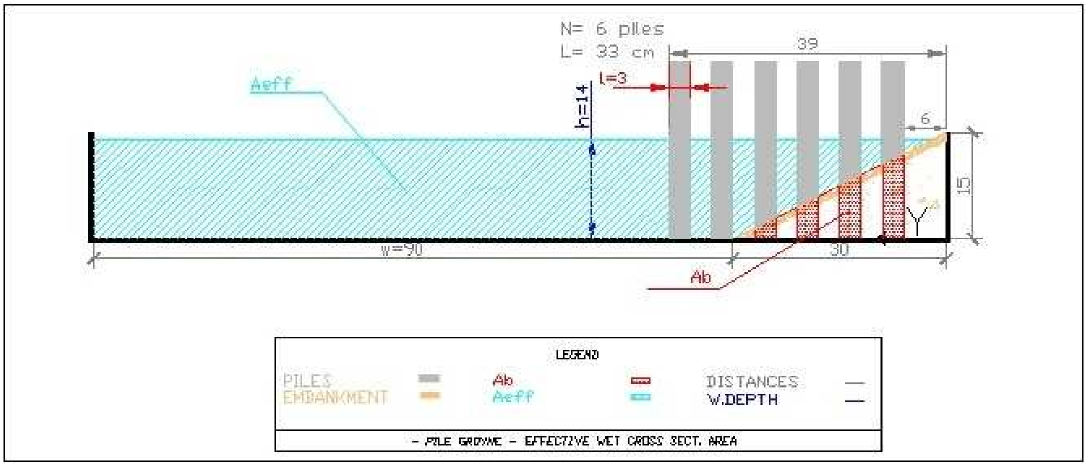

Figure D.1. Sketch wet cross sectional area and groyne distribution.

Consequently, with an average mesh size of approximately 2 cm, the Chezy coefficient results in:

$$C = \sqrt{\frac{g\Delta x}{c_{u-loss}h}} = \sqrt{\frac{9.81 \cdot 0.02}{1.9 \cdot 0.14}} = 0.86\,\mathrm{m}^{½}/\mathrm{s} \tag{D.6}$$

Finally, a value of 1 m^{½}/s will be considered for the model case with groyne.

The bottom friction coefficient will be modified in a number of selected cells at the same location than the piles. The case with the groyne 35 cm upstream the entrance will be modelled, in which the piles are located from points (4.65, 0.06) to (4.65, 0.39).

Appendix E.

Numerical Model. Figures.

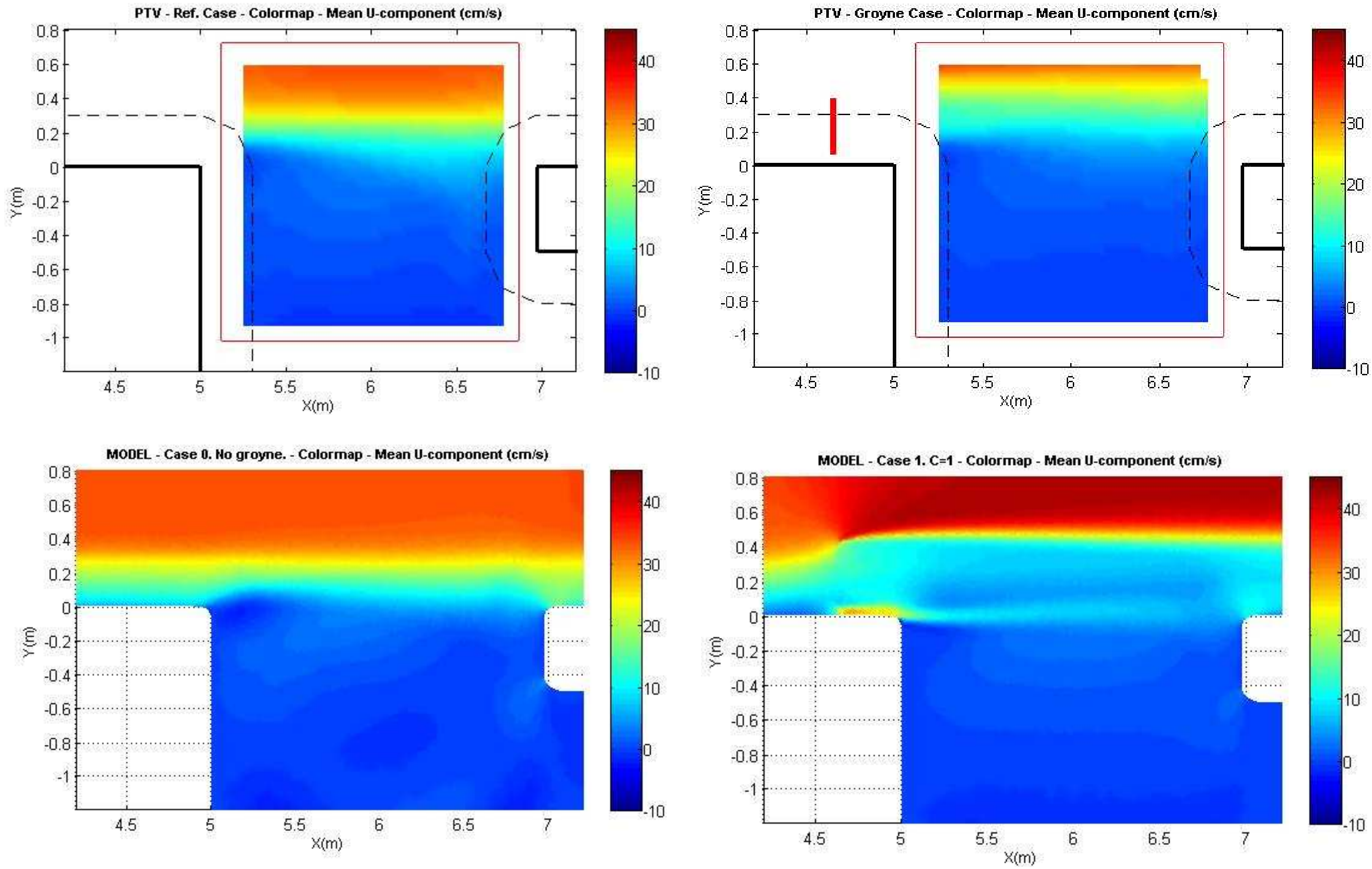

Figure E.1. Colormaps. Mean U-component (cm/s). PTV results Tests 2 and 6, MODEL Cases "0" and "1" (C=1).

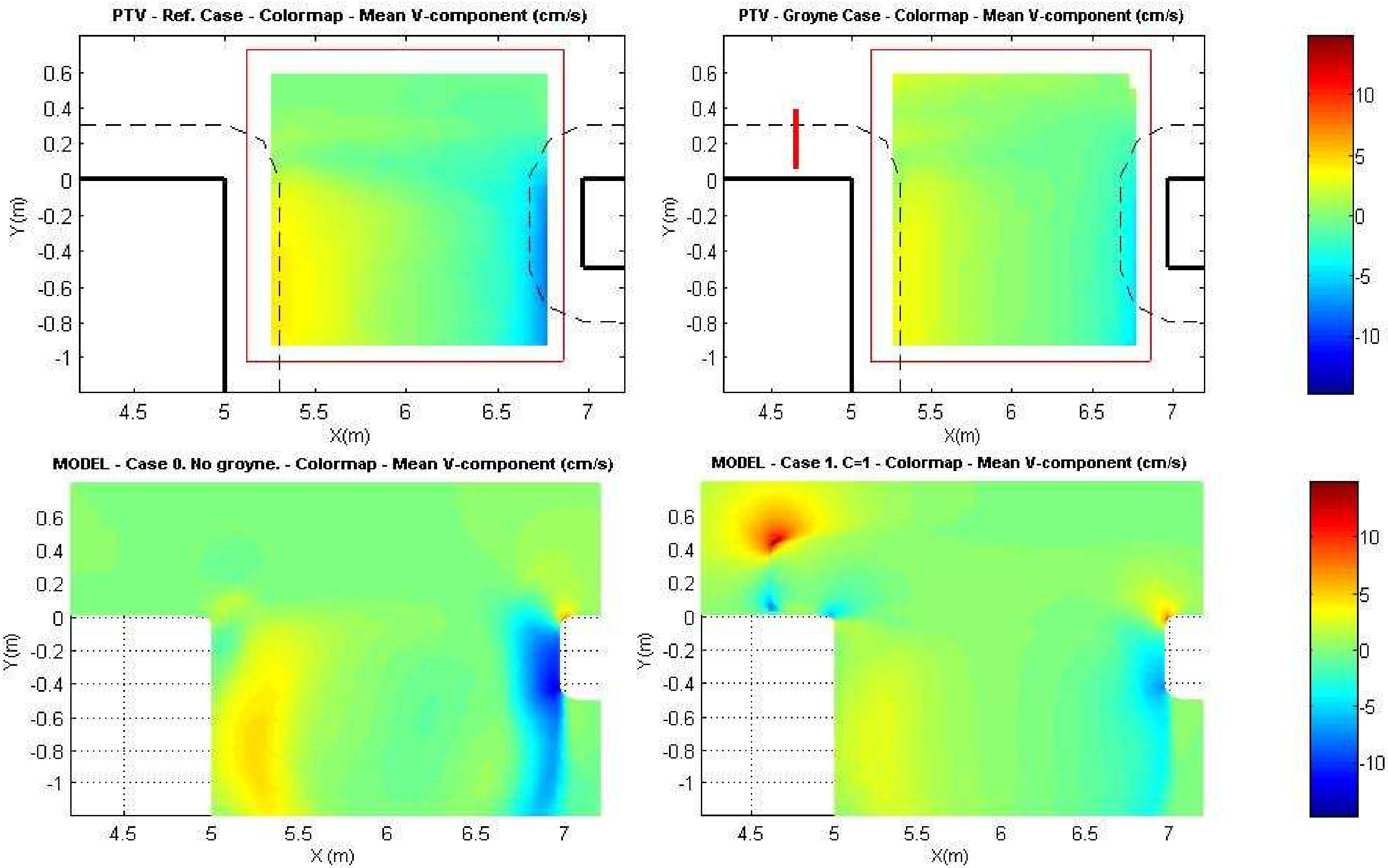

Figure E.2. Colormaps. Mean V-component (cm/s). PTV results Tests 2 and 6, MODEL Cases "0" and "1" (C=1).

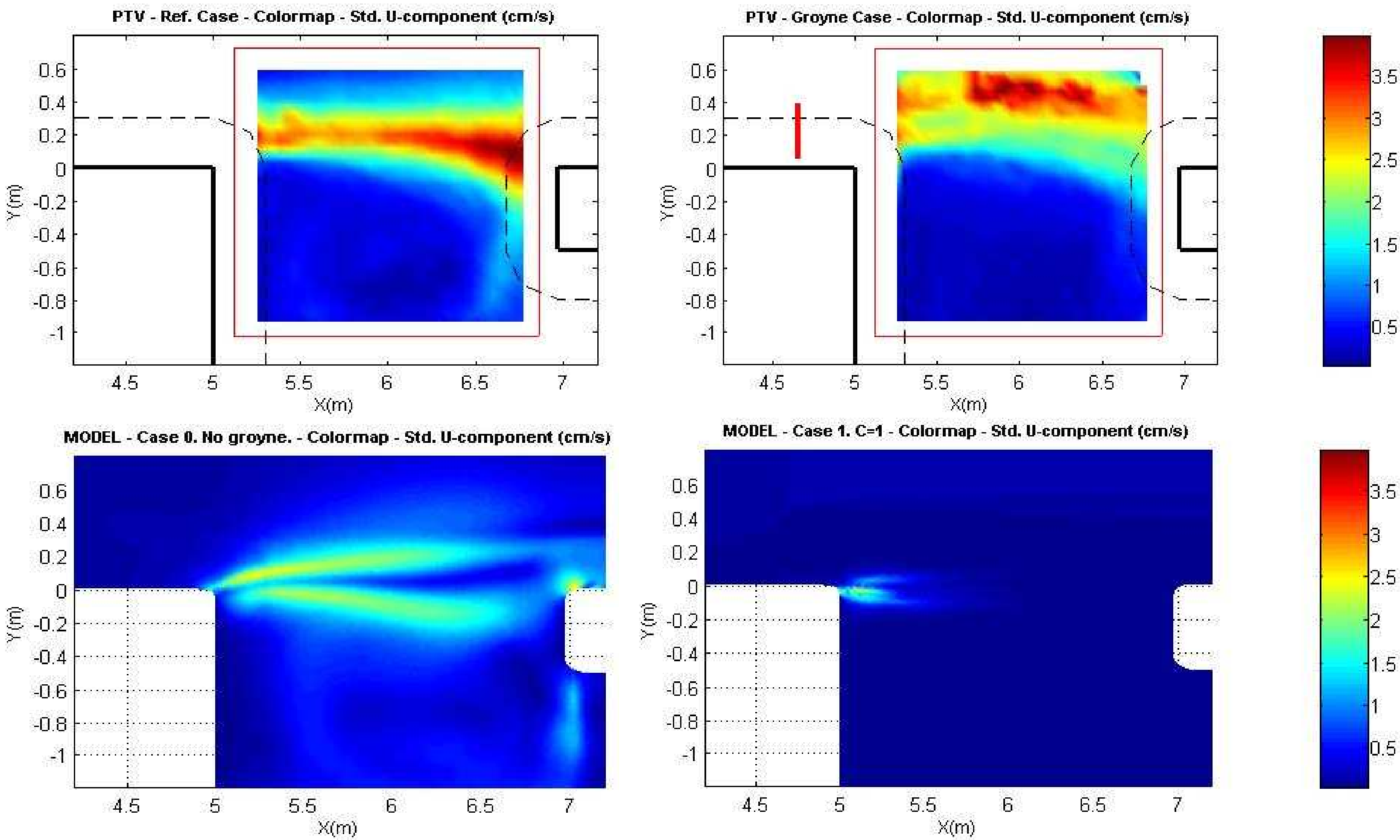

Figure E.3. Colormaps. Std U-component (cm/s). PTV results Tests 2 and 6, MODEL Cases "0" and "1" (C=1).

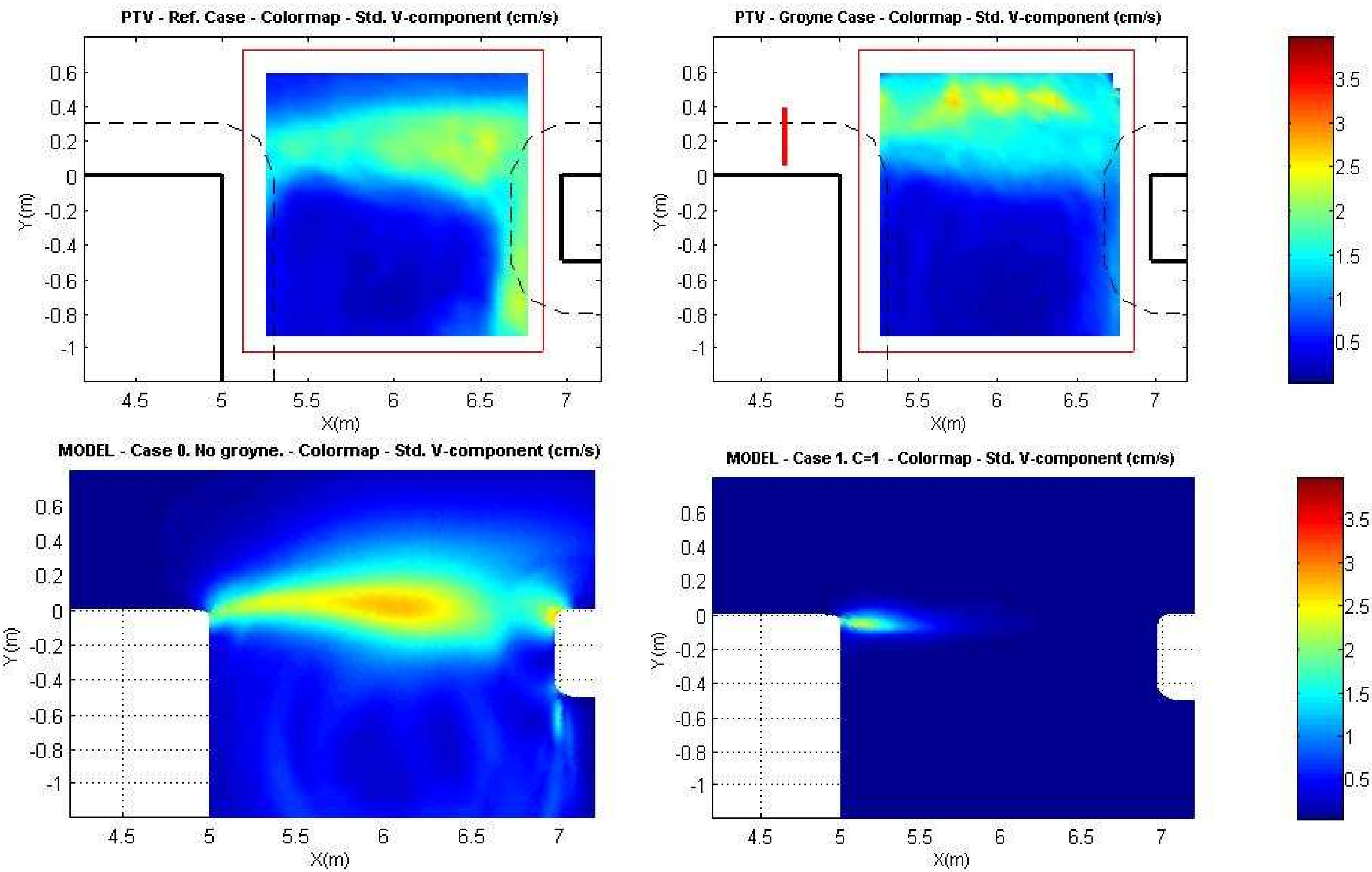

Figure E.4. Colormaps. Std V-component (cm/s). PTV results Tests 2 and 6, MODEL Cases "0" and "1" (C=1).

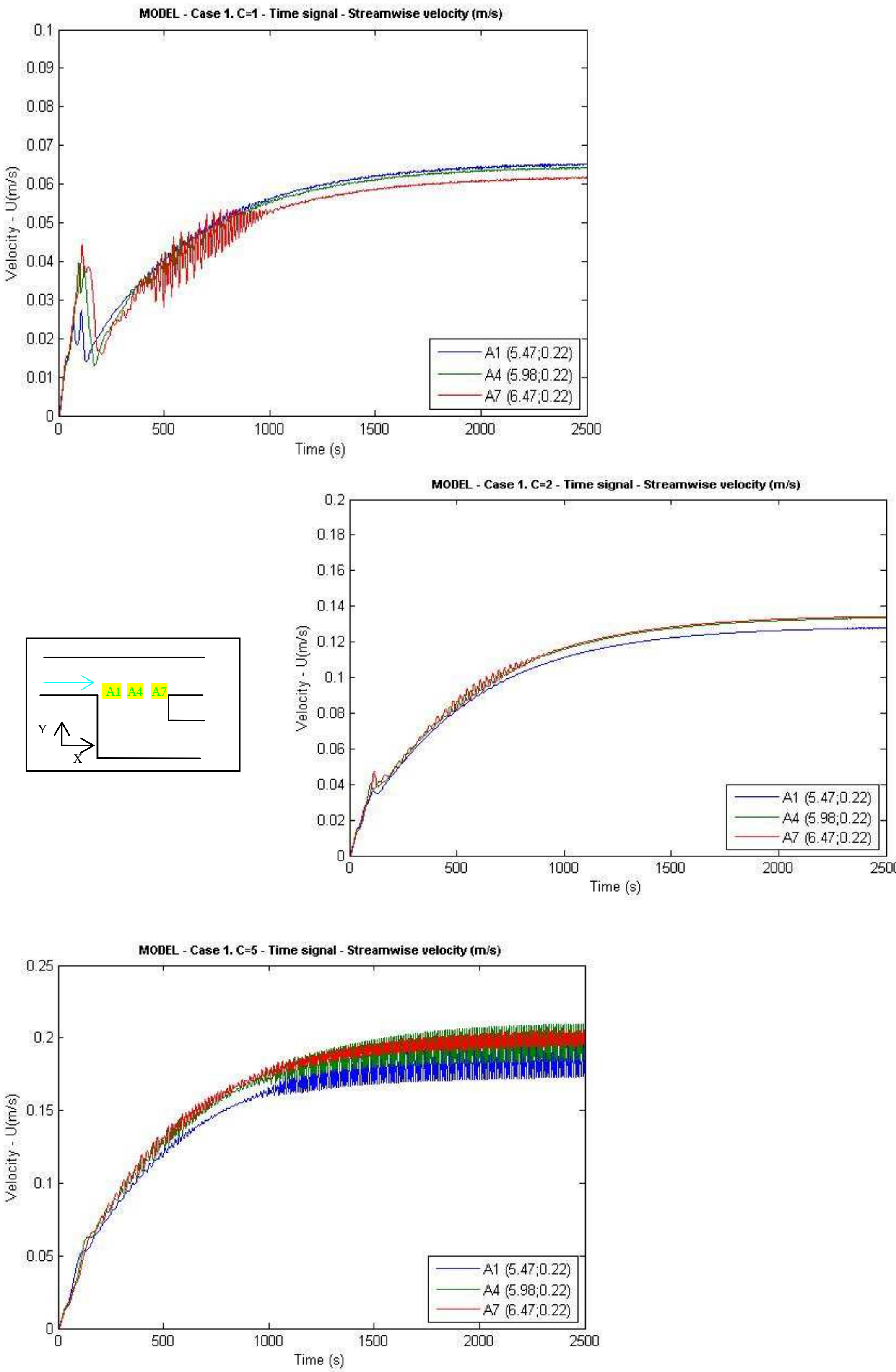

Figure E.5. Time signals of U-component (cm/s). MODEL case “1”C=1 (top), C=2(middle) and C=5(bottom).

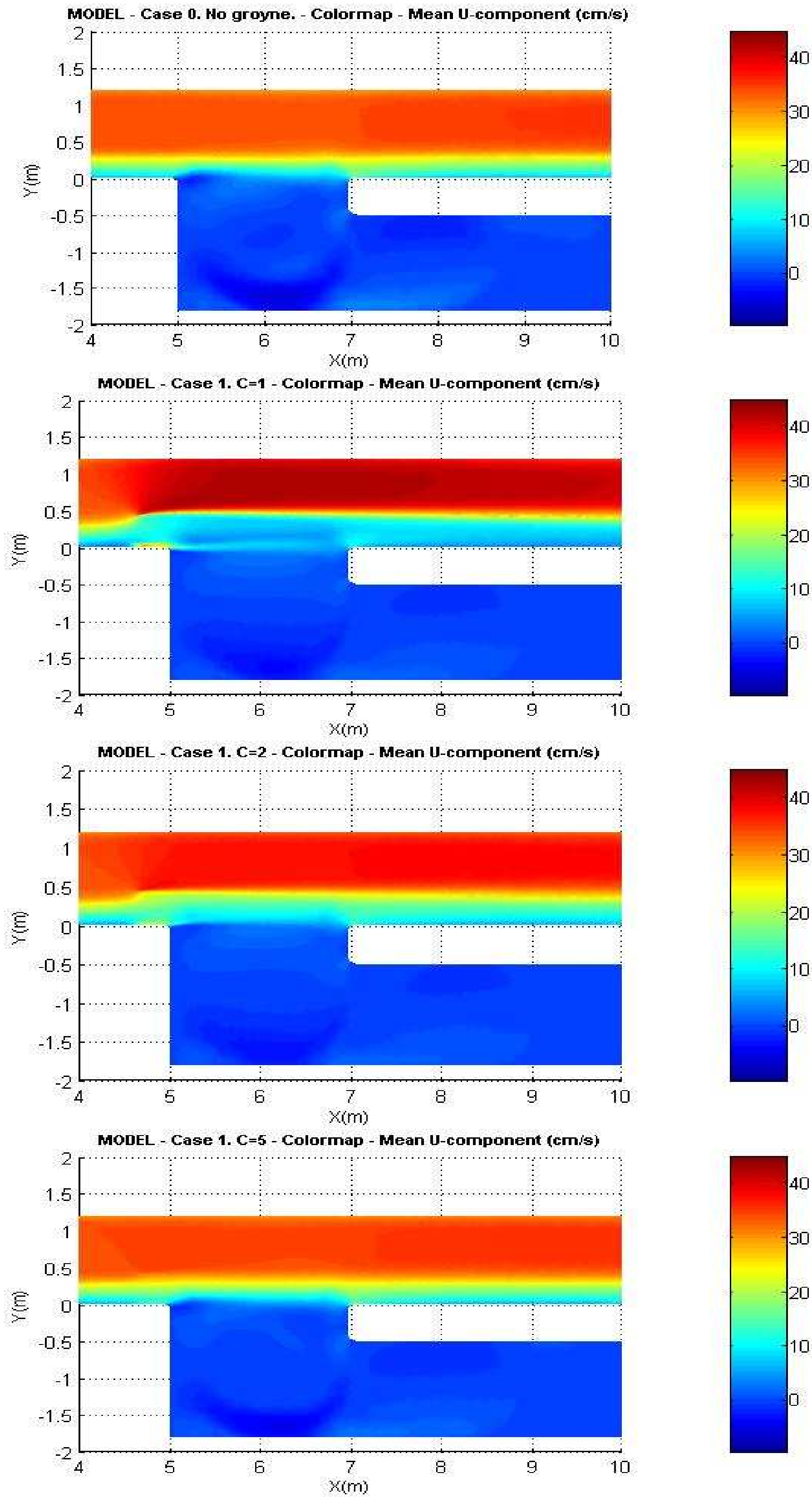

Figure E.6. Colormaps. Mean U-component (cm/s). MODEL Case "0" and Cases "C=1", "C=2" and "C=5".